NASA-TM-109739

IN-05-TM
5049
132P

Vehicle Integration Effects on Hypersonic Waveriders.

Charles Edward Cockrell, Jr.
Hypersonic Airbreathing Propulsion Branch, Gas Dynamics Division,
NASA Langley Research Center

B.S., May 1990, University of Virginia, Charlottesville, Virginia.

A Thesis submitted to

The Faculty Of

The School of Engineering and Applied Science
of The George Washington University in partial satisfaction
of the requirements for the degree of Master of Science

April 21, 1994

This research was conducted at NASA LaRC.

ABSTRACT

The integration of a class of hypersonic high-lift configurations known as waveriders into hypersonic cruise vehicles was evaluated. Waveriders offer advantages in aerodynamic performance and propulsion/airframe integration (PAI) characteristics over conventional hypersonic shapes. A wind-tunnel model was developed which integrates realistic vehicle components with two waverider shapes, referred to as the "straight-wing" and "cranked-wing" shapes. Both shapes were conical-flow-derived waveriders at a design Mach number of 4.0. The cranked-wing shape was designed to provide advantages in subsonic performance and directional stability over conventional waveriders. Experimental data and limited computational fluid dynamics (CFD) predictions were obtained over a Mach number range of 2.3 to 4.63 at a Reynolds number of 2.0×10^6 per foot. The CFD predictions and flow visualization data confirmed the shock attachment characteristics of the baseline waverider shapes and illustrated the waverider flow-field properties. Both CFD predictions and experimental data showed that no significant performance degradations occur at off-design Mach numbers for the waverider shapes and the integrated configurations. The experimental data showed that the effects of adding a realistic canopy were minimal. The effects of adding engine components were to increase the drag and thus degrade the aerodynamic performance of the configuration. A significant degradation in aerodynamic performance was observed when 0^o control surfaces were added to close the blunt base of the waverider to a sharp trailing edge. A comparison of the fully-integrated waverider models to the baseline shapes showed that the performance was significantly degraded when all of the components were added to the waveriders. The fully-integrated configurations studied here do not offer significant performance advantages over conventional hypersonic vehicles, but still offer advantages in air-breathing propulsion integration. Additionally, areas are identified in this study where improvements could be made to enhance the performance. Both fully-integrated configurations are longitudinally unstable over the Mach number range studied for unpowered conditions. The cranked-wing fully-integrated configuration provided significantly better lateral-directional stability characteristics than the straight-wing configuration.

ACKNOWLEDGEMENTS

Numerous individuals deserve special thanks for their contributions to this effort throughout all stages of the project including preliminary concept development, model design and fabrication, wind tunnel testing and development of the computational models. Larry Huebner, Group Leader for the Hypersonic PAI Group in the Hypersonic Air-Breathing Propulsion Branch, served as co-Project Engineer for the wind tunnel tests and provided invaluable assistance during all phases of this project. This project was conducted as a cooperative effort with Lockheed-Fort Worth Company in Fort Worth, Texas. Dennis Finley was the primary Lockheed Engineer on the project and also provided input in all areas.

The preliminary lines for the model were developed by the Hypersonic Vehicles Office at NASA Langley Research Center. Dr. Mark Lewis and Dr. John Anderson of the University of Maryland provided assistance in obtaining and running the MAXWARP design code. The model designs were developed by General Dynamics-Convair Division in San Diego, California. Bill Conkling, Tom Barclay and Elmo Sterling fabricated the model at NASA Langley's model fabrication shop. The numerical surface description of the baseline waverider models used for CFD grid generation were developed at NASA Langley's Geometry Laboratory. Susan Bowen of Computer Sciences Corporation provided assistance in enhancing the schlieren and vapor screen images from the wind tunnel tests. Dana Forrest served as the primary Data Analyst for the wind tunnel tests. Bill Corlett, Facility Manager of the Unitary Plan Wind Tunnel, provided assistance in developing test plans and familiarization with tunnel procedures. The Technicians and Test Engineers at UPWT also deserved special thanks for their efforts in the experimental phase of this project.

Finally, many thanks to my wife Holly, whose great moral support provided the motivation to complete this project.

TABLE OF CONTENTS

LIST OF SYMBOLS

B.L.	Butt-line of model (distance from center line in spanwise direction) (in)
C_D	Drag coefficient
C_f	Skin friction coefficient
C_l	Rolling moment
$C_{l\beta}$	Rolling moment derivative, $\frac{\partial C_l}{\partial \beta}$
C_L	Lift coefficient
C_m	Pitching moment coefficient
$C_{m\alpha}$	Pitching moment curve slope, $\frac{\partial C_m}{\partial \alpha}$
C_n	Yawing moment
$C_{n\beta}$	Yawing moment derivative, $\frac{\partial C_n}{\partial \beta}$
C_p	Specific heat at constant pressure $\left(\frac{\text{Btu}}{\text{lbm} - {}^{o}\text{R}}\right)$
C_v	Specific heat at constant volume $\left(\frac{\text{Btu}}{\text{lbm} - {}^{o}\text{R}}\right)$
D	Drag (lbf)
E_t	Total energy (Btu/lbm)
k	Thermal conductivity coefficient
l	Distance downstream of the leading edge (ft.)
L	Lift (lbf)
L_{cone}	Length of generating flow field cone
M.S.	Model station (distance from nose in streamwise direction) (in)
M_e	Local Mach number
M_∞	Freestream Mach number
p	Pressure (lbf/ft^2)
q	Dynamic pressure (lbf/ft^2)
Re'_x	Reynolds number at the reference temperature (reference temperature method)
S_{ref}	Planform area (ft^2)

S_{wet}	Wetted surface area (ft^2)
T_w	Wall temperature (^oR)
T'	Reference temperature (reference temperature method) (^oR)
T_∞	Freestream temperature (^oR)
u,v,w	Velocity components (ft/sec)
u_c	Total velocity at first cell center next to solid boundaries (ft/sec)
V	Total volume (ft^3)
V_{eff}	Volumetric efficiency, $V^{2/3}/S_{ref}$
V_r	Velocity component along a conical ray (ft/sec)
V_∞	Freestream velocity (ft/sec)
W.L.	Water-line of model (distance from zero reference in vertical direction) (in)
X, Y, Z	Cartesian coordinates (ft)
y^+	Grid spacing parameter
α	Angle of attack
β	Sideslip angle
γ	Ratio of specific heats, C_p/C_v
δ	Cone semi-apex angle
$\Delta\zeta$	Distance from solid boundary to first cell center (ft)
Θ	Angle of ray reference to cone axis
Θ_f	Angle of flow in test section
μ	Viscosity coefficient $(\frac{lbf-sec}{ft^2})$
μ'	Viscosity coefficient at the reference temperature (reference temperature method)
μ_c	Viscosity coefficient at the first cell center next to solid boundaries
ξ, η, ζ	Computational coordinates
ρ	Density (lbm/ft^3)
ρ'	Reference density (reference temperature method) (lbm/ft^3)
ρ_c	Density at the first cell center next to solid boundaries (lbm/ft^3)

LIST OF TABLES

LIST OF FIGURES

CHAPTER 1
INTRODUCTION

The objectives of this study are to evaluate, using both experimental and computational methods, the aerodynamic performance and stability characteristics of a class of hypersonic high-lift configurations known as waveriders. Additionally, the study will determine the effect on aerodynamic performance and stability of integrating realistic vehicle components with pure waverider forebodies. To accomplish these objectives, a wind-tunnel model which integrates two pure waverider shapes with various canopies, wings, engine components and control surfaces was fabricated and tested. Limited computational predictions were also obtained in order to provide comparisons with experimental data and design-code predictions. The results will create an aerodynamic data base for waverider-derived configurations, will show the effects of individual realistic vehicle components on waverider performance and will quantify the differences in aerodynamic performance and stability between the baseline waverider shapes and the fully-integrated waverider configurations.

A waverider is any shape that is designed such that the bow shock is perfectly attached along the outer leading edge at the design condition. The waverider design method leads to several advantages over conventional hypersonic concepts. The attached leading edge shock wave confines the high pressure region to the lower surface and leads to high lift-to-drag ratios. Design predictions suggest that waveriders have an aerodynamic performance advantage, in terms of higher lift-to-drag ratios, over existing hypersonic vehicles. The flow field below the waverider bottom surface is uniform and, in the case of waveriders derived from axisymmetric flow fields, there is no crossflow in this region, making these shapes attractive candidates for engine integration. These advantages have led to interest in using waverider shapes as the forebodies of hypersonic air-breathing engine-integrated airframes. Waveriders have been considered for various types of missions including hypersonic cruise, single-stage-to-orbit and various space-based applications.

Waveriders were first introduced in the 1950's by Nonweiler in the form of "caretshaped" waveriders, designed from supersonic flows over simple wedges.[1] Early waverider shapes were not considered for any practical application due to many criticisms associated with these shapes. These criticisms included poor off-design performance, poor volumetric efficiencies and design methods which relied on inviscid techniques. Recent research in this area has addressed many of these issues. Experimental and computational research has shown that waveriders can be designed which provide not only excellent aerodynamic performance at the design point, but also reasonable performance at off-design Mach numbers.[2,3,4,5] New design methods are able to produce shapes which have good aerodynamic performance as well as high volumetric efficiencies. Finally, the most recent design codes are capable of including an estimate for skin friction in the optimization process, resulting in more realistic shapes and performance predictions.[2] These advances have led to a renewed interest in waverider-derived configurations.

The current study examines the aerodynamic performance and stability of a waverider-derived hypersonic cruise vehicle. No data currently exist which address the integration of realistic vehicle components with waverider configurations. Therefore, the objectives of this study are threefold. The first is to create an experimental and computational data base for waverider-derived configurations. The second is to examine the effects of individual vehicle components on pure waverider performance. The final objective is to determine the differences in aerodynamic performance and stability which result from integrating all vehicle components and to assess whether the fully-integrated waverider-derived configuration provides the same advantages that the pure waverider does. The objectives of the study will be accomplished using results from wind-tunnel testing and limited computational fluid dynamics (CFD) solutions for the flow fields of some of the baseline waverider shapes. A wind tunnel model was designed which integrates canopies, engine packages and control surfaces with two Mach 4.0 waverider configurations. The model was tested in the Unitary Plan Wind Tunnel (UPWT) at NASA Langley Research Center. Limited CFD predictions were obtained for the baseline waverider configurations in order to provide comparisons with experimental data and design-code predictions.

This thesis contains a description of waverider design theory and a discussion of the method used in the development of the baseline waverider configurations and the integrated vehicle components. The details of the experimental study are presented, including a description of the facility, test conditions, instrumentation and data obtained. The computational method used to obtain the CFD predictions is also presented, including the method of generating computational grids and the flow solver used in the study. The results are presented in two chapters. Chapter 5 shows the results of the baseline waverider configurations without integrated components. This chapter shows comparisons between computational and experimental data at selected angles of attack at the design Mach number as well as at off-design Mach numbers. Aerodynamic performance characteristics are examined together with longitudinal, directional and lateral stability data. Flow-field characteristics are also examined using schlieren and vapor-screen photographs from wind-tunnel tests as well as CFD flow-field solutions. Chapter 6 shows the experimental results of integrating aircraft components on the baseline waverider shapes. The effects of the canopy, engine components and control surfaces on aerodynamic performance and stability are examined. The characteristics of the fully-integrated waverider-derived configurations are also examined and compared to those of the baseline waverider configurations. Finally, Chapter 7 presents interpretations and conclusions from the data presented.

CHAPTER 2
WAVERIDER DESIGN METHODS AND CONFIGURATION DEVELOPMENT

2.0 Summary

A specific waverider shape is designed by selecting freestream conditions, the type and dimensions of the generating flow-field body and the shape of the leading edge, which is defined on the shock wave produced by the generating body. The resulting waverider shape provides advantages over conventional hypersonic shapes in terms of aerodynamic performance and propulsion/airframe integration (PAI) characteristics. A waverider design code was used which employs an optimization routine to design various types of waveriders and includes viscous effects and user-specified volumetric constraints in the optimization process. This code was used to design two waverider shapes for the current study using design conditions and volumetric constraints that were selected based on a hypersonic-cruise vehicle application. A wind-tunnel model was designed which integrated the two waverider forebodies with canopies, engine components and control surfaces.

2.1 Waverider Design Methods

A specific waverider shape is uniquely defined by freestream conditions, the type of generating flow-field body and a leading edge definition.[2] The shapes of the upper and lower surfaces of the configuration follow from these parameters. The freestream conditions, including Mach number and Reynolds number or altitude, are selected based on mission criteria. The generating flow-field body is used to define the shock shape upon which the leading edge of the waverider is defined. Any arbitrary body in supersonic or hypersonic flow can be used as a generating flow-field body. This study focuses specifically on conical-flow-derived waveriders. The generating flow-field body used for the configurations in this study is a right circular cone in supersonic or hypersonic flow. The length of the generating cone, length of the waverider and semi-apex angle of the cone are generally specified by the designer. The selection of these parameters can have a significant effect on the shape of the waverider generated as well as on the aerodynamic performance of the configuration. The planform shape, or leading edge, is defined on the shock wave produced by the cone. The inviscid conical flow field behind the shock wave is obtained from the Taylor-Maccoll equation, which is given as[6]

$$\frac{\gamma-1}{2}\left[1-V_r^2-\left(\frac{dV_r}{d\Theta}\right)^2\right]\left[2V_r+\left(\frac{dV_r}{d\Theta}\right)\cot\Theta+\frac{d^2V_r}{d\Theta}\right]-\frac{dV_r}{d\Theta}\left[V_r\frac{dV_r}{d\Theta}+\frac{dV_r}{d\Theta}\frac{d^2V_r}{d\Theta}\right]=0 \quad (2.1)$$

where,

V_r = component of velocity along a conical ray,
Θ = angle of the ray referenced to the axis of the cone,
γ = ratio of specific heats.

Figure 2.1 illustrates the design of a conical-flow derived waverider. The lower surface of the configuration is defined by tracing streamlines from the leading edge to the base of the configuration. The result is that the lower compression surface is a stream surface behind the conical shock wave. The upper surface may be designed using a number of different methods. Among the most common methods are to design the surface as a freestream surface or as a slight expansion surface. The conical flow field, defined behind the shock wave, exists only on the lower surface flow field of the waverider.

The resulting configuration provides two distinct advantages over existing hypersonic configurations. The first is an aerodynamic performance advantage over conventional vehicles.[2,6] Theoretically, the shock wave is perfectly attached along the outer leading edge at the design Mach number. The result is that the high pressure region behind the shock wave is confined to the lower surface and no flow spillage from the lower surface to the upper surface occurs. The maximum lift-to-drag ratios which are produced by this method are higher than those of existing hypersonic configurations. Figure 2.2, taken from reference 7, shows the traditional "L/D barrier" in the supersonic/hypersonic regime for conventional vehicles. This is an empirical correlation based on actual flight vehicle experience and extrapolated to hypersonic Mach numbers.[8] The symbols in the figure represent predictions for conical-flow-derived waveriders generated using the current method, which is described in detail in reference 7. In general, the conical-flow-derived waveriders show an increase in maximum lift-to-drag ratio from the traditional L/D barrier.

Another advantage of axisymmetric waverider flow fields is that they provide excellent propulsion/airframe integration (PAI) characteristics.[9] The lower surface flow field is highly uniform, and there is no crossflow in this region. These characteristics are ideal for the integration of scramjet engine modules. The aerodynamic performance and PAI benefits offered by waveriders have generated interest in their use for various hypersonic vehicle designs.

Waveriders are typically optimized for some parameter such as maximum lift-to-drag ratio or minimum drag at the freestream conditions specified. The choice of optimization parameter is based on the type of vehicle desired or on various mission criteria. For example, maximum lift-to-drag ratio would be more appropriate as a design parameter for hypersonic cruise vehicles, while a minimum drag shape would be appropriate for single-stage-to-orbit missions. This study will focus on waveriders optimized for maximum lift-to-drag ratio at prescribed freestream conditions.

2.2 MAXWARP Design Code

The design code utilized in this study is the (University of) Maryland Axisymmetric Waverider Program (MAXWARP).[2,7,10] The MAXWARP code is an inviscid design method which includes an estimate for skin friction in the design process. The code uses a simplex optimization routine to optimize waveriders for a given figure of merit: maximum lift-to-drag ratio or minimum drag. Various volumetric constraints may also be imposed by the user in order to produce waveriders with desirable structural characteristics and component packaging. These constraints include values for aspect ratio, slenderness ratio and total volume.

The procedure in MAXWARP is to create new waverider shapes over a number of iterations until the optimum shape is found. For the case of conical-flow-derived waveriders, the Taylor-Macoll equation is integrated using a fourth order Runge-Kutta method to compute the inviscid conical flow field behind the shock wave. The cone semi-apex angle and length of the flow-field generating body are specified by the user along with freestream conditions. The code starts with an initial leading edge definition on the conical shock wave and then creates a waverider shape from this initial leading edge. The basis leading edges are defined by pre-set functions in the code and are not specified by the designer. The pressure distributions on the surface of the configuration are integrated to calculate lift and drag coefficients. Additionally, an estimate for skin friction is included so that force coefficient predictions include both inviscid and viscous effects. The optimization routine generates an updated leading edge that drives towards the desired figure of merit.[2] At each step, a new leading edge definition is used to generate a new waverider shape and calculate the force coefficients. The code eliminates any shape which violates any of the user-specified volumetric constraints.

The inclusion of a skin friction estimate within the optimization process is one of the unique aspects of the MAXWARP code. As a result, the optimization routine attempts to minimize wetted surface area and thereby reduce skin friction drag. The skin friction coefficient, C_f, is calculated using the reference temperature method which is given as[11]

$$C_f = \frac{0.0592}{(Re'_x)^{0.2}} \tag{2.2}$$

where the reference Reynolds number, Re'_x, is given by

$$Re'_x = \frac{\rho' V_\infty l}{\mu'} \tag{2.3}$$

and

ρ' = reference density,

V_∞ = Freestream Velocity,

μ' = reference viscosity,

l = distance downstream of the leading edge.

The reference density and viscosity are evaluated at the reference temperature, T', which is given by

$$\frac{T'}{T_\infty} = 1 + 0.032M_e^2 + 0.58\left(\frac{T_w}{T_\infty} - 1\right) \tag{2.4}$$

where

T_∞ = Freestream temperature (K),

M_e = Local Mach number,

T_w = Wall temperature (K).

Equations (2.2) and (2.4) apply to a turbulent boundary layer. MAXWARP allows the designer to specify a fully-turbulent or fully-laminar boundary layer. The wall temperature is specified by the designer as part of the initial set of input parameters. The inclusion of skin friction in the optimization routine of MAXWARP addresses a major criticism of waveriders. Previously, only inviscid methods were used which resulted in shapes with large surface areas and therefore, large values of skin friction. The true lift-to-drag ratios of these configurations were typically poor compared to predicted values. The effect of including skin friction in the optimization routine is to generate shapes that have relatively smaller wetted surface areas than those designed by purely invisicid methods. The class of waveriders generated using this method are referred to as "viscous-optimized" waveriders. However, the term "viscous-optimized" in this context only refers to the inclusion of a skin friction estimate in force coefficient values within the optimization routine. The code does not account for the change in effective surface shape which results from the presence of a boundary layer.

The code also contains an option which allows the designer to specify a set of leading edge coordinates to design a specific waverider shape, without running the optimization routine. Using this option, the code simply designs the upper and lower surfaces from the given leading edge coordinates and computes force coefficient estimates for the design.

2.3 Design Conditions for the Current Study

The baseline waverider configurations used in this study were designed using the MAXWARP design code. The parameters for freestream conditions and optimization parameters were chosen based on the applicability of this study to a hypersonic cruise vehicle, with facility limitations taken into account. The design freestream Mach number was 4.0 and the design Reynolds number was $2.0\text{x}10^6$ per foot. Although the specific Mach number range of interest for this type of vehicle would be approximately 5.0 to 5.5, Mach 4.0 was selected as the design point based on the limitations of the Unitary Plan Wind Tunnel (UPWT) and the range of data desired. The Mach number range in the high Mach number test section of this facility is 2.3 to 4.63. A design point of Mach 4.0 allows data to be obtained at, above and below the design point. This will allow for the validation of the waverider concept at the design Mach number and will also allow for the evaluation of off-design performance. Data obtained in this range of Mach numbers would be applicable to a Mach 5.0-5.5 vehicle with only a re-design of the waverider forebody necessary in order to achieve shock attachment at the design point of interest. The Reynolds number chosen is based on nominal operating conditions in the UPWT. The configuration was optimized for maximum lift-to-drag ratio at the design point since this is more appropriate as a hypersonic cruise performance parameter than minimum drag.

A fully turbulent boundary layer was specified in the design with a wall temperature of 585 ^{o}R. It is not likely that fully laminar conditions could be maintained in experimental testing at the conditions of interest and transition is difficult to predict. Fully turbulent conditions can be maintained by the application of boundary layer transition grit to the model surface. The wall temperature was selected based on previous experimental data from models tested in the UPWT.

A right circular cone was used as the generating flow-field body for the waverider shape. A study was conducted, using the MAXWARP code, to determine the semi-apex angle of the cone that would provide the highest maximum lift-to-drag ratio at the conditions specified. This was done by generating waveriders using various cone angles and selecting the value that yielded the best aerodynamic performance. Based on this study, a cone semi-apex angle of 8.1 degrees was selected. Figure 2.3 shows the variation of lift-to-drag ratio with cone semi-apex angle for the cases generated.

The optimum waverider shape generated at the conditions specified, with no volumetric constraints imposed, provides excellent aerodynamic performance but poor volumetric efficiency and structural characteristics. Therefore, some volumetric constraints were incorporated into the optimization routine in order to meet certain design guidelines. These guidelines were based on desired characteristics of a waverider-derived hypersonic cruise vehicle and include target values for aspect ratio, volumetric efficiency, PAI characteristics and structural characteristics.[12] The target value of span-to-length ratio was 0.8. Larger span waveriders yield better aerodynamic performance, but are difficult to integrate as a full waverider-based vehicle. An attempt was made to increase the volumetric efficiency from the unconstrained value while accepting a minimum penalty in lift-to-drag ratio. The volumetric efficiency is defined as

$$V_{eff} = V^{2/3}/S_{wet} \tag{2.5}$$

where,

V_{eff} = volumetric efficiency,

V = Total Volume

S_{wet} = Wetted Surface area.

Additionally, a configuration with a flat or slightly convex bottom surface was desired for ease in propulsion systems integration. A configuration free of substantial curvature over most the cross section was also desired for structural support within the model and for the inclusion of an internal spar in an actual aircraft. These guidelines were achieved by adjusting the user-specified volumetric constraints described previously as well as the length of the flow-field generating cone.

2.4 Waverider Description

Two different waverider shapes were developed for this study. The first shape is referred to as the "straight-wing" shape and was designed using the MAXWARP optimization routine using the guidelines previously outlined in section 2.3. The second shape, referred to as the "cranked-wing" shape, was designed by adjusting the leading edge of the straight configuration to create a curved wing-tip shape that has increased aspect ratio, but still maintains shock attachment along the outer leading edge at the design freestream condition. The term "cranked" in this context refers to a shape in which the sweep angle not only changes, but also has a large dihedral angle in the plane of the base. The cranked-wing shape is designed to provide improvements in subsonic performance and directional stability, while maintaining the waverider aerodynamic performance advantage in the supersonic/hypersonic regime.

A 3-view drawing and an oblique view of the straight-wing waverider shape is shown in figure 2.4. The selected shape meets most of the design guidelines specified previously.

The span-to-length ratio is 0.824. This is greater than the target value of 0.8, but is the lowest value that could be obtained without violating other constraints. The volumetric efficiency was increased by 17.9 percent over the unconstrained waverider shape to a value of 0.112. This increase in volumetric efficiency corresponded to only a 2.75 percent decrease in maximum lift-to-drag ratio, so the objective of obtaining a higher volumetric efficiency without suffering a large penalty in aerodynamic performance was achieved. Figure 2.5 shows the trade-off between volumetric efficiency and aerodynamic performance. This figure shows the lift-to-drag ratio and volumetric efficiency of the straight and cranked leading-edge waveriders as well as the optimized waverider with no volumetric constraints imposed (labeled as "unconstrained"). Also shown on the figure are two other cases with different volumetric constraints specified. These designs, labeled "constrained waverider" and "waverider designed close to apex of cone" are different waverider shapes that were not selected for the model design. Note that the waverider designed close to the apex of the cone provides high volumetric efficiency, but poor aerodynamic performance. Such configurations are not desirable because the departure from the aerodynamic performance of the unconstrained optimized case is too great. The lower surface of the straight-wing configuration has a slight convex curvature which facilitates integration of the propulsion system. The length of the waverider configuration was selected to be 24.0 inches based on the size of the test section in the UPWT. The length of the generating cone was selected to be twice the length of the waverider configuration. The selection of these dimensions fixes the location of the waverider on the conical shock wave. A selection of different locations on the conical shock wave would result in waveriders with much different structural characteristics. A diagram of the location of the waverider on the conical shock wave is shown in figure 2.6. Table 2.1 summarizes the characteristics of the straight-leading-edge waverider.

A 3-view drawing and an oblique view of the cranked-leading-edge waverider shape is shown in figure 2.7. The cranked-wing shape was designed by altering the leading edge of the straight-wing waverider and then using the design code to generate the waverider shape from the given leading edge, without running the optimization routine. The cranked leading edge still lies on the same conical shock wave produced by the generating cone used to design the straight-wing waverider. The cranked-wing waverider has similar characteristics to the straight-wing waverider. The span-to-length ratio is 0.932, which represents a significant increase in the aspect ratio. This increase in aspect ratio should provide a significant improvement in the subsonic and transonic performance over the straight-wing configuration, while maintaining the structural characteristics of the straight-wing waverider near the center line of the configuration. The volumetric efficiency of this configuration is 0.108 with a maximum lift-to-drag ratio of 6.743. The slight convex curvature of the bottom surface is maintained towards the center line of the model. The dihedral angle of the aft cranked section is approximately 28 degrees. The characteristics of the cranked leading edge waverider shape are summarized in table 2.2.

2.5 Description of Wind Tunnel Model Components

The "pure" waverider forebodies were designed based on the MAXWARP waverider shapes, with two slight modifications which were necessary to facilitate the integration of model support hardware as well as additional components. Additional volume was added to the upper surface of the configurations in order to accommodate the sting and balance necessary to measure the aerodynamic loads on the model during testing. Additional volume was added to the upper surface rather than the lower surface because previous research indicates that modifications to the lower surface have an effect on the propulsion/airframe integration characteristics of the waverider.[5] Figures 2.8 and 2.9 show photographs of the straight-wing and cranked-wing waverider shapes with the additional volume added to the upper surface. The lower surface was modified slightly by creating an expansion surface that acts as a contoured nozzle near the center line of the model which begins approximately 22 inches from the nose of the configuration. The lower surface follows the waverider streamsurface to this point. This modification was made in order to facilitate the integration of engine components. Figure 2.10 shows a photograph of the lower surface of the cranked-wing waverider with the expansion on the aft end of this surface. The configuration was designed such that the leading edge shapes are identical to the point where the cranked wings begin to curve upward along the conical shock wave. In order to minimize model changes, a configuration with a common center body and interchangeable wing tips was designed. This allows for the testing of both waverider shapes without removing the entire model. Figures 2.11 and 2.12 illustrate this by showing a comparison of the planform shapes and base views, respectively, of the two waverider shapes.

Canopies and propulsion systems components were designed for the waverider-based configuration. The first canopy was designed with faceted surfaces to resemble a realistic canopy for a hypersonic vehicle. Because of the design of the model, a canopy-off configuration could not be tested. Therefore, a smooth ogive canopy was designed in order to provide a comparison of the aerodynamic performance between the two canopies. These canopies are referred to as the faceted and smooth canopies, respectively. Figures 2.8 and 2.9 show the models with the smooth canopy attached, while figure 2.13 shows the faceted canopy attached to the model. The smooth canopy is also shown in figure 2.14. The engine package included an inlet and nozzle/expansion ramp. The engine-on data will provide an indication of the effect of modifying the waverider airframe to integrate a propulsion system and is not intended to provide an accurate simulation of propulsion effects. The inlet consists of a compression ramp with two side walls. Two different nozzle/expansion ramps were designed, one for use with configurations that do not have control surfaces attached and the second for use with configurations with control surfaces integrated. These are referred to as the "short" and "long" nozzles, respectively. Identical nozzles with static pressure taps were also fabricated in order to obtain surface pressure measurements on the nozzle. The non-instrumented ramps were used when obtaining force and moment data. Figure 2.13 also shows the engine components integrated with the model.

Control surfaces were designed and fabricated in order to examine their effects on waverider aerodynamic performance as well as the effectiveness of the control concept. The control surfaces close the blunt base of the configuration to a sharp trailing edge. Elevons were designed for angles of 0, positive 20 (trailing edge down) and negative 20 degrees. Because of the severe closure angle and the method by which the control surfaces were attached to the waverider shape, different parts were fabricated for each fixed angle. A set of outboard ailerons for the same three angles was designed for the straight wing. Because of the curved surface of the cranked wing and the small thickness of the outer leading edge, the set of ailerons for the cranked-wing configuration consisted of an inboard aileron, which remained fixed at zero degrees, and a set of outboard ailerons, which were deflected at 0, positive 20 and negative 20 degrees. A vertical tail surface was also designed in order to augment directional stability. Figures 2.13 and 2.14 show photographs of the model components.

Figure 2.15 shows an exploded view of the model components, indicating how the components fit together with the two waverider shapes. The design allowed for testing of the straight-wing and cranked-wing pure waverider configurations, which are defined as configurations with no engine components or control surfaces and with the smooth canopy attached. Various combinations of the waverider with different vehicle components could also be tested up to and including the fully-integrated waverider-derived configurations, which are defined as configurations with engine components, all control surfaces and with the faceted canopy integrated. Table 2.3 shows a list of reference quantities for each configuration tested. Detailed geometry specifications may be obtained from the author upon request.

Waverider Length	24.0 inches
Cone Length	48.0 inches
Span/Length	0.824
Base-Height/Length	0.0923
Volumetric Efficiency	0.112
Planform Area, S_{ref}	1.894 ft^2
Predicted Maximum L/D	6.859

Table 2.1. Characteristics of Straight-Wing Waverider Designed by MAXWARP.

Waverider Length	24.0 inches
Cone Length	48.0 inches
Span/Length	0.932
Base-Height/Length	0.0923
Volumetric Efficiency	0.108
Planform Area, S_{ref}	2.052 ft^2
Predicted Maximum L/D	6.743

Table 2.2. Characteristics of Cranked-Wing Waverider Designed by MAXWARP.

Configuration	S_{ref} (ft^2)	Span (in.)	Length (in.)	Base Area (ft^2)
Straight Leading Edge Model with No Engines or Controls.	1.894	19.80	24.0	0.1580
Straight Leading Edge Model with Engines. (No Controls)	1.894	19.80	24.0	0.1481
Straight Leading Edge Model with Engines and Controls	2.202	19.80	26.597	0.0194
Cranked Leading Edge Model with No Engines or Controls	2.052	23.016	24.0	0.1860
Cranked Leading Edge Model with Engines. (No Controls)	2.052	23.016	24.0	0.1745
Cranked Leading Edge Model with Engines and Controls.	2.346	23.016	26.597	0.0194

Table 2.3. Reference Quantities for Various Configurations.

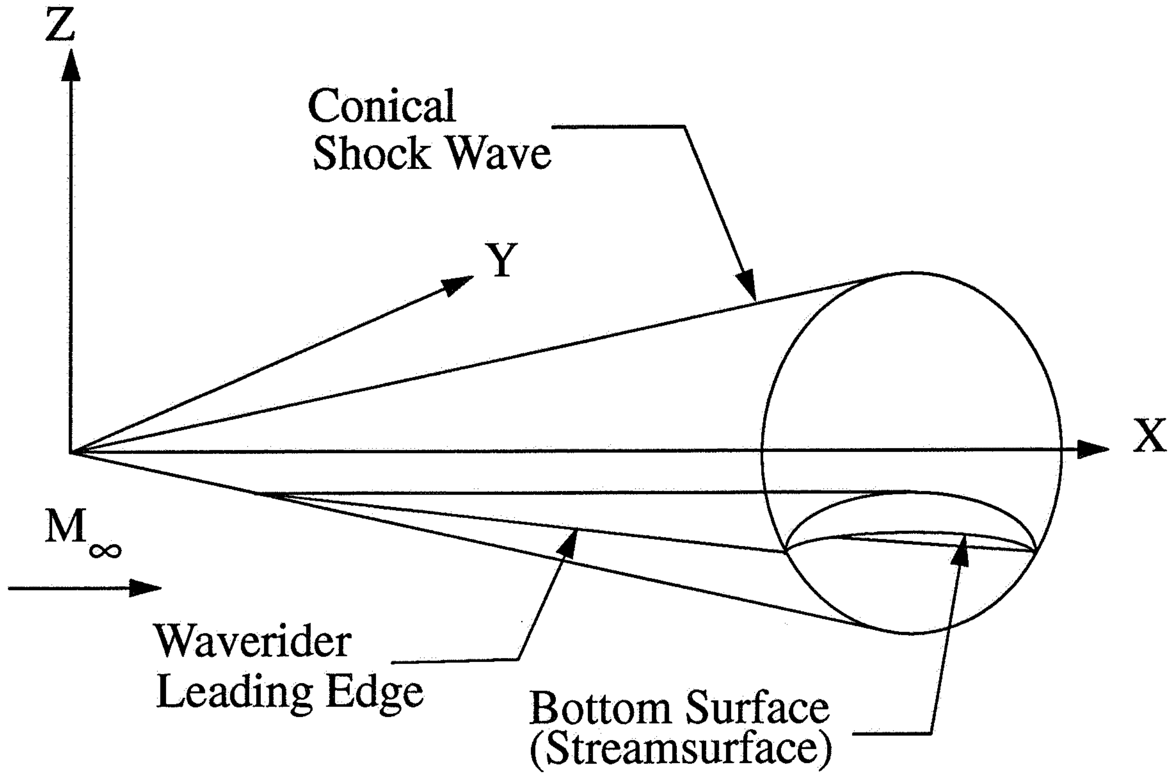

Figure 2.1: Design of a conical-flow derived waverider.

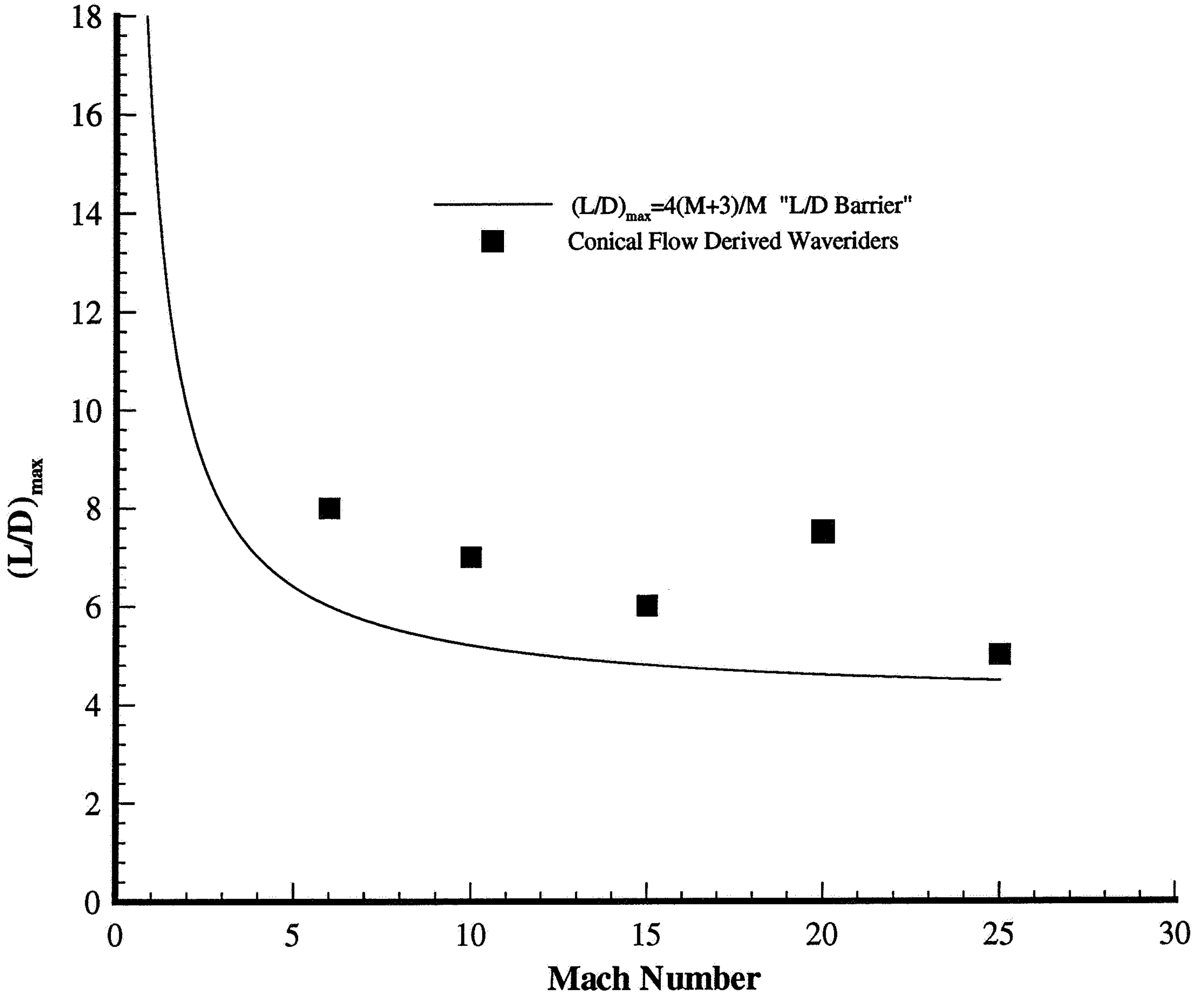

Figure 2.2. Comparison of L/D_{max} Values of Conventional Vehicles vs. Waveriders.

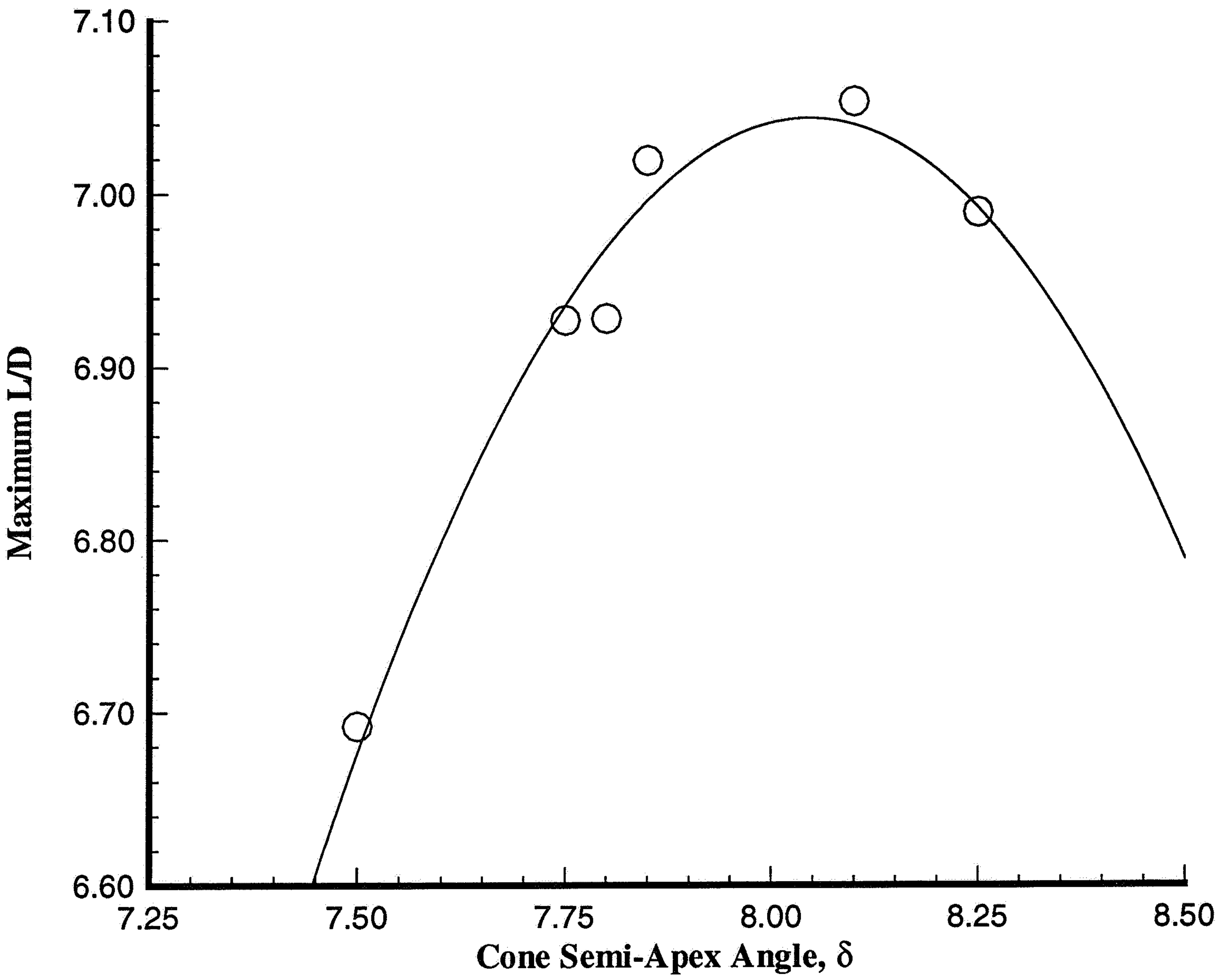

Figure 2.3. Variation of Maximum L/D with Cone Semi-Apex Angle.

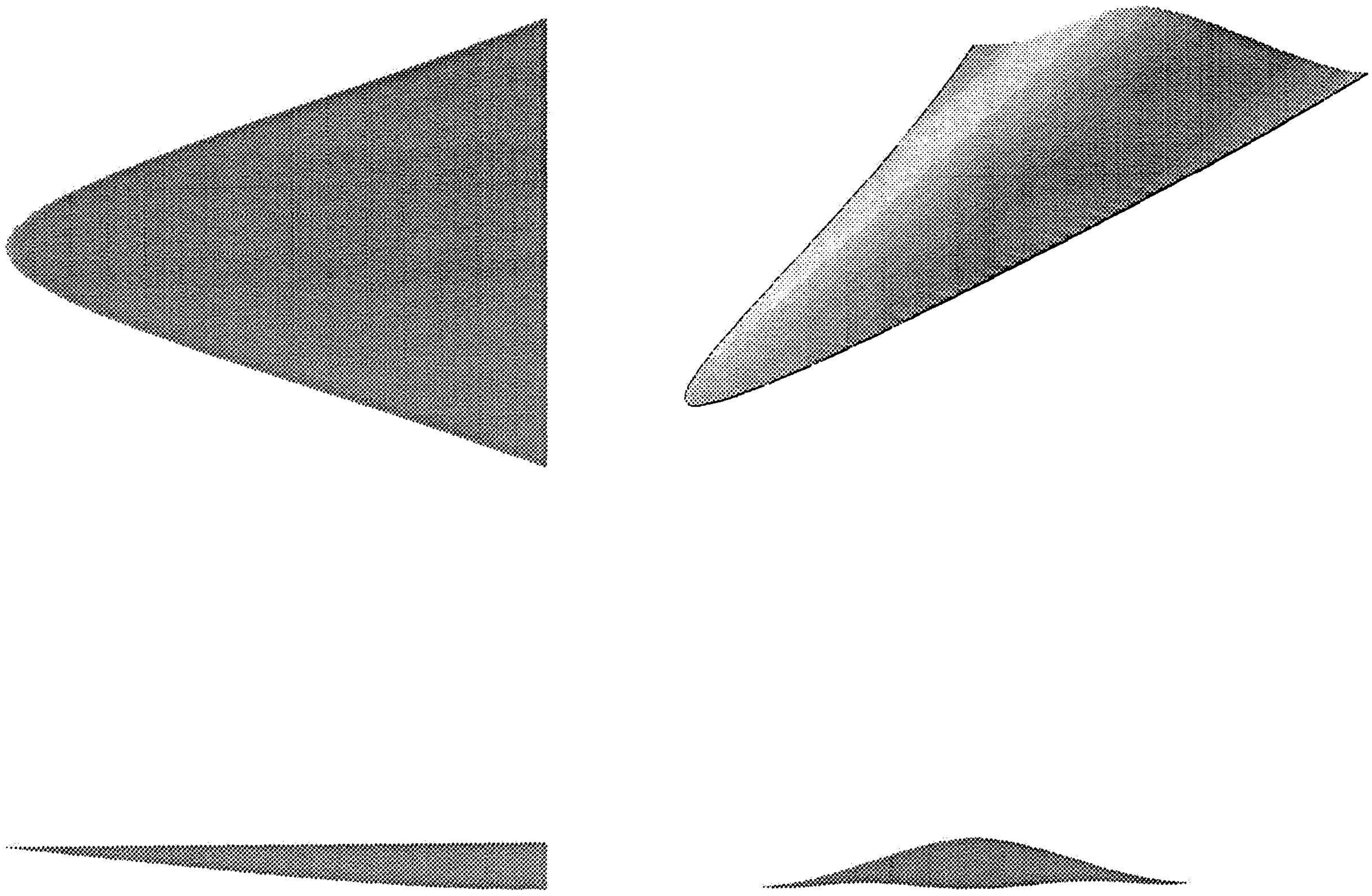

Figure 2.4. Straight-Wing Waverider Designed by MAXWARP.

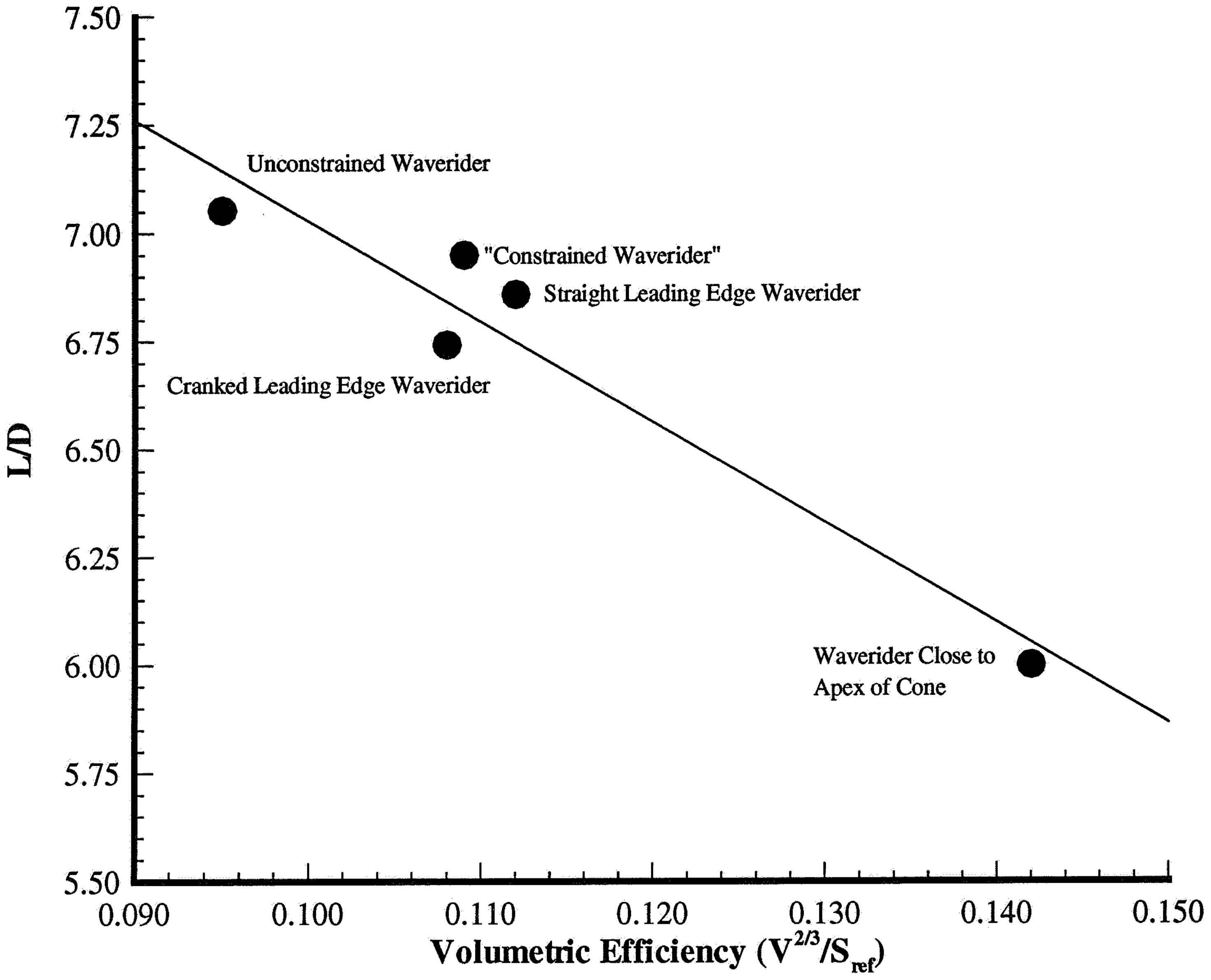

Figure 2.5. Waverider L/D Vs. Volumetric Efficiency.

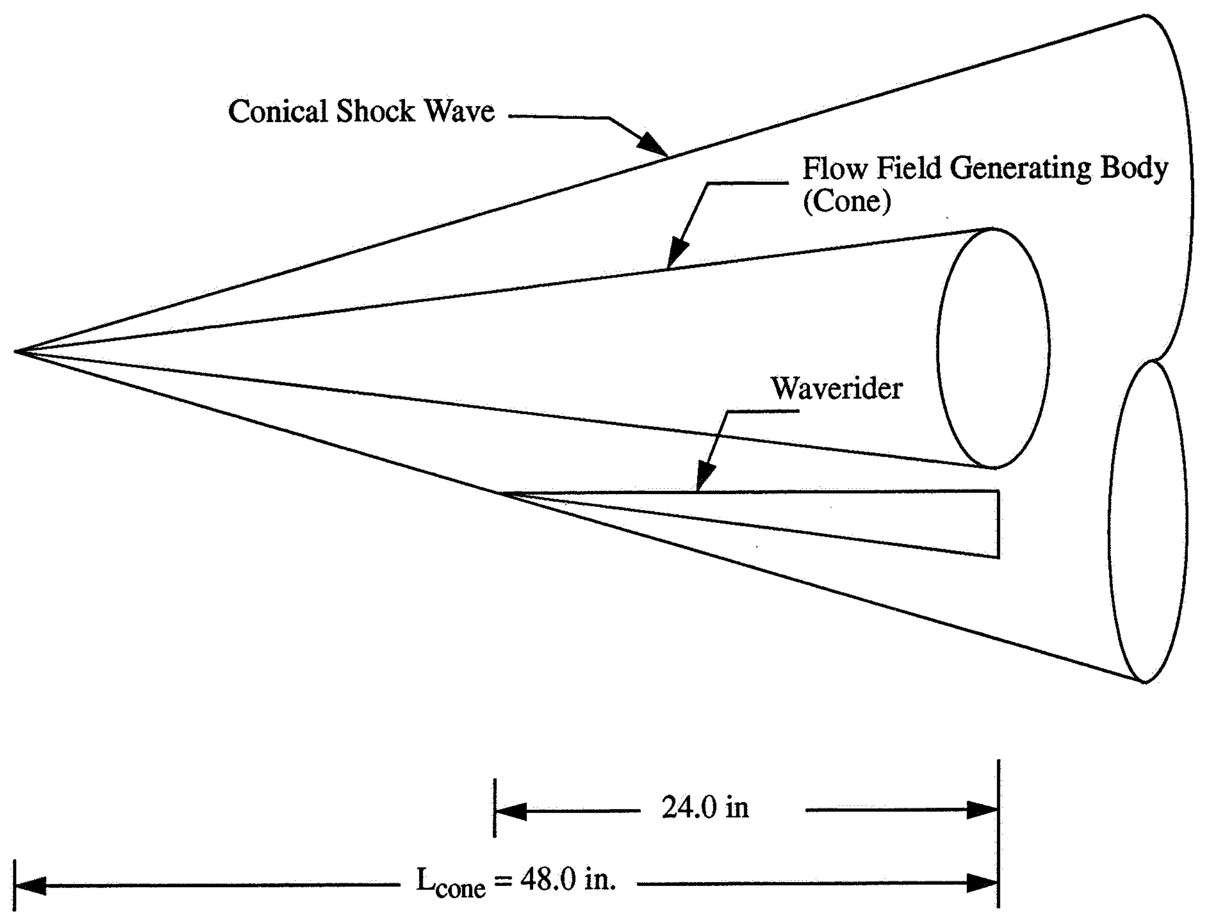

Figure 2.6. Location of Waverider on Conical Shock Wave

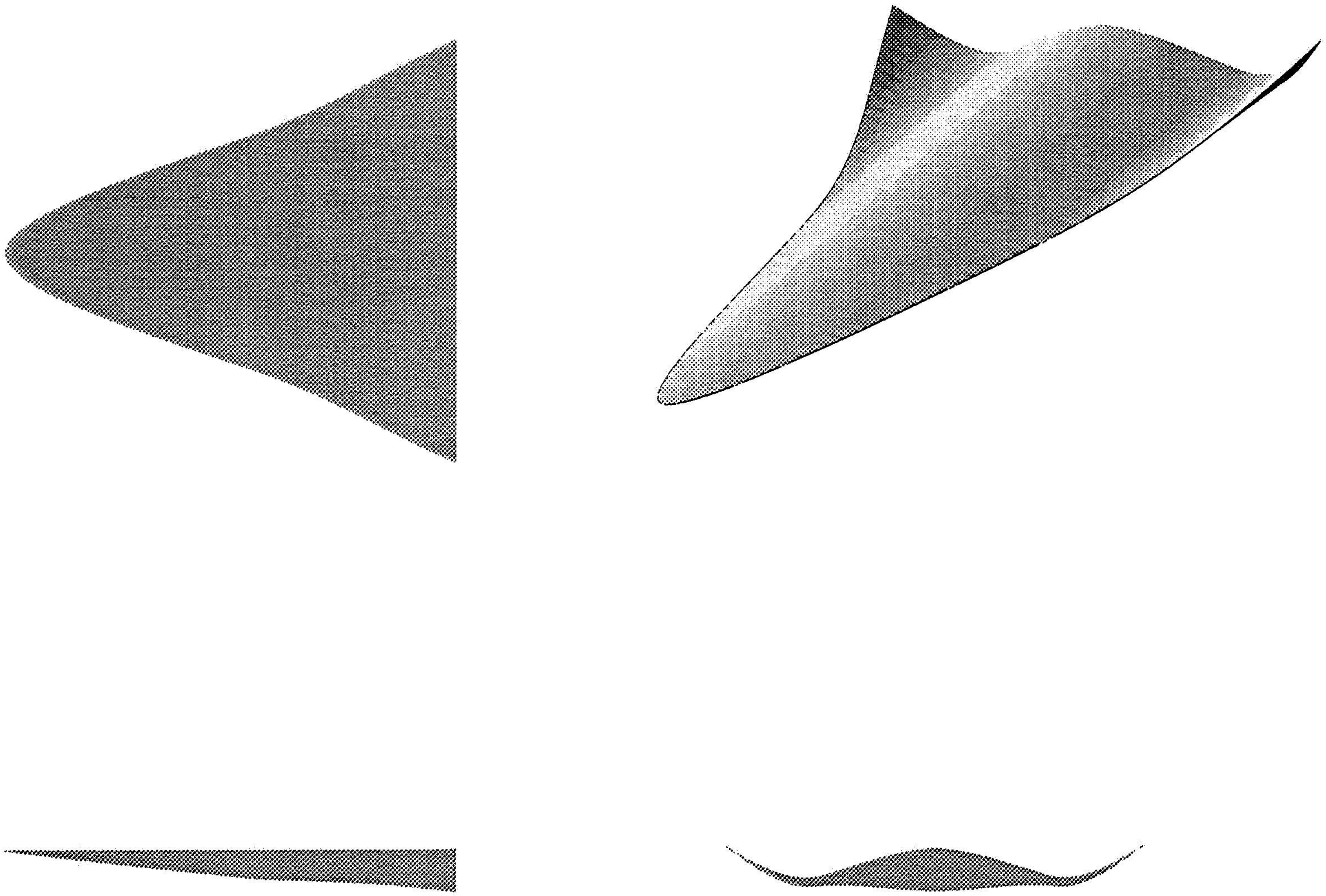

Figure 2.7. Cranked-Wing Waverider Designed by MAXWARP.

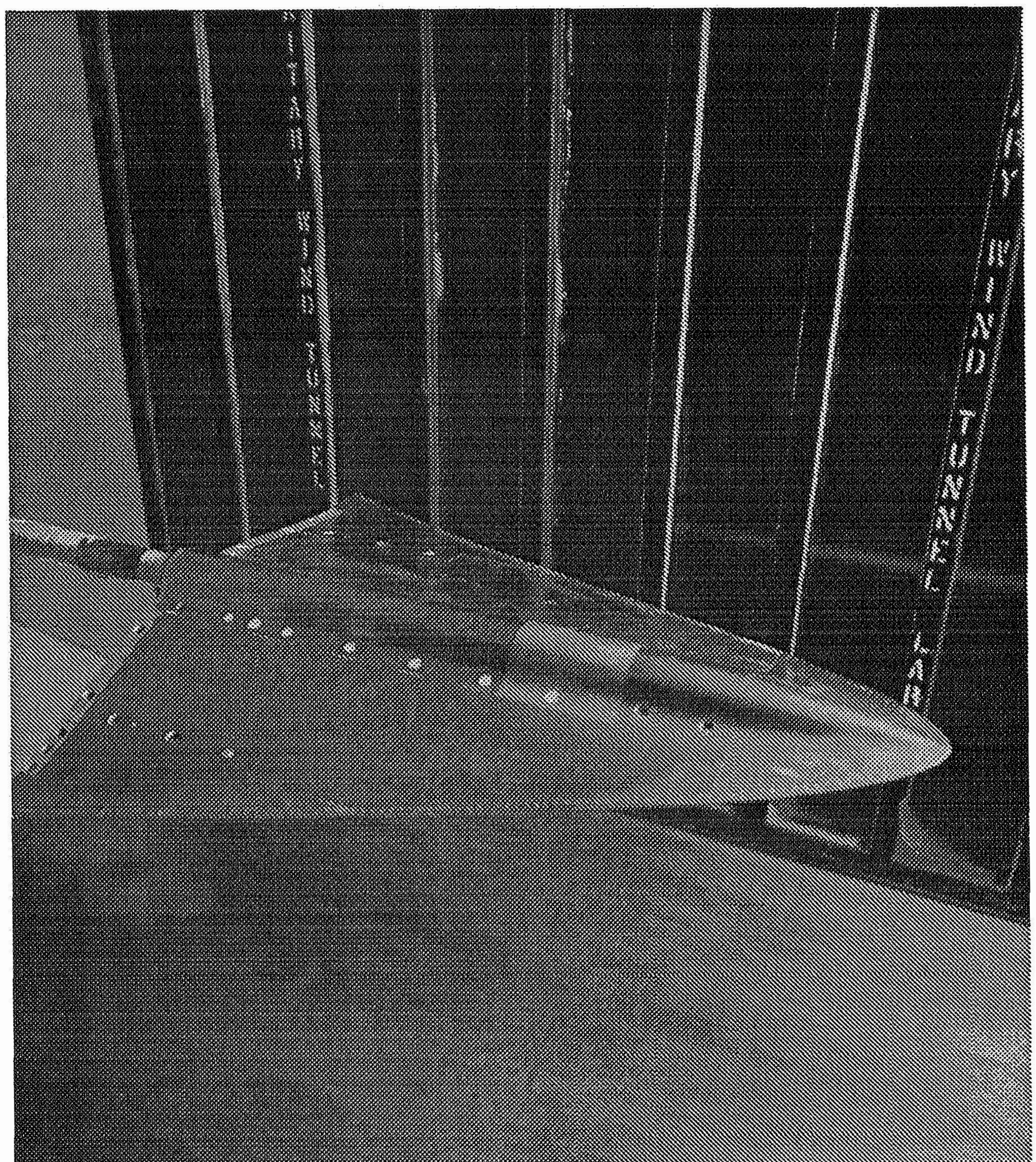

Figure 2.8. Straight-Wing Waverider Model in UPWT.

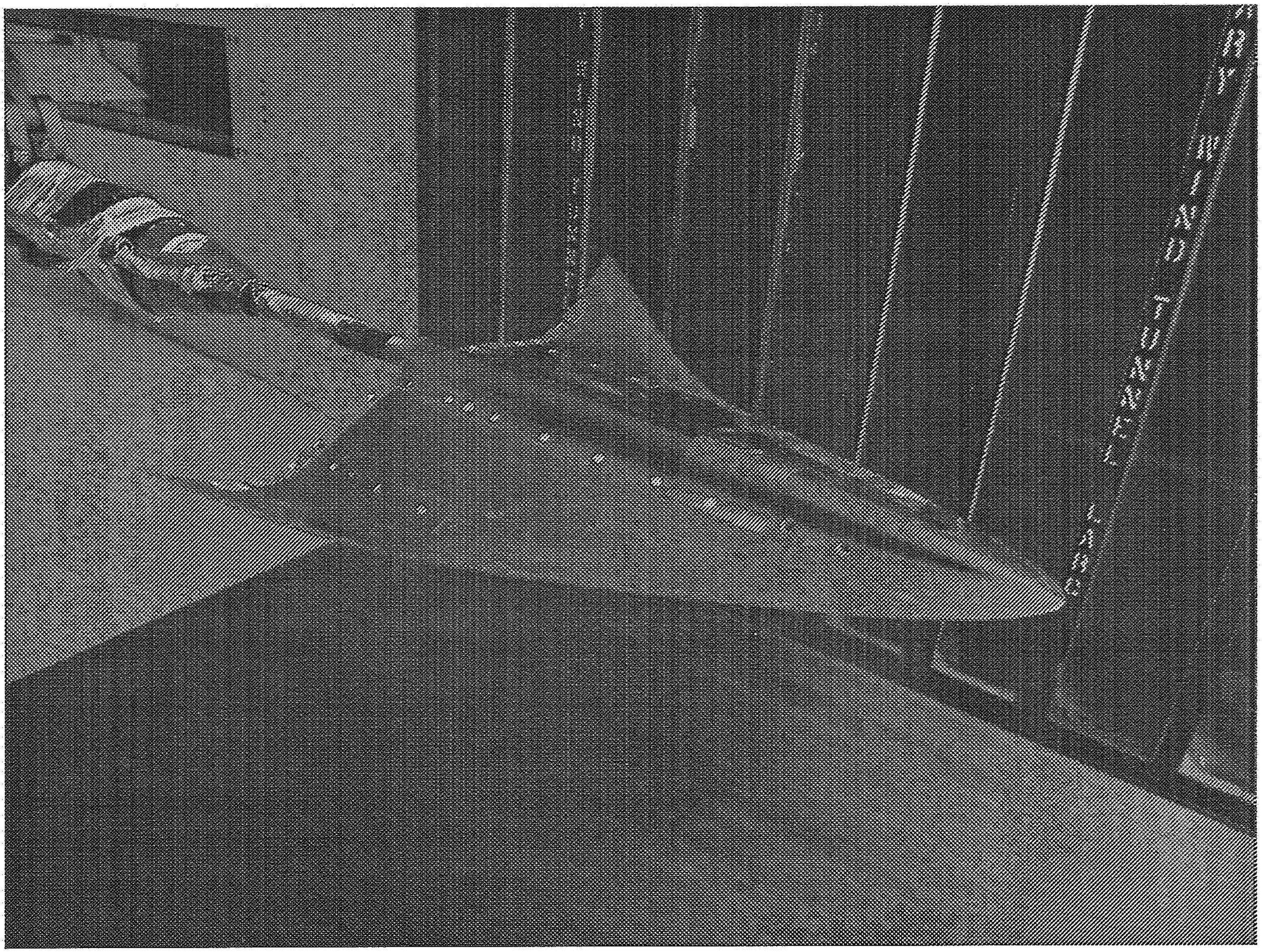

Figure 2.9. Cranked-Wing Waverider Model in UPWT.

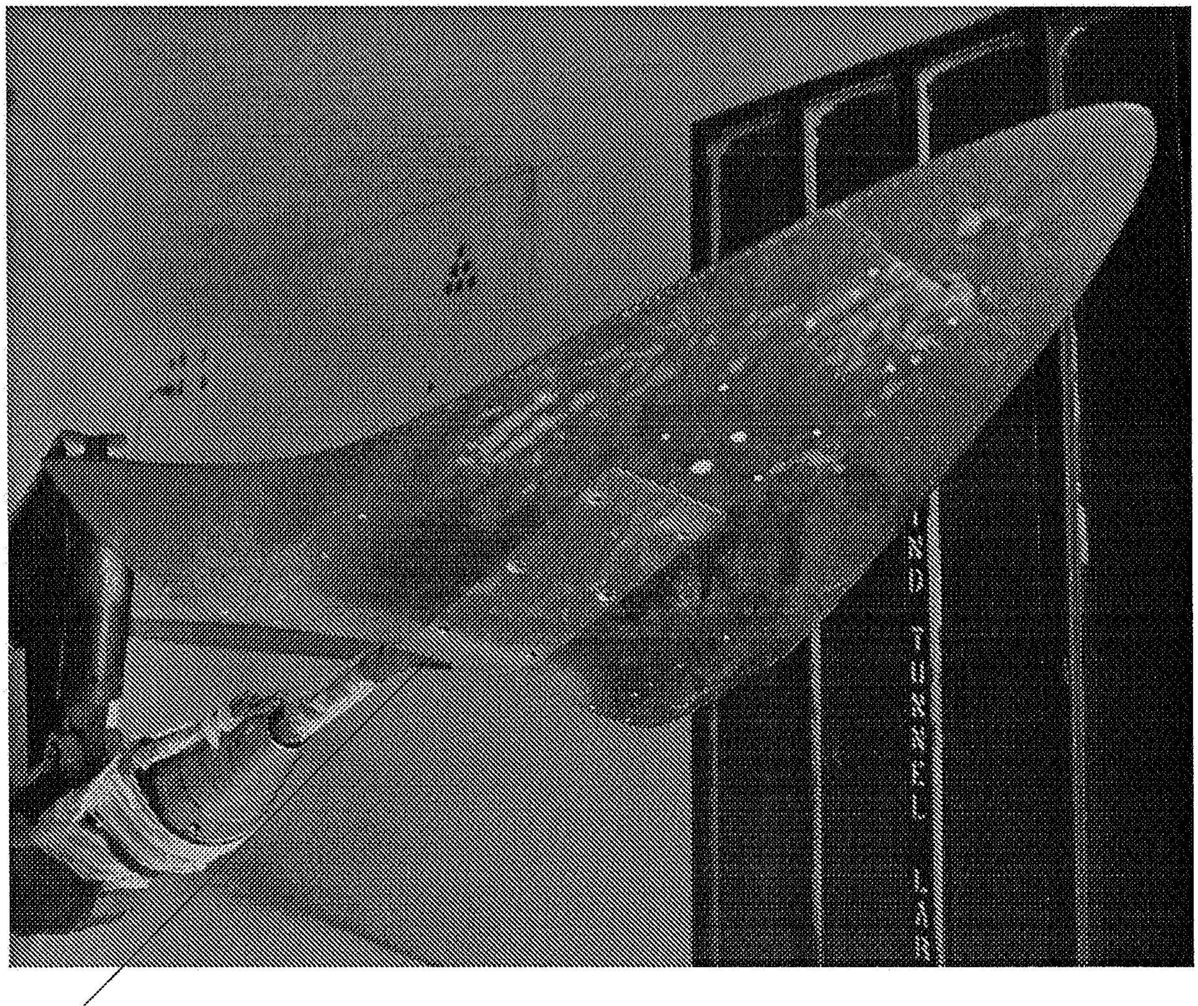

Expansion Ramp

Figure 2.10. Photograph of Lower Surface of Cranked-Wing Waverider Model.

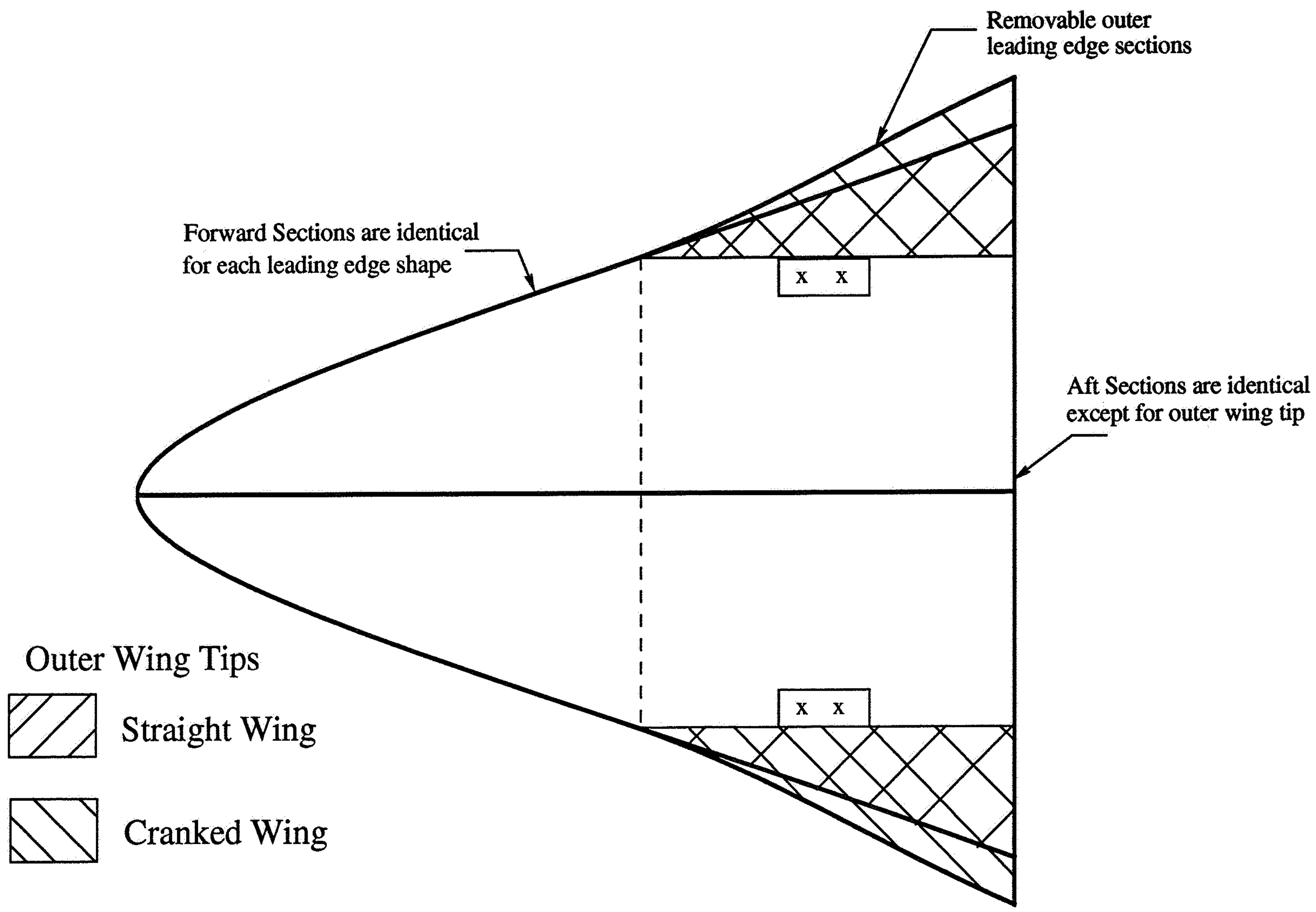

Figure 2.11. Comparison of Planform Shapes of Two Waverider Shapes.

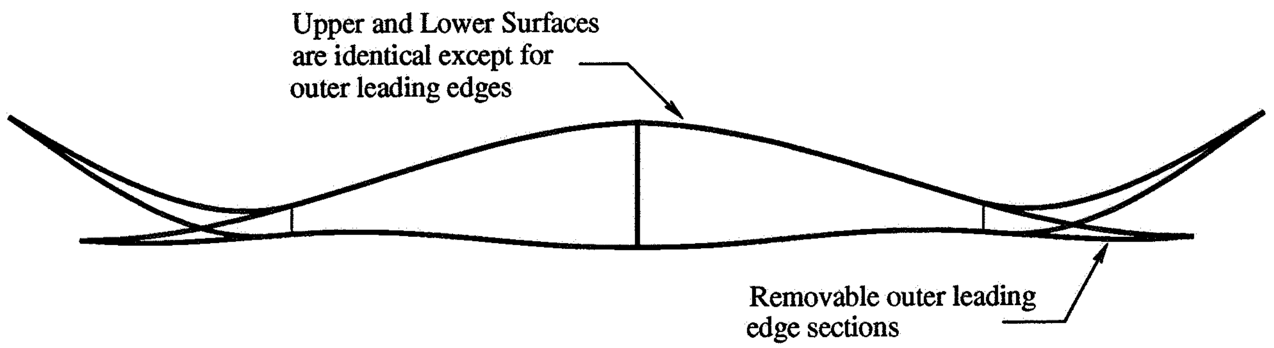

Figure 2.12. Comparison of Base Views of Two Waverider Shapes.

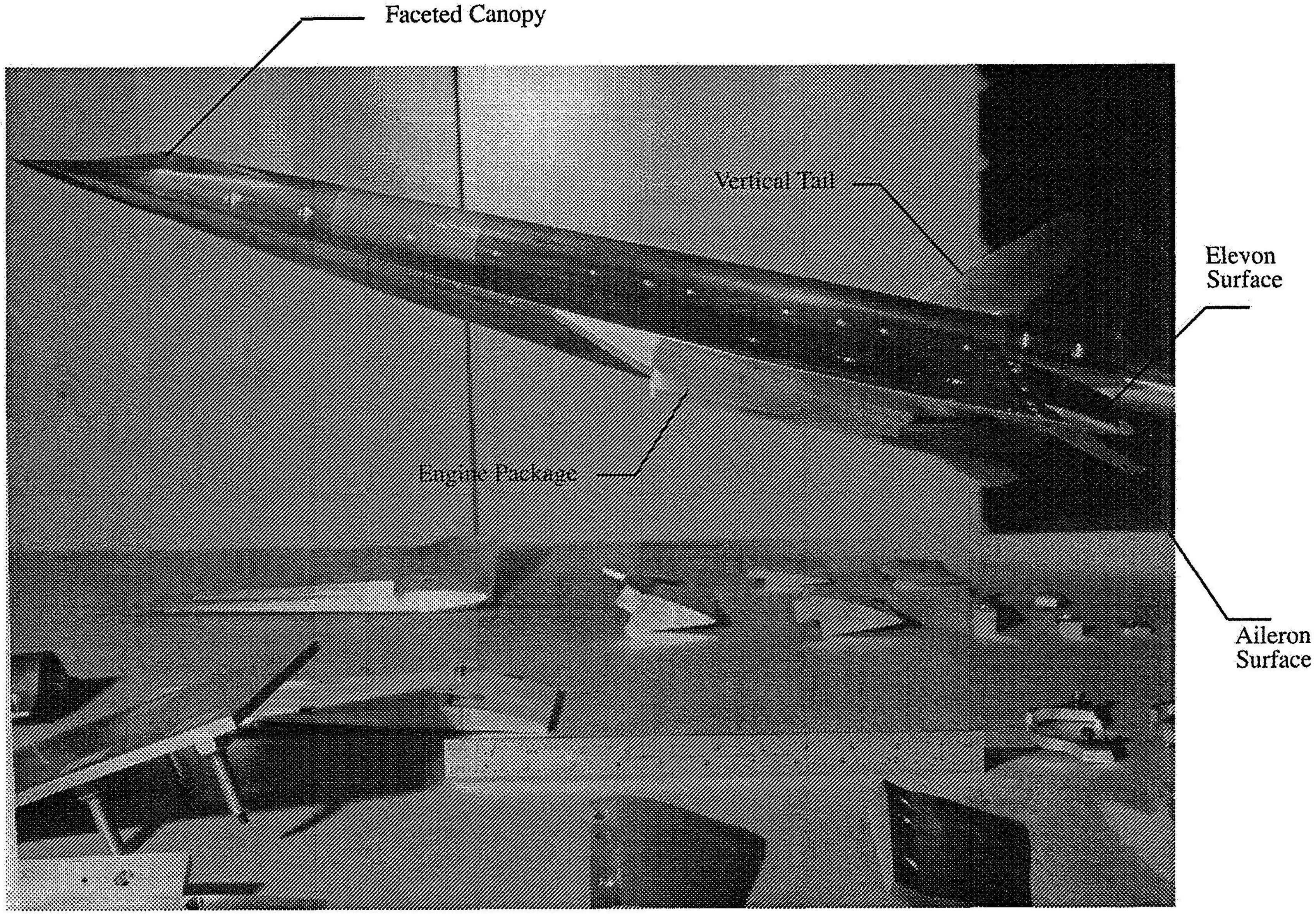

Figure 2.13 Photograph of Waverider Model with Faceted Canopy, Engine Components and Control Surfaces Attached.

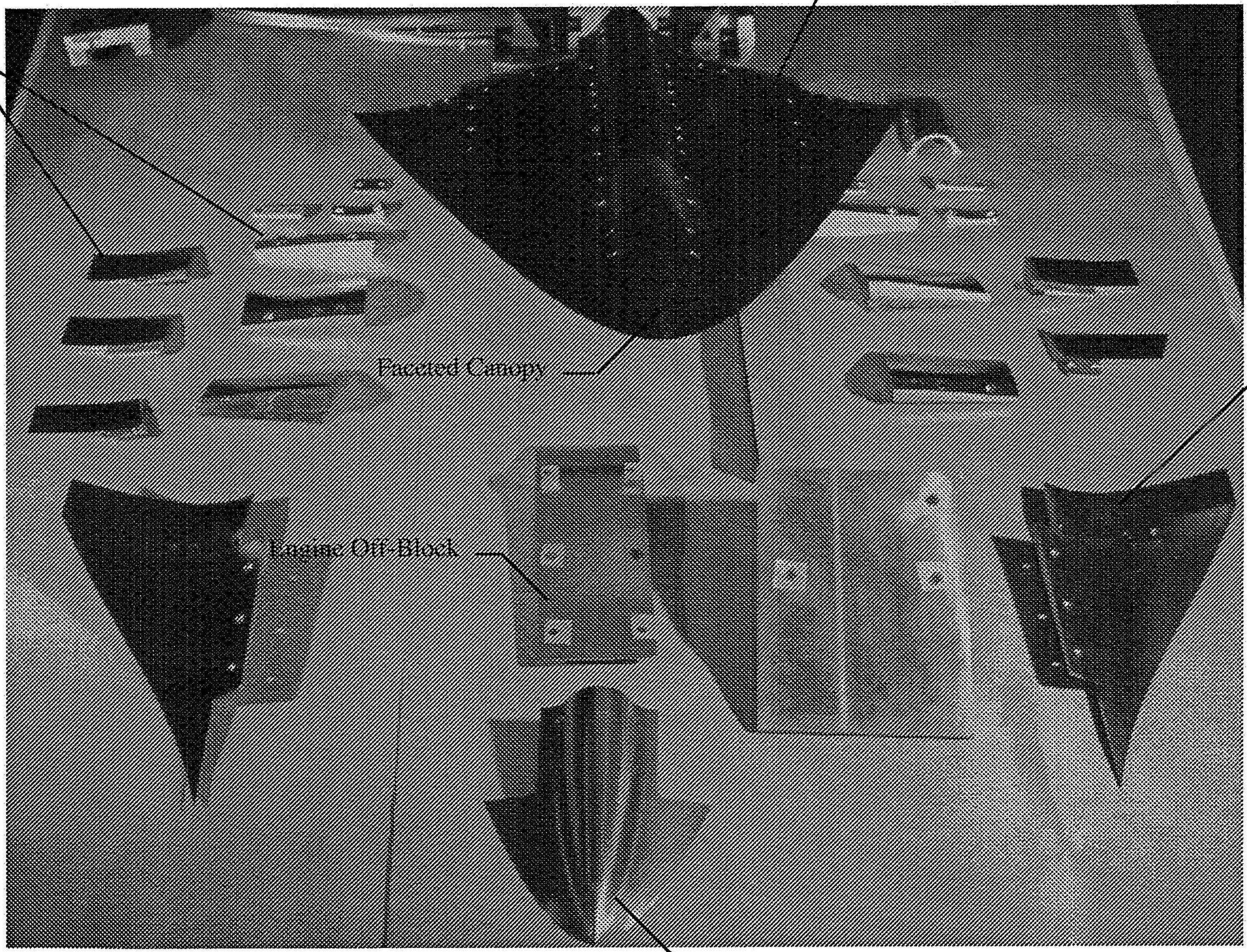

Figure 2.14. Photograph of Waverider Model with Various Components

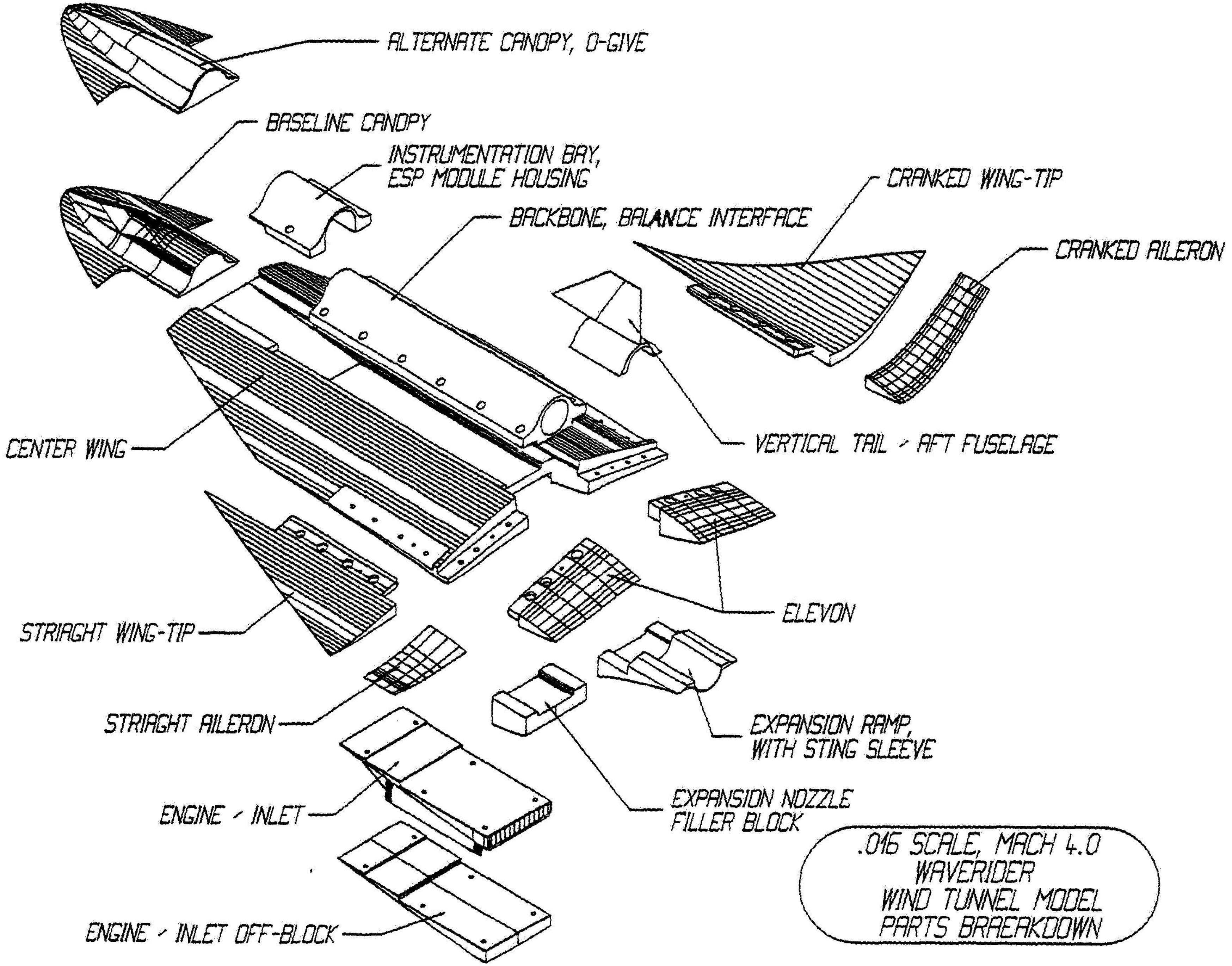

Figure 2.15. Exploded View of Waverider Model Parts.

CHAPTER 3
EXPERIMENTAL METHOD

3.0 Summary

The waverider model was tested in the high Mach number test section of the Unitary Plan Wind Tunnel (UPWT) at NASA Langley Research Center. The test configurations ranged from the baseline waverider configurations to the fully-integrated hypersonic waverider-derived cruise vehicles. The test conditions included pitch polars at Mach numbers of 2.3, 3.5, 4.0, 4.2 and 4.63. Data were also taken at a sideslip angle of 3^o in order to examine the lateral-directional stability characteristics of the configurations. The model was instrumented with a 6-component strain gauge balance to obtain force and moment data. Static pressure tubes were placed at the blunt base in order to measure the base pressures as well as sting cavity pressures. Several runs were repeated with a nozzle surface instrumented with static pressure taps in order to measure pressures on this surface. Flow visualization data, including schlieren and vapor-screen photographs, were also obtained. The raw force data were corrected for flow angularity as well as base and chamber pressures.

3.1 Facility Description

The facility utilized in this study was the high Mach number test section of the Unitary Plan Wind Tunnel (UPWT) at NASA Langley Research Center. The UPWT is a closed-circuit, continuous-flow pressure tunnel with two 4x4x7-foot test sections. The Mach number range of the facility is 1.47 to 4.63, with a range in the high Mach number test section of 2.3 to 4.63. Continuous variation of Mach number is achieved by using axisymmetric sliding block nozzles to vary the nozzle throat-to-test section area ratio. The Reynolds number range of this facility is 0.5×10^6 to 8.0×10^6 per foot. However the nominal Reynolds number for most tests is 2.0×10^6 per foot. Figure 3.1 shows a diagram of the layout of this facility. A detailed description of the UPWT can be found in reference 13.

3.2 Test Configurations and Conditions

The configurations tested range from the straight and cranked waverider shapes with no engines or control surfaces attached to the fully-integrated waverider-derived vehicles. The test configurations were chosen to show the pure waverider performance, to isolate the effects on waverider aerodynamic performance and stability of the canopy, engine package and control surfaces and to show the aerodynamic performance and stability characteristics of the fully-integrated configurations. Table 3.1 shows a list of configurations tested. For each configuration listed, a configuration number, leading edge shape, canopy type, elevon deflection angle and aileron deflection angle is shown. Note that a positive aileron or elevon deflection corresponds to a trailing edge down deflection, while a negative value corresponds to a trailing edge up deflection. Additionally, the configurations are labeled as either engine-off or engine-on. The test type for the first configuration is labeled as "flow angles" because this configuration was tested in upright and inverted positions for the purpose of obtaining estimates for the flow angles at each Mach number in the test section. (This process is described in further detail in section 3.3). Otherwise, for each configuration, either 6-component force and moment data, nozzle pressure data or vapor-screen photographs were obtained. Schlieren photographs were taken along with force and moment runs.

The test conditions were chosen to investigate the performance and stability of each configuration at both the design Mach number and at off-design Mach numbers. Data were obtained at Mach numbers of 2.3, 4.0 and 4.63 for all configurations studied and, additionally, at Mach numbers of 3.5 and 4.2 for some configurations. Data were obtained at a freestream Reynolds number of $2.0\text{x}10^6$ per foot and, in some cases, at Reynolds numbers of $1.5\text{x}10^6$ per foot and $3.0\text{x}10^6$ per foot in order to investigate the effects at off-design Reynolds numbers. Data were obtained over an angle-of-attack range of -6° to 10° and at sideslip angles of 0° and 3°. Data were obtained for configuration number 2 over a sideslip-angle range of -5° to 5° at Mach numbers of 2.3 and 4.63 and 0° angle of attack. The data for yawing moment and rolling moment coefficients at each condition are plotted versus sideslip angle in figure 3.2. A non-zero value of roll and side force is observed at 0° sideslip due to the difficulty in measuring the balance-to-model roll misalignment angle precisely. The values for each parameter are nearly linear over the range of sideslip angles investigated. From these data, it was concluded that stability derivatives could be estimated by obtaining data at only two sideslip angles. Table 3.2 shows the run schedules used in the test. Run schedule 1 was used for configurations 1 through 7; run schedule 2 was used for configurations 8 through 18 and run schedule 3 was used for configurations 19 through 22. Run schedule 2 was also used for vapor screen runs with the exception that photographs were only taken at a 0° sideslip angle. Transition grit was applied to the model in order to ensure a fully-turbulent boundary-layer at the conditions specified. The grit size was specified as number 35 grit and was placed along the top and bottom surfaces of the model at a distance of 0.4 inches aft of the leading edge in the streamwise direction. Recall that a fully-turbulent boundary-layer specification was made in MAXWARP when the waverider shapes were designed.

3.3 Instrumentation and Data

The data obtained from the wind-tunnel tests included 6-component force and moment data, static pressure readings on the blunt base of the model, static pressure data on the nozzle surfaces and flow visualization data. The model was instrumented with a 6-component internal balance to obtain force and moment data. The balance utilized in this case was the NASA-LaRC-designated UT-50-B balance. The moment reference center for all configurations was located 16.623 inches aft of the nose for all configurations.

A total of eleven 5-psi pressure transducers were used to measure the static pressure along the blunt base of the configurations and in the cavity surrounding the sting. Figure 3.3(a) shows a diagram of the placement of static pressure tubes along the base of configurations with no control surfaces or engine components. The integrated areas used and pressure taps averaged to compute force coefficients to correct for base drag are also shown on the figure. The end of each tube was placed against, but not touching, the model surface at the locations indicated. The tubes were secured to the sting and connected to pressure transducers located outside of the test section. For configurations with no control surfaces, a 0.09” diameter tube with holes drilled in it was secured to the blunt base and connected to another sting-secured pressure tube. This tube provided another reading of the average static pressure along the blunt base towards the outer wing tip. The same number of base pressure measurements were taken for configurations with no control surfaces, but with engine components. The position of some tubes was changed slightly to ensure that they were not behind the surface of the nozzle. For configurations with both engines and control surfaces, only 2 base and 2 chamber pressure measurements were taken. The placement of static-pressure tubes and integrated areas used for this case is shown in figure 3.3(b). A 32-port, 5-psi external ESP module was used to measure the static pressure on the nozzle surface for four runs. Figures 3.4 (a) and (b) show drawings with the location of pressure taps on the nozzle surfaces for the short and long nozzles, respectively. Recall that the short nozzle is used with configurations that have no control surfaces, while the long nozzle is used with configurations that have control surfaces integrated. There were a total of 12 pressure taps on the short nozzle and 24 pressure taps on the long nozzle. Integrated surface areas used to correct for nozzle surface pressures are shown in table 3.3. In the table, X corresponds to the streamwise direction, Y to the spanwise direction and Z to the vertical direction. Therefore, the ΔX-Y area is the component applied to normal force and ΔY-Z is the component applied to axial force. As noted in figures 3.4 (a) and (b), taps 1-12 are present on the short nozzle surface, while taps 1-24 are present on the long nozzle surface.

Schlieren and vapor-screen photographs were taken in order to examine flow-field features including the shock attachment characteristics for various configurations. Prior to taking vapor-screen photographs, the model surface was painted black and 5 locations were identified on the model surface to be illuminated by the laser light sheet. The laser was positioned outside of the test section window during runs and the light sheet was projected across the model surface in the spanwise direction, illuminating one cross section at a time. The light sheet locations are shown in figure 3.5. The camera was mounted inside of the test section above and behind the model.

The force and moment data were corrected for flow angularity and base pressure. Calibration data available for the UPWT indicates that the flow in both test sections has an upflow angle generally within 0.5 degrees.[13] In order to obtain values for the flow angle at each Mach number, configuration 1 was run in an upright and inverted (rolled 180^o about the model center line) position. Angle of attack sweeps were run at each Mach number in each position. The flow angles were computed after the initial set of runs and used for the remainder of the runs to correct angle of attack. As an example, figure 3.6 illustrates the computation of flow angle at Mach 4.63 by comparison of the normal force coefficients versus angle of attack for the upright and inverted configurations. The axial force data were corrected for base and chamber pressures before computing lift and drag coefficients. Since the blunt base will be eliminated by the addition of control surfaces in any realistic waverider-derived configuration, it is necessary to eliminate the effect of the base in the force data. This is accomplished by subtracting measured values of base drag from axial force data and correcting the data to assume freestream pressure at the base. The integrated areas indicated in figures 3.3(a) and 3.3(b) were used to compute the component of axial force acting at the blunt base. The method of assuming freestream pressure at the base is consistent with the design code method and with previous studies showing predictions for waverider aerodynamic performance. Unless otherwise noted, all lift and drag coefficient data presented assume freestream pressure acting at the blunt base.

The accuracy of the UT-50-B balance, based on a recent calibration, is 0.5 percent of full-scale for each component to within 95 percent confidence. The full-scale load limits were: 600 lbf normal, 40 lbf axial, 1500 in-lbf pitching moment, 400 in-lbf rolling moment, 800 in-lbf yawing moment and 300 lbf side force. Using the method of root-mean-squares summation to combine independent error sources, this corresponds to a range of uncertainty in lift coefficient of 0.0053 at $\alpha=0^o$ to 0.0054 at $\alpha=10^o$ and an uncertainty range in drag coefficient of 0.00036 at $\alpha=0^o$ to 0.001 at $\alpha=10^o$ for the $M_\infty=4.0$ and $Re_\infty=2.0\times10^6$ per foot condition. The repeatability of measurements was observed to be better than these uncertainties. Therefore, differences less than these ranges observed in comparisons of data from different test configurations could be considered significant. However, comparisons between experimental data and independent measurements, such as CFD predictions, are only good to within to within these uncertainty ranges.

Config. No.	Wing Type	Canopy	Elevons	Ailerons	Engine/ Inlet	Test Type	Run Schedule
1	Cranked	Faceted	None	None	Off	Flow Angles	1
2	Cranked	Faceted	None	None	Off	Force/Moment	1
3	Straight	Faceted	None	None	Off	Force/Moment	1
4	Straight	Smooth	None	None	Off	Force/Moment	1
5	Cranked	Smooth	None	None	Off	Force/Moment	1
6	Cranked	Faceted	None	None	On	Force/Moment	1
7	Straight	Faceted	None	None	On	Force/Moment	1
8*	Straight	Faceted	0°	0°	On	Force/Moment	2
9*	Straight	Faceted	0°	0°	On	Force/Moment	2
10	Straight	Faceted	0°	+/-20°	On	Force/Moment	2
11	Straight	Faceted	+20°	+20°	On	Force/Moment	2
12	Straight	Faceted	+20°	0°	On	Force/Moment	2
13*	Cranked	Faceted	0°	0°	On	Force/Moment	2
14*	Cranked	Faceted	0°	0°	On	Force/Moment	2
15	Cranked	Faceted	0°	+/-20°*	On	Force/Moment	2
16	Cranked	Faceted	+20°	+/-20°*	On	Force/Moment	2
17	Cranked	Faceted	+20°	0°	On	Force/Moment	2
18	Cranked	Faceted	-20°	0°	On	Force/Moment	2
19	Cranked	Faceted	0°	0°	On	Pressures	3
20	Cranked	Faceted	+20°	+/-20°*	On	Pressures	3
21	Cranked	Faceted	-20°	0°	On	Pressures	3
22	Cranked	Faceted	None	None	On	Pressures	3
5	Cranked	Smooth	None	None	Off	Vapor Screen	2
4	Straight	Smooth	None	None	Off	Vapor Screen	2

* Configurations 8 and 13 were run without a vertical tail. All other controls-on configurations were run with a vertical tail

Table 3.1. Test Configurations

Run Schedule 1

Reynolds No. (Per Foot)	Mach No.	Alpha	Beta	Notes
1.5×10^6	4.0	sweep	0.0^o	Off-Design Reynolds number.
2.0×10^6	2.3	sweep	0.0^o, 3.0^o	underspeed
2.0×10^6	3.5	sweep	0.0^o	underspeed
2.0×10^6	4.0	sweep	0.0^o, 3.0^o	design point
2.0×10^6	4.2	sweep	0.0^o	overspeed
2.0×10^6	4.63	sweep	0.0^o, 3.0^o	overspeed
3.0×10^6	4.0	sweep	0.0^o	Off-Design Reynolds number.

Run Schedule 2

Reynolds No. (Per Foot)	Mach No.	Alpha	Beta	Notes
2.0×10^6	2.3	sweep	0.0^o, 3.0^o	underspeed
2.0×10^6	4.0	sweep	0.0^o, 3.0^o	design point
2.0×10^6	4.63	sweep	0.0^o, 3.0^o	overspeed

Run Schedule 3

Reynolds No. (Per Foot)	Mach No.	Alpha	Beta	Notes
2.0×10^6	2.3	sweep	0.0^o,+/- 3.0^o	underspeed
2.0×10^6	4.0	sweep	0.0^o,+/- 3.0^o	design point
2.0×10^6	4.63	sweep	0.0^o,+/- 3.0^o	overspeed

Table 3.2. Run Schedules used in Wind Tunnel Testing.

Tap #	ΔX (in.)	ΔY (in.)	ΔZ (in.)	ΔX-Y Area (in^2)	ΔY-Z Area (in^2)
1	0.0	0.566	0.503	0.0	0.285
2	0.0	0.388	0.503	0.0	0.170
3	0.0	0.339	0.503	0.0	0.171
4	0.00	0.507	0.503	0.0	0.255
5	1.142	0.566	0.396	0.646	0.224
6	1.142	0.388	0.396	0.386	0.134
7	1.142	0.339	0.396	0.387	0.134
8	1.142	0.507	0.396	0.579	0.201
9	0.761	0.566	0.259	0.431	0.147
10	0.761	0.388	0.259	0.257	0.088
11	0.761	0.339	0.259	0.258	0.088
12	0.761	0.507	0.259	0.386	0.131
13	0.762	0.566	0.224	0.431	0.127
14	0.762	0.388	0.224	0.257	0.076
15	0.762	0.339	0.224	0.258	0.076
16	0.762	0.507	0.119	0.386	0.060
17	0.762	0.566	0.199	0.431	0.133
18	0.762	0.388	0.199	0.257	0.067
19	0.762	0.339	0.105	0.258	0.036
20	0.762	0.507	0.0	0.386	0.0
21	0.761	0.566	0.262	0.431	0.148
22	0.761	0.388	0.262	0.257	0.089
23	0.761	0.339	0.0	0.258	0.0
24	0.761	0.507	0.0	0.386	0.0

Coordinate Directions: X: Streamwise, Y: Spanwise, Z: Vertical.

Table 3.3. Integrated Areas for Nozzle Surface Pressures.

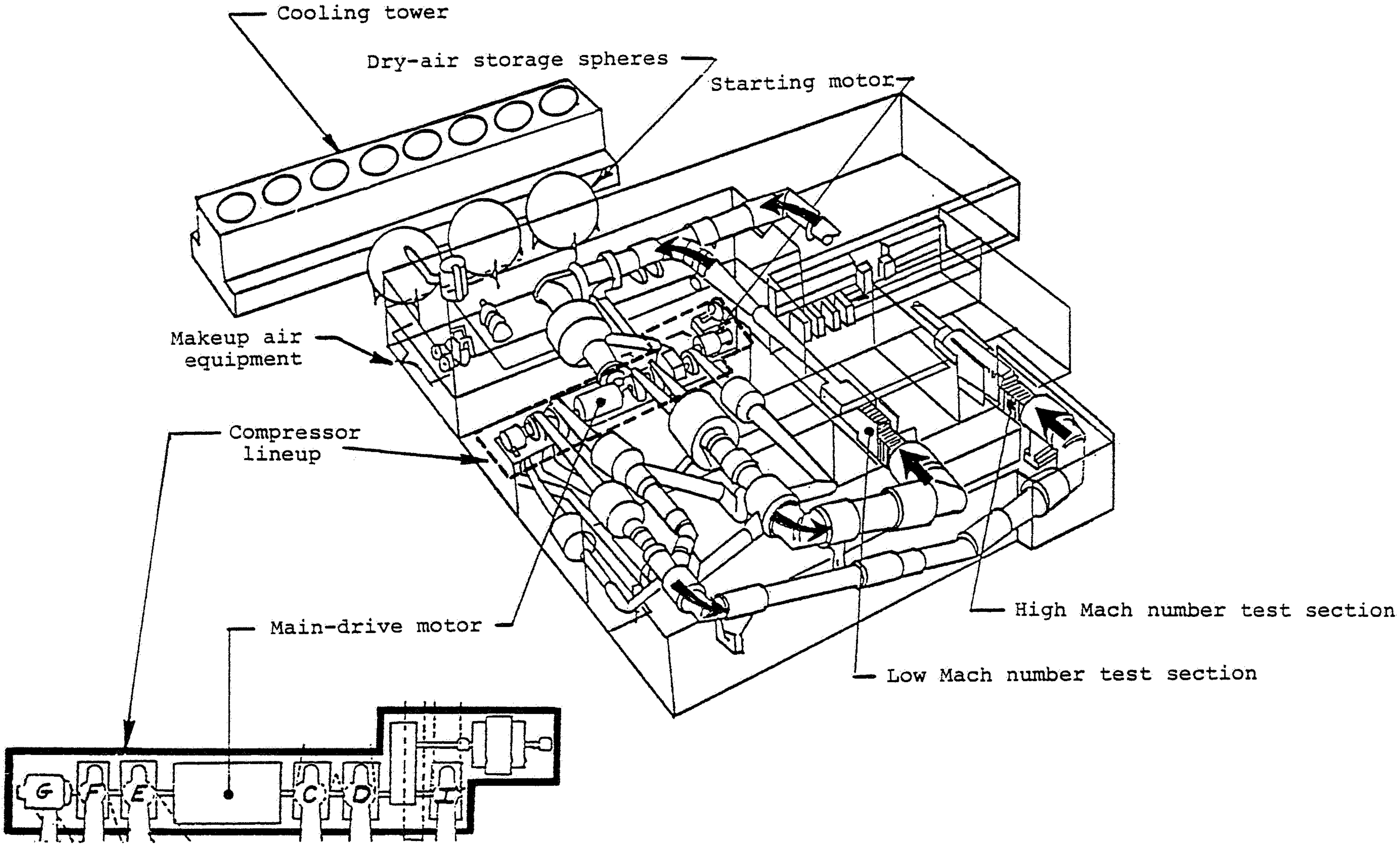

Figure 3.1. Schematic Drawing of the Langley Unitary Plan Wind Tunnel (UPWT).

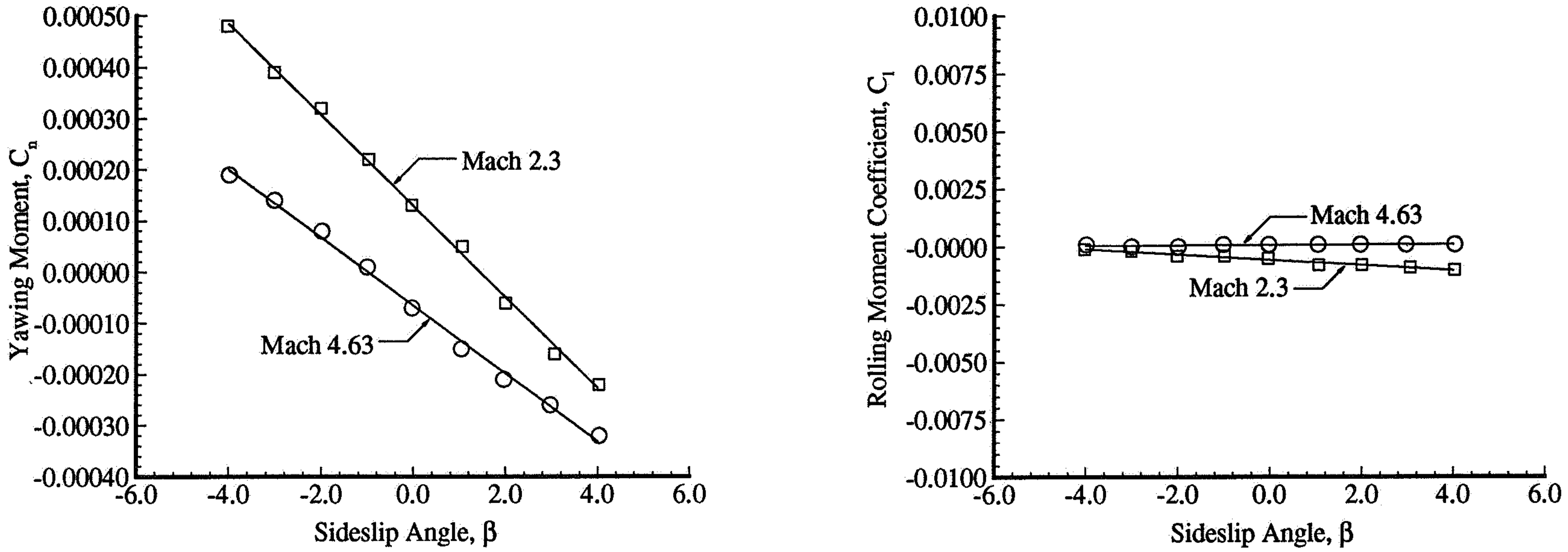

Figure 3.2. Yawing Moment Coefficient and Rolling Moment Coefficient Vs. Sideslip Angle for Beta Sweeps at Mach 2.3 and Mach 4.63 at 0^o Angle of Attack.

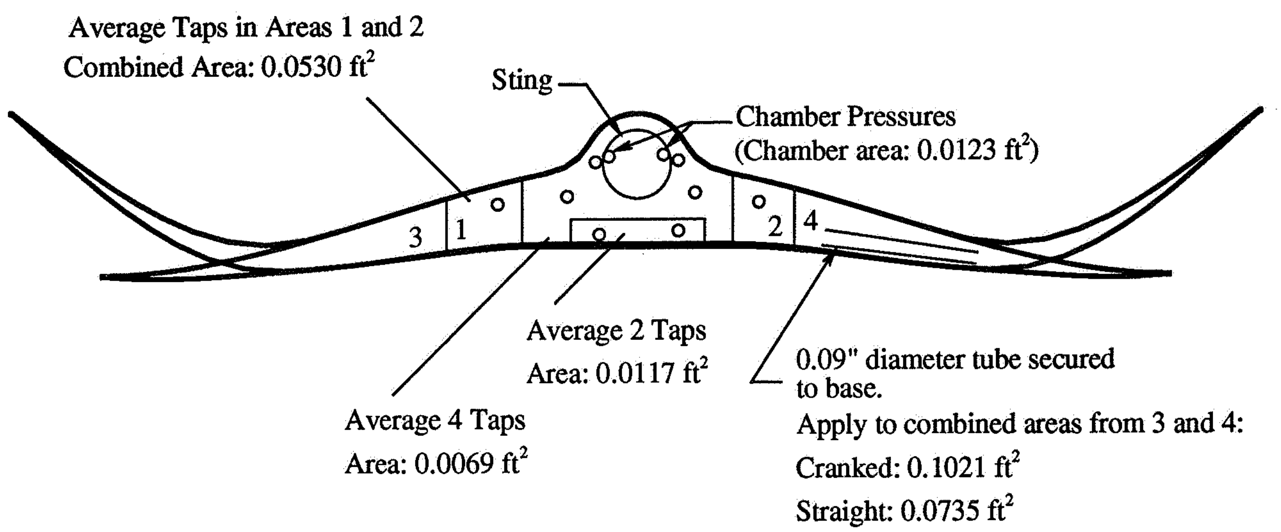

Figure 3.3(a). Placement of Base and Chamber Pressure Tubes on Configurations with No Engines or Control Surfaces.

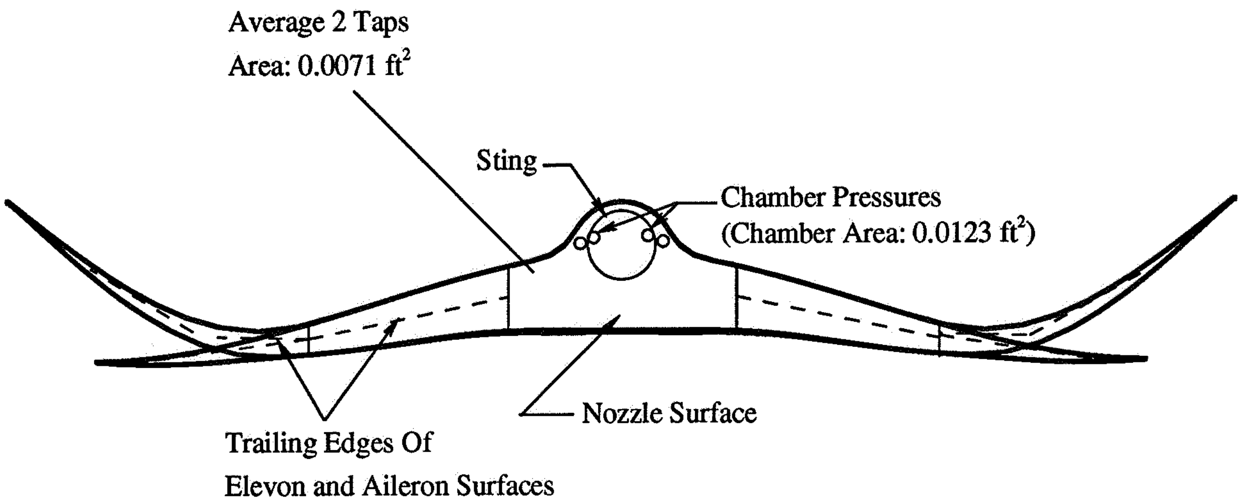

Figure 3.3(b). Placement of Base and Chamber Pressure Tubes on Configurations with Engines and Control Surfaces.

Tap No.	Model Sta.	B.L.	W.L.
1	22.030	-1.353	-1.785
2	22.030	-1.015	-1.788
3	22.030	-0.676	-1.792
4	22.030	-0.338	-1.796
5	22.791	-1.353	-1.244
6	22.791	-1.015	-1.252
7	22.791	-0.676	-1.254
8	22.791	-0.338	-1.255
9	23.552	-1.353	-0.964
10	23.552	-1.015	-0.974
11	23.552	-0.676	-0.974
12	23.552	-0.338	-0.975

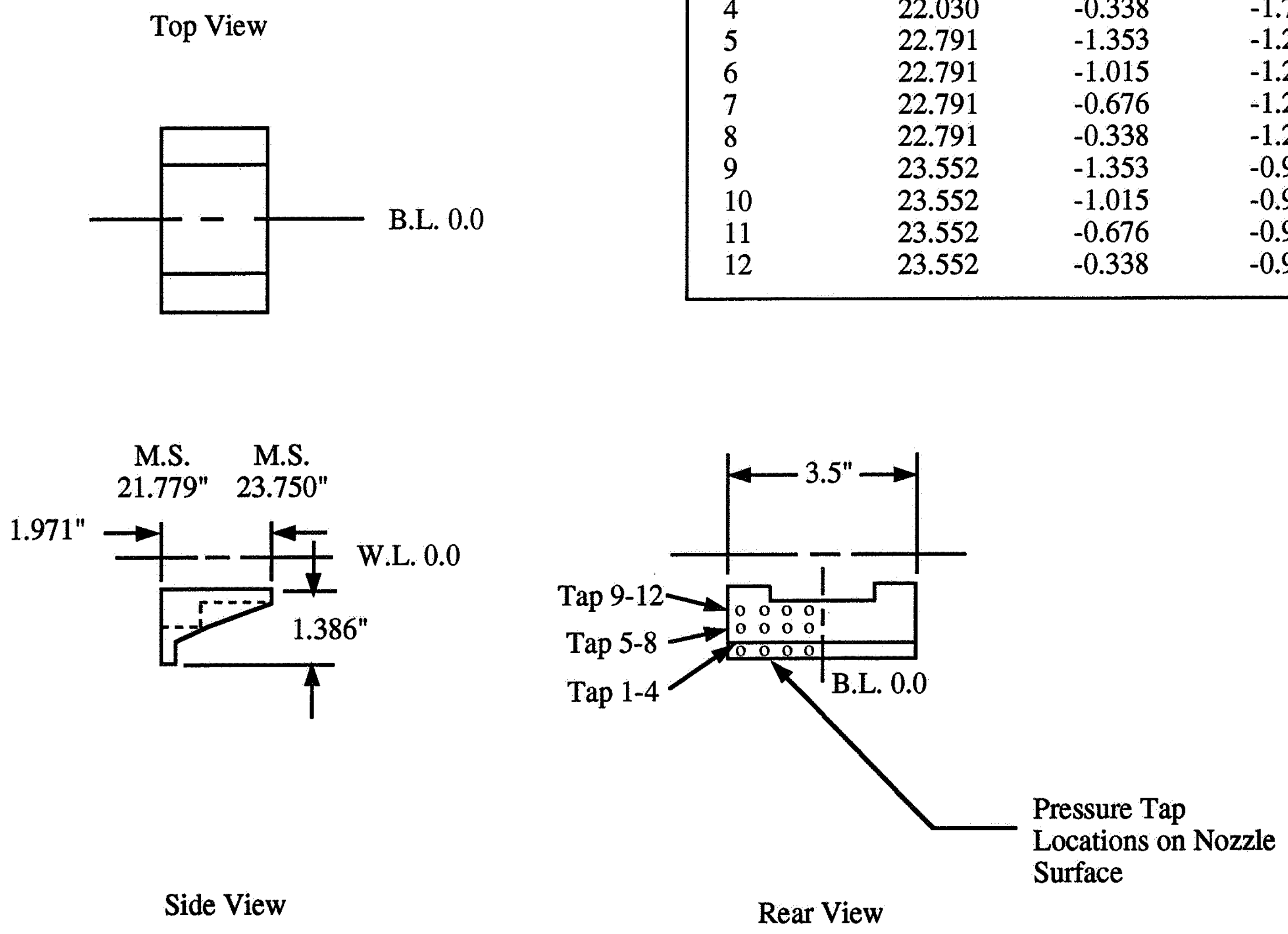

Figure 3.4(a). Three-View Drawing of Short Expansion Ramp Showing Pressure Tap Locations.

Tap No.	Model Sta.	B.L.	W.L.
13	24.313	-1.353	-0.724
14	24.313	-1.015	-0.731
15	24.313	-0.676	-0.734
16	24.313	-0.338	-0.745
17	25.075	-1.353	-0.516
18	25.075	-1.015	-0.523
19	25.075	-0.676	-0.532
20	25.075	-0.338	-0.739
21	25.836	-1.353	-0.332
22	25.836	-1.015	-0.339
23	25.836	-0.676	-0.451
24	25.836	-0.338	-0.739

Locations for Taps 1-12 are given in Figure 3.4(a).

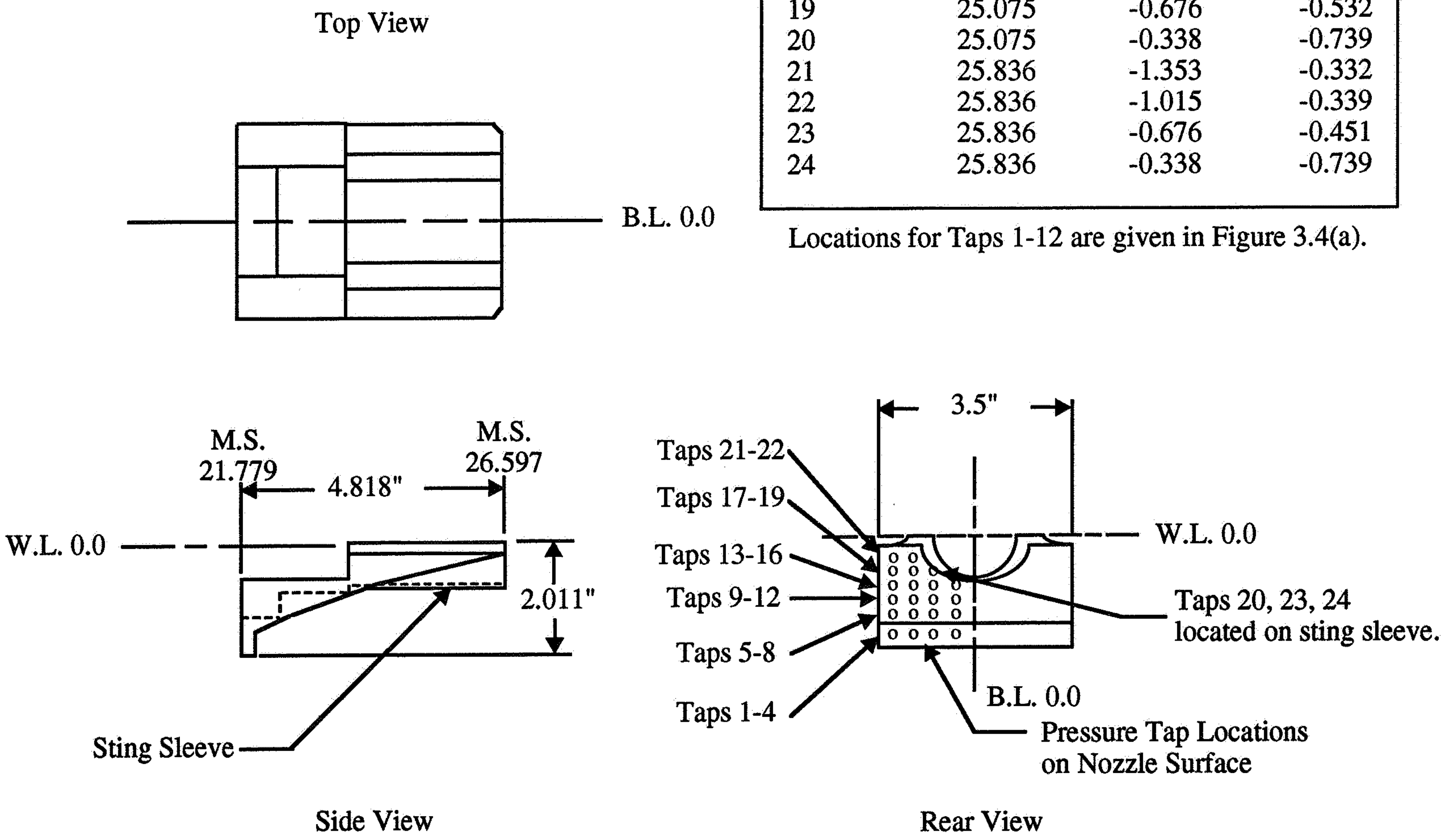

Figure 3.4(b). Three-View Drawing of Long Expansion Ramp Showing Pressure Tap Locations.

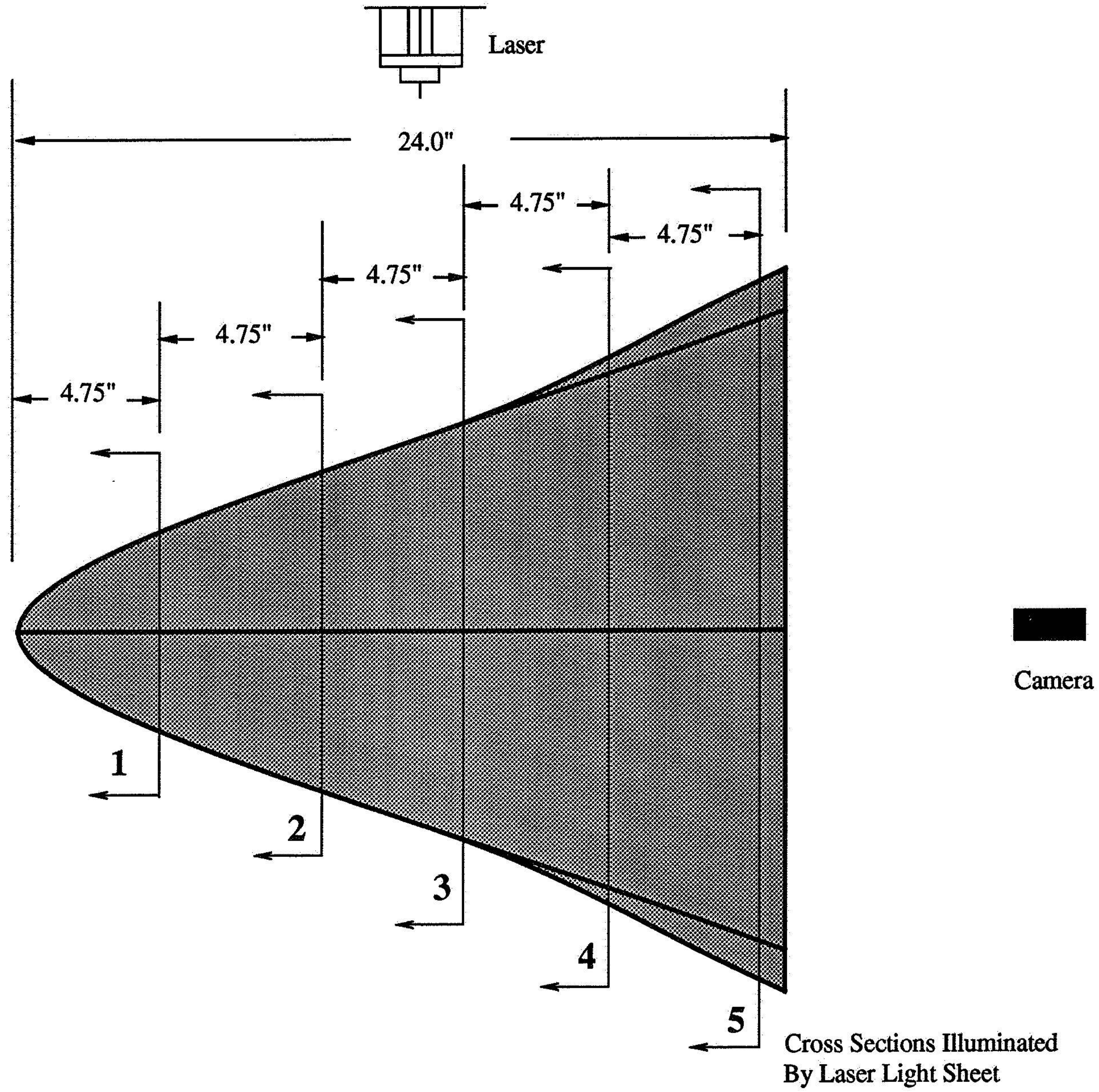

Figure 3.5. Laser Light Sheet Locations for Vapor Screen Runs.

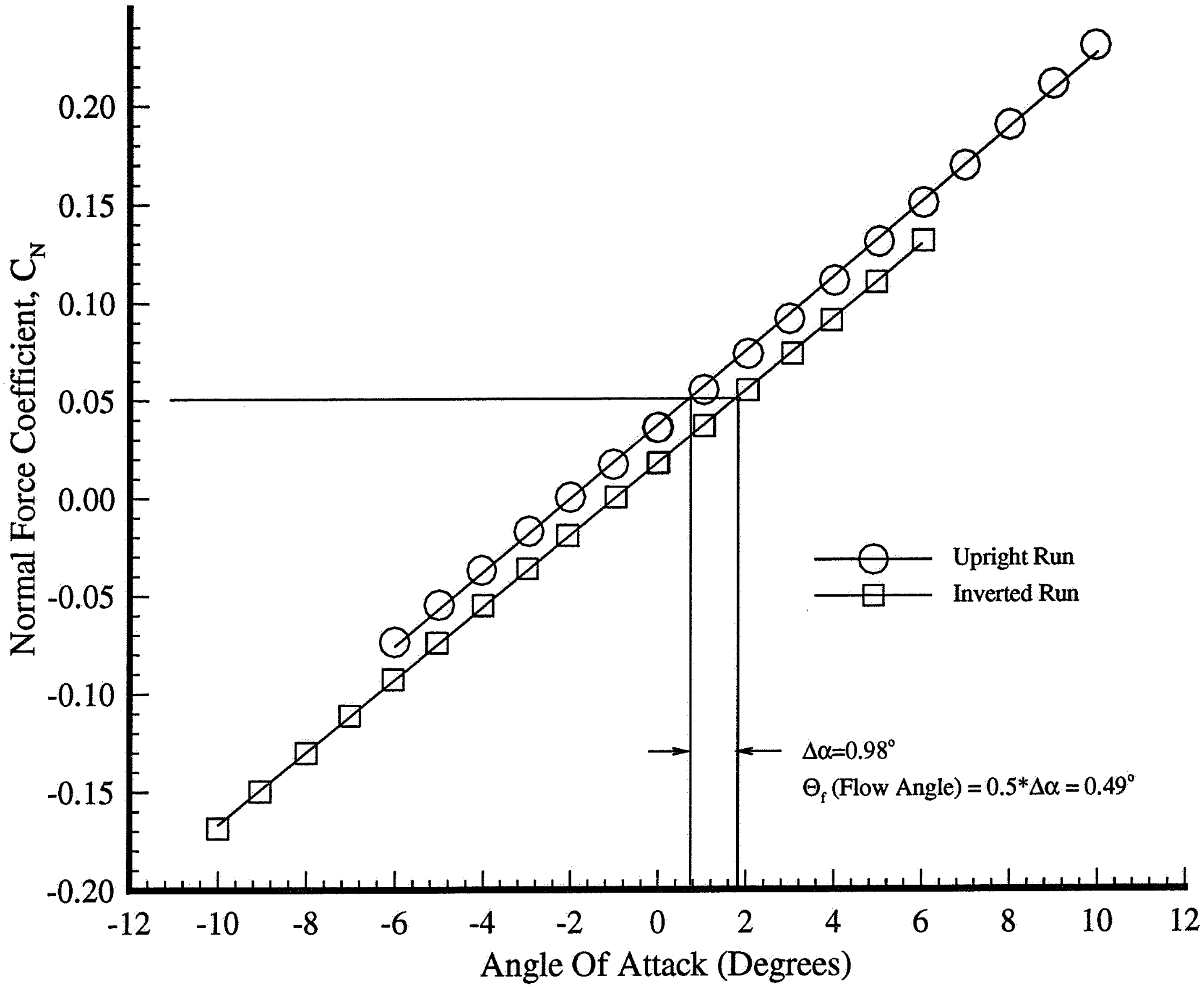

Figure 3.6. Computation of Test Section Flow Angle at Mach 4.63.

CHAPTER 4
COMPUTATIONAL METHODS

4.0 Summary

Computational Fluid Dynamics (CFD) solutions were obtained for the straight-wing design-code waverider shape and the "pure" straight-wing and cranked-wing models. The design-code shape refers to the waverider shape generated by the design code before the modifications discussed in section 2.4 were made. The "pure" waverider models refer to those configurations without engine components or control surfaces and with the smooth, ogive canopy attached. Solutions for these configurations were obtained in order to provide comparisons between the flow-field characteristics of the design-code shape and the fabricated model shape, between force coefficient and flow-field predictions from CFD solutions and experimental data for the pure waverider shapes, and between computational predictions and MAXWARP design-code predictions. The surface definition for the straight-wing design-code waverider was taken from the design code output and surface descriptions of the wind tunnel models were developed from computer-aided design (CAD) files of the model parts. Three-dimensional structured volume grids were created for each configuration and viscous CFD solutions were obtained using the General Aerodynamic Simulation Program (GASP).[16,17,19] Solutions were obtained at selected angles of attack at the design Mach number of 4.0 and at selected off-design Mach numbers at 0° angle of attack.

4.1 Computational Grids

Computational grids were developed for each configuration studied by first developing a numerical surface description and then creating 3D volume grids. The surface coordinates output by MAXWARP were used as the numerical description for the design-code shape. Since the code produces shapes which have infinitely sharp leading edges, the leading edges were rounded in order to provide a better comparison with the predictions for the wind-tunnel models. Numerical surface descriptions of the straight-wing and cranked-wing wind-tunnel models were obtained from CAD surface descriptions of the model parts. Three-dimensional volume grids were created for each configuration using the GRIDGEN software package, which utilizes algebraic transfinite interpolation methods with elliptic interior point refinement.[14]

The computational grids for each of the three configurations model only half of the configuration since each is symmetric about the center line. The ξ-computational direction runs from the nose of the configuration to the base of the configuration in the streamwise direction. The η-computational direction begins at the upper center line and wraps around the leading edge, ending at the lower center line. The ζ-computational direction runs from the surface of the configuration to the outer boundary. The computational and cartesian coordinate systems are shown in figure 4.1. The grid for the straight-wing design code waverider shape contained 51 points in the ξ direction, 79 points in the η direction and 61 points in the ζ direction. The grids for each of the two model shapes contained 91 points in the ξ direction, 111 points in the η direction and 91 points in the ζ direction. Additional points were necessary for these two grids in order to model the canopy, upper surface curvature and lower surface expansion. Blunt leading edges were modeled for each configuration. A close-up view of the base of the straight-wing model is shown in figure 4.2 in order to illustrate how this region is resolved. Grid points were also clustered near the surface of each configuration in order to adequately resolve the boundary layer flow. The amount of grid spacing needed is judged by examining the grid spacing parameter, y^+, which is given by[15]

$$y^+ = \sqrt{\frac{\rho_c u_c \Delta\zeta}{\mu_c}} \tag{4.1}$$

where ρ_c, u_c, and μ_c are the density, velocity and viscosity at the first cell center next to the solid surface and $\Delta\zeta$ is the distance from the first cell center to the body surface. Previous research has shown that y^+ values on the order of 1 provide accurate solutions.[15]

4.2 Solution Method

The CFD solutions were obtained using the General Aerodynamic Simulation

Program (GASP), version 2.2.[16,17] GASP is a finite volume code based on the upwind/relaxation algorithms. The code is capable of solving the full Reynolds-averaged Navier-Stokes (RANS) equations as well as subsets of these equations, including the parabolized Navier-Stokes (PNS), thin-layer Navier-Stokes (TLNS) and Euler equations. Time integration in GASP is based on the integration of primitive variables, and convergence to a steady state solution is obtained by iterating in pseudo-time until the L2 norm of the residual vector has been reduced by a sufficient amount. GASP also contains several flux-split algorithms and limiters to accelerate convergence to steady state. Mesh sequencing is also available as a means to improve convergence.

The computational method used in this study is to model each configuration as a two zone problem, as illustrated in figure 4.1. The first zone includes the blunt nose of the configuration. The flow in this region is a combination of subsonic and supersonic flow since there will be a small area of subsonic flow behind the detached bow shock. Therefore, the TLNS equations are solved over the entire zone using a global iteration procedure. The TLNS equations are obtained by neglecting all viscous terms parallel to the body surface. Only the viscous terms normal to the solid boundary are retained. The TLNS equations may be written in Cartesian coordinates as follows:[18]

$$\frac{\partial}{\partial t}\rho + \frac{\partial}{\partial x}(\rho u) + \frac{\partial}{\partial y}(\rho v) + \frac{\partial}{\partial z}(\rho w) = 0 \tag{4.1}$$

$$\frac{\partial}{\partial t}(\rho u) + \frac{\partial}{\partial x}(p + \rho u^2) + \frac{\partial}{\partial y}\left(\rho uv - \mu\frac{\partial u}{\partial y}\right) + \frac{\partial}{\partial x}(\rho uw) = 0 \tag{4.2}$$

$$\frac{\partial}{\partial t}(\rho v) + \frac{\partial}{\partial x}(\rho uv) + \frac{\partial}{\partial y}\left(p + \rho v^2 - \frac{4}{3}\mu\frac{\partial v}{\partial y}\right) + \frac{\partial}{\partial z}(\rho vw) = 0 \tag{4.3}$$

$$\frac{\partial}{\partial t}(\rho w) + \frac{\partial}{\partial x}(\rho uw) + \frac{\partial}{\partial y}\left(\rho uw - \mu\frac{\partial w}{\partial y}\right) + \frac{\partial}{\partial z}(p + \rho w^2) = 0 \tag{4.4}$$

$$\frac{\partial}{\partial t}(E_t) + \frac{\partial}{\partial x}(E_t u + pu) + \frac{\partial}{\partial y}(E_t v + \rho v - \mu u\frac{\partial u}{\partial y} - \frac{4}{3}\mu v\frac{\partial v}{\partial y} - \mu w\frac{\partial w}{\partial y} - k\frac{\partial T}{\partial y})$$

$$+ \frac{\partial}{\partial z}(E_t w + pw) = 0 \qquad (4.5)$$

In the preceding equations, E_t represents the total energy, ρ is the density, u, v, and w are velocity components, p is the pressure and μ is the viscosity coefficient. Furthermore, these equations assume that the y-direction is normal to the solid surface. Equation (4.1) is the continuity equation, equations (4.2) through (4.4) are the x, y, and z momentum equations and equation (4.5) is the energy equation. The second zone is the remainder of the configuration, extending from the zonal boundary to the base of the configuration. The flow in this region is solved by applying the PNS equations. The PNS equations are obtained by neglecting the streamwise viscous terms and are valid for predominately supersonic flows with no streamwise boundary layer separation. The PNS equations may be written in Cartesian coordinates as follows:[18]

$$\frac{\partial}{\partial x}(\rho u) + \frac{\partial}{\partial y}(\rho v) + \frac{\partial}{\partial z}(\rho w) = 0 \qquad (4.6)$$

$$\rho u\frac{\partial u}{\partial x} + \rho v\frac{\partial u}{\partial y} + \rho w\frac{\partial u}{\partial z} = -\frac{\partial p}{\partial x} + \frac{\partial}{\partial y}(\mu\frac{\partial u}{\partial y}) + \frac{\partial}{\partial z}(\mu\frac{\partial u}{\partial z}) \qquad (4.7)$$

$$\rho u\frac{\partial v}{\partial x} + \rho v\frac{\partial v}{\partial y} + \rho w\frac{\partial v}{\partial z} = -\frac{\partial p}{\partial y}$$

$$+ \frac{4}{3}\frac{\partial}{\partial y}(\mu\frac{\partial v}{\partial y}) + \frac{\partial}{\partial z}(\mu\frac{\partial v}{\partial z}) + \frac{\partial}{\partial z}(\mu\frac{\partial w}{\partial y}) - \frac{2}{3}\frac{\partial}{\partial y}(\mu\frac{\partial w}{\partial z}) \qquad (4.8)$$

$$\rho u\frac{\partial w}{\partial x} + \rho v\frac{\partial w}{\partial y} + \rho w\frac{\partial w}{\partial z} = -\frac{\partial p}{\partial z}$$

$$+ \frac{4}{3}\frac{\partial}{\partial z}(\mu\frac{\partial w}{\partial z}) + \frac{\partial}{\partial y}(\mu\frac{\partial w}{\partial y}) + \frac{\partial}{\partial y}(\mu\frac{\partial v}{\partial z}) - \frac{2}{3}\frac{\partial}{\partial z}(\mu\frac{\partial v}{\partial y}) \qquad (4.9)$$

$$\rho u C_v \frac{\partial T}{\partial x} + \rho v C_v \frac{\partial T}{\partial y} + \rho w C_v \frac{\partial T}{\partial z} = -p\left(\frac{\partial u}{\partial x} + \frac{\partial v}{\partial y} + \frac{\partial w}{\partial z}\right) + \frac{\partial}{\partial y}\left(k\frac{\partial T}{\partial y}\right)$$

$$+ \frac{\partial}{\partial z}\left(k\frac{\partial T}{\partial z}\right) + \mu\left[\left(\frac{\partial u}{\partial y}\right)^2 + \left(\frac{\partial u}{\partial z}\right)^2 + \left(\frac{\partial w}{\partial y} + \frac{\partial v}{\partial z}\right)^2\right]$$

$$+ \frac{4}{3}\mu\left(\left(\frac{\partial v}{\partial y}\right)^2 + \left(\frac{\partial w}{\partial z}\right)^2 - \frac{\partial v \partial w}{\partial y \partial z}\right) \qquad (4.10)$$

In the preceding equations, T is the temperature, C_v is the specific heat at constant volume and the streamwise direction is assumed to be the x-direction. Equation (4.6) is the continuity equation, equations (4.7) through (4.9) are the momentum equations and equation (4.10) is the energy equation. The PNS equations allow the use of a space marching technique, whereby a single plane is fully converged before advancing to the next plane in the streamwise direction. This technique may be used since there is no downstream influence in supersonic flows. GASP also uses the Vigneron technique to correct for the presence of a streamwise pressure gradient in the subsonic region of the boundary layer when solving the PNS equations.[19] A no-slip boundary condition is applied to all solid boundaries with a fixed wall temperature of 585 °R. This temperature is identical to that specified in the MAXWARP optimization routine when designing the waverider shapes. Freestream conditions are applied at the outer boundary; second order extrapolation from interior cells is applied at the last streamwise plane and symmetry boundary conditions are applied at the center line. The Baldwin-Lomax algebraic turbulence model was used in these solutions to model turbulent boundary layers[17] and convergence to a steady state was obtained by reducing the L2 norm of the residual vector by 5 orders of magnitude.

4.3 Conditions

In order to make appropriate comparisons, the conditions at which solutions were obtained were chosen based on conditions at which experimental data were available. Solutions were obtained at Mach 4.0 at angles of attack of -6, 0, 2, 4 and 8 degrees for the design-code shape and the straight-wing model. Solutions were obtained at Mach 4.0 at angles of attack of -6, 0 and 8 degrees for the cranked-wing model. Solutions were also obtained at off-design Mach numbers of 2.3 and 4.63 at 0^o angle of attack for each of the three configurations. A summary of freestream properties for each condition run is shown in table 4.1. Flow-field characteristics and force coefficient predictions from computational solutions are presented in Chapter 5 along with experimental force, moment and flow visualization data for the pure waverider models.

Mach No.	Temperature, T (^oR)	Density, ρ (lbm/ft^3)	Pressure, P (lbf/ft^2)	Dynamic Pressure, q (lbf/ft^2)	Viscosity Coefficient, μ (lbm/[s-ft])
2.3	284.57	7.618×10^{-3}	115.39	427.21	7.237×10^{-6}
4.0	151.89	3.220×10^{-3}	25.977	290.95	3.882×10^{-6}
4.63	120.77	2.424×10^{-3}	15.340	233.19	3.016×10^{-6}

Note: All of the above conditions correspond to a freestream Reynolds number of 2.0×10^6 per foot.

Table 4.1. Freestream conditions used for computational solutions.

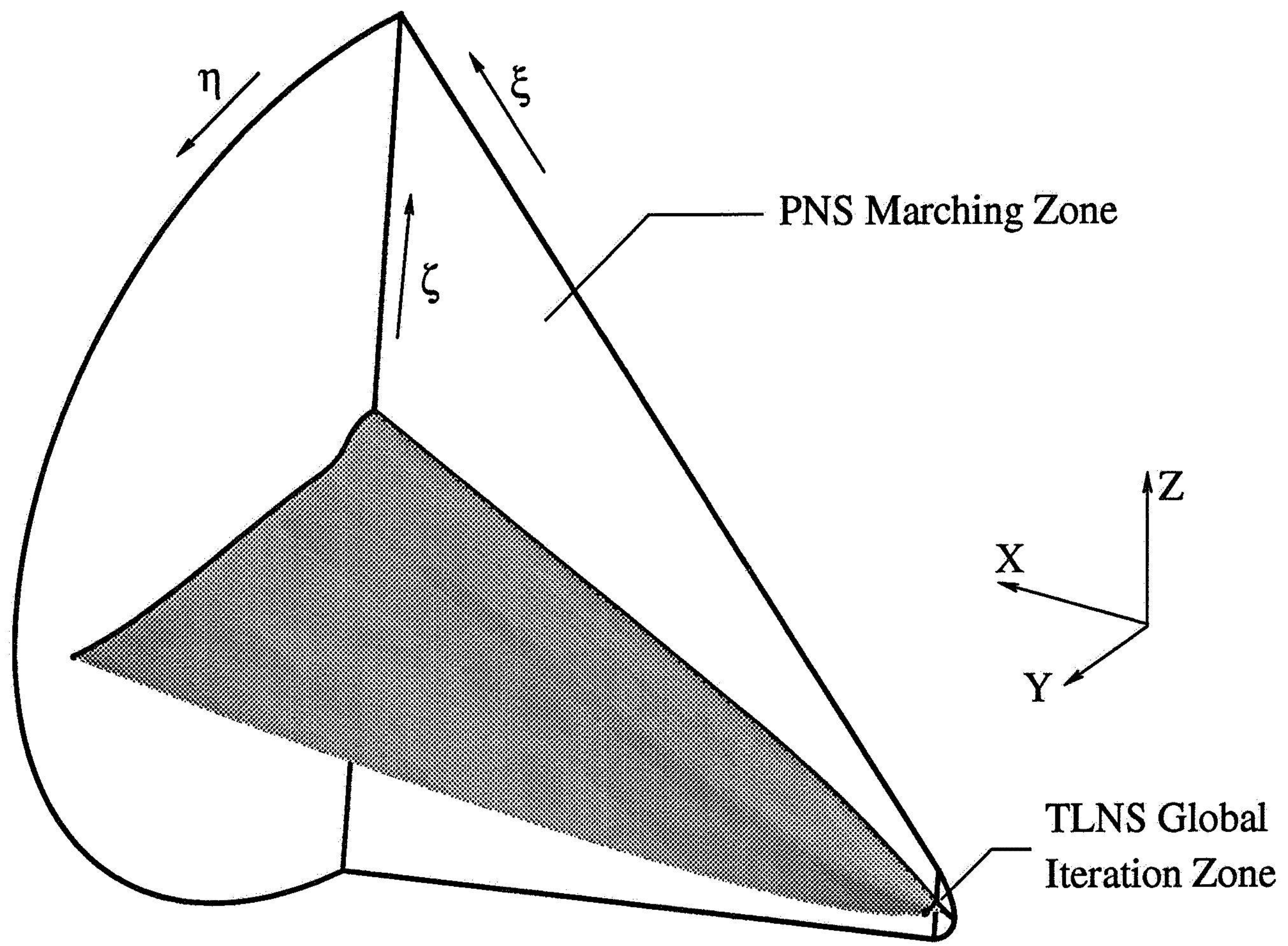

Figure 4.1. Coordinates and Computational Scheme for Waverider CFD Solutions.

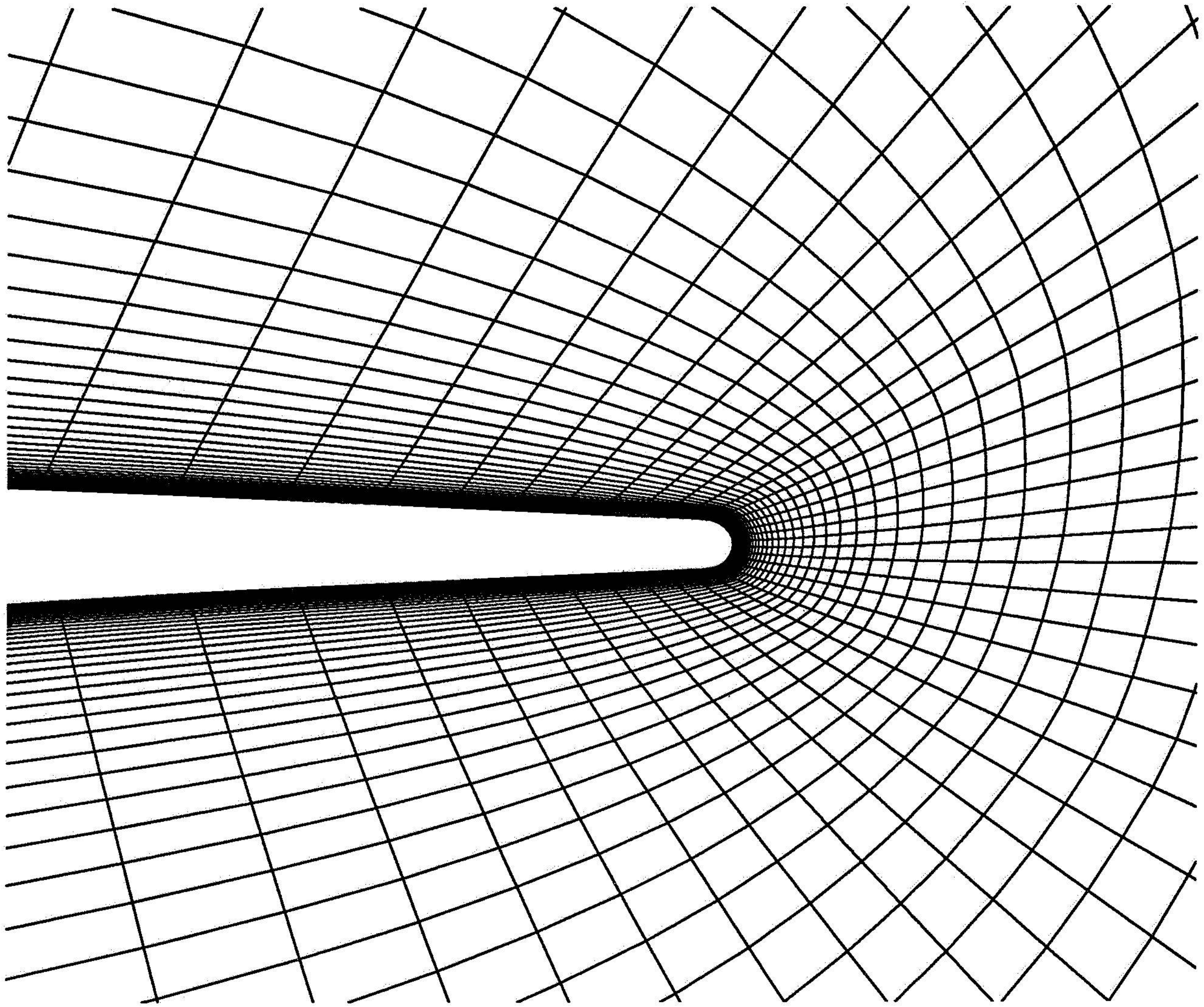

Figure 4.2. Close-Up View of Outer Leading Edge at Base of Straight-Wing Waverider Model.

CHAPTER 5
WAVERIDER FLOW-FIELD CHARACTERISTICS AND AERODYNAMIC PERFORMANCE

5.0 Summary

The flow-field characteristics and aerodynamic performance of the two pure waverider configurations, with no integrated components except the smooth canopy, are examined in this chapter. The differences between the flow-field characteristics of the straight-wing design-code shape and the straight-wing pure waverider model are illustrated by comparing computational fluid dynamics (CFD) solutions for each configuration. The flow-field characteristics of the straight-wing and cranked-wing pure waverider models are examined at the design Mach number by comparing CFD solutions with experimental flow-visualization data. Flow-field variations over an angle of attack range at Mach 4.0 and at off-design Mach numbers are also shown. The aerodynamic performance and stability characteristics of the two pure waverider models are examined using experimental force and moment data. Flow-field and force coefficient predictions from CFD solutions are also presented for comparisons where appropriate.

5.1 Flow-Field Characteristics at the Design Mach Number

The flow-field characteristics of waverider configurations at the design Mach number can be illustrated by examining computational solutions of each configuration as well as experimental flow visualization data. Differences between the flow fields of the straight-wing design-code shape and the straight-wing pure waverider model are examined first by comparing CFD solutions of each configuration at Mach 4.0. This comparison will show the effects of the modifications made to the design-code shape in order to obtain the model shape, as discussed in chapter 2. Figure 5.1 shows non-dimensional static pressure contours at the center line of each configuration for solutions at $M_\infty = 4.0$, $\alpha=0^o$ and $Re_\infty=2.0\text{x}10^6$ per foot. The static pressures are non-dimensionalized by freestream pressure. The presence of the canopy on the straight-wing model causes a compression on the upper surface. The top surface of the design-code shape is designed as a freestream surface. The straight-wing design code shape does show a slight compression on the upper surface, due to boundary layer displacement. The bottom-surface flow field of the straight-wing model is identical to that of the design-code shape up to the point where the expansion begins on the model surface. The presence of the expansion surface does not disrupt the smooth conical flow field on the bottom surface of the waverider model and does not degrade the waverider PAI characteristics. Figure 5.2 shows non-dimensional static pressure contours at the base of each configuration for the same two solutions. There is a large low pressure region in the bottom-surface flow field of the straight-wing model that extends from the center line to approximately half the distance to the outer leading edge. This is due to the expansion on the bottom surface of the model. The two additional flow-field features which can be seen in the solution of the straight-wing model are the bow shock above the upper surface and the edge of the expansion fan which originates at the point where the canopy blends with the upper surface. The high pressure region is confined below the bottom surface of both configurations and the shock is slightly detached from the leading edge. Figure 5.3 shows a close-up view of the outer leading edge of both configurations. Both views are shown to the same length scale. The leading edge of the model extends further out in the spanwise direction than the design-code shape because the procedure used to blunt the leading edges of the design-code shape was to shorten the leading edge, while the model shape was rounded by lengthening the leading edge. As a result, the detachment distance is smaller for the straight-wing model than for the design-code shape. This detachment distance exists at the design Mach number for both configurations due to blunt leading edge effects and boundary layer displacement effects.

The flow-field characteristics of the straight-wing and cranked-wing pure waverider models are illustrated by presenting CFD solutions for each configuration as well as laser vapor-screen photographs from the wind-tunnel tests. Figure 5.4 shows a laser vapor-screen photograph of the flow at the base of the straight-wing pure waverider model and non-dimensional static pressure contours at the base of the same configuration from a CFD solution at Mach 4.0, 0^o angle of attack and freestream Reynolds number of $2.0x10^6$ per foot. The photograph was taken using a camera mounted behind the model and looking upstream. The model lower surface is highlighted in the photograph by the laser light sheet on the surface. The bow shock is indicated by the contrast between light and dark regions below the light sheet. On the left-hand side of the photograph, the shock is observed to be meeting the edge of the lower surface. Thus, the vapor-screen photograph confirms the shock attachment characteristics predicted by the CFD solution. The experimental data and CFD predictions also indicate that the high pressure region remains confined below the model lower surface. The same type of data are shown in figure 5.5 for the cranked-wing pure waverider model. The shock can be seen in the right-hand side of the photograph meeting the outer leading edge of the model. The lower surface is again highlighted by the laser light. The experimental data confirm the shock attachment characteristic at the outer leading edge, which is predicted by the CFD solution for this case as well. Figure 5.6 further illustrates that the shock is slightly detached at the outer leading edge for both models. This figure shows a close-up view of the outer leading edge at the base of the cranked-wing and straight-wing configurations from CFD solutions at Mach 4.0 and 0^{o} angle of attack. Both of the views in the figure are to the same length scale and non-dimensional static pressure contours are shown in each view.

5.2 Off-Design Angle of Attack and Mach Number Effects on Flow-Field Characteristics

The flow-field characteristics at off-design angles of attack may be examined by comparing laser vapor-screen photographs with computational solutions. Figure 5.7 shows a vapor-screen photograph of the cranked-wing pure waverider model taken at Mach 4.0 and -6^{o} angle of attack. The photograph was again taken using a camera mounted behind the model and looking upstream and the upper surface is highlighted by the laser light. Also shown on the figure is a CFD solution for the same configuration at the same freestream conditions and angle of attack. Static pressure contours, non-dimensionalized by freestream pressure, are shown at the base of the configuration in the figure. The CFD solution indicates that the shock is detached from the leading edge. The detachment distance is slightly greater than at the zero degree angle of attack condition. A large high pressure region exists on the outer portion of the wing upper surface. This is due to a compression on the outer wing tips where the leading edges begin to turn upward. The shape of the shock in the upper surface flow field is qualitatively confirmed by the vapor-screen photograph. Figure 5.8 shows a vapor-screen photograph and CFD solution of the same configuration at Mach 4.0 and 8^{o} angle of attack. The CFD solution again shows that the shock is detached from the outer leading edge at this angle of attack, but no significant amount of flow spillage occurs at the leading edge. The high pressure region is still mostly confined to the lower surface. A large low pressure region is present near the outer wing tips on the upper surface. The qualitative shock shape is confirmed by the vapor screen photograph. Figure 5.9 shows a comparison of CFD solutions of the straight-wing configuration at Mach 4.0 and angles of attack of -6^{o} and 8^{o}. Vapor-screen photographs were not available for this configuration at these conditions, due to the poor quality of the photographs taken during the experiment. Similar patterns are seen in the flow field of the straight-wing configuration as those that were observed for the cranked-wing model. The shock is detached from the outer leading edge at both conditions, but no significant amount of flow spillage occurs. The detachment distances are greater than for the cranked-wing configurations.

The flow-field characteristics of each configuration at off-design Mach numbers can also be illustrated by examining experimental flow visualization data and CFD solutions. Figure 5.10 shows a comparison of a vapor-screen photograph and a CFD solution for the cranked-wing model at Mach 2.3 and 0^{o} angle of attack. The freestream Reynolds number is $2.0\text{x}10^{6}$ per foot. The orientation and data shown in this figure are the same as the previous figures. At Mach numbers below the design Mach number of 4.0, the shock wave angle is larger and the detachment distance should be much larger than at the design Mach number. This is confirmed in the CFD solution as well as the experimental data. There is a small amount of flow spillage from the lower surface to the upper surface, as evidenced by the high pressure values at the outer wing tip on the upper surface. Figure 5.11 shows similar views of the same configuration at Mach 4.63. The photograph in this figure was taken with the laser light sheet approximately 5 inches upstream of the base, since the quality of the photograph taken with the light sheet at the base was poor. Above the design Mach number, the shock moves closer to the leading edge than at the design Mach number, as illustrated in both the vapor-screen photograph and predicted by the CFD solution.

There is still a large high pressure region in the bottom-surface flow field of this configuration. CFD flow-field predictions for the straight-wing configuration are shown in figure 5.12. The computational solutions for the straight-wing model predict similar shock detachment/attachment characteristics as the cranked-wing model at Mach 2.3 and Mach 4.63. The shock attachment characteristics can be further illustrated by examining planform schlieren photographs of the cranked-wing model. Figure 5.13 shows schlieren photographs of the cranked-wing model at Mach 2.3 (top), Mach 4.0 (middle) and Mach 4.63 (bottom). The right of the figure shows a close-up view near the leading edge at each Mach number. The schlieren images in this figure have been enhanced by computer imaging techniques in order to show the shock structure more clearly. At Mach 2.3, the schlieren photograph shows that the shock is detached from the leading edge. At Mach 4.0, the shock is much closer to the outer leading edge, but a small detachment distance still exists. At Mach 4.63, the photograph does not show the presence of a shock wave near the leading edge, possibly because the shock is attached at this condition.

5.3 Aerodynamic Performance and Stability of Baseline Waverider Configurations

The aerodynamic performance and stability characteristics are examined using experimental force and moment data and computational predictions. The performance of the straight-wing design-code shape and the straight-wing pure waverider model are examined first using CFD predictions for force coefficients in order to the show the effects of the modifications made to the design-code waverider shape. Then, the aerodynamic performance of the two pure waverider models are examined using experimental data and compared with CFD predictions. Off-design Mach number and Reynolds number effects are also evaluated. Finally, the longitudinal and lateral-directional stability characteristics are examined for each configuration using experimental data. All of the experimental and computational data presented assumes that freesteam pressure acts at the blunt base of the configurations, as discussed in section 3.3, and the reference moment center used is 16.623 inches aft of the nose for each configuration.

The aerodynamic performance characteristics of the straight-wing design-code shape and the straight-wing pure waverider model are examined in order to show the effects of the modifications made to the design-code shape. Figure 5.14 shows lift and drag coefficients as well as lift-to-drag ratios of both configurations at $M_\infty = 4.0$ and Re_∞=2.0x10^6 per foot. The data presented here are developed by integrated pressure and skin friction values from CFD solutions. Therefore, the predictions shown include both inviscid and viscous forces. Also shown in the figure are the design-code predictions for each quantity. The lift coefficient value for the design-code shape at 0^o angle of attack is greater than that for the model. This is due to a loss of lift from the lower surface expansion of the model. As angle of attack increases, this difference diminishes. The values obtained from CFD predictions for the design-code shape are lower than the design code predictions. At lower values of lift coefficient, the drag values for the model are higher than that of the design-code shape, due to increased drag from the additional volume on the upper surface. However, at higher values of lift coefficient, the design-code shape shows higher drag values. The drag values obtained from CFD predictions are slightly higher than the design-code predictions. The design-code shape has a higher maximum lift-to-drag ratio and it occurs at a lower lift coefficient value than the model. At higher values of lift coefficient, the model shows higher lift-to-drag ratios. These comparisons of the performance characteristics of the two configurations indicate that the modifications made to the design-code shape to develop the wind-tunnel model did not cause a significant degradation in the waverider aerodynamic performance.

The aerodynamic performance of the straight and cranked pure waverider configurations at the design Mach number is shown in figure 5.15. This figure shows experimental data and CFD predictions for the lift, drag and lift-to-drag ratios of each configuration at Mach 4.0 and a Reynolds number of 2.0x10^6 per foot. In general, there is good agreement between the experimental data and computational predictions. The experimental data show that the cranked-wing configuration has a slightly higher maximum lift-to-drag ratio than the straight-wing model. The experimental data also show that the maximum lift-to-drag ratio occurs near 2^o angle of attack for each configuration. The design code assumes a waverider at 0^o angle of attack as the design condition. This finding is consistent with previous studies, such as those in references 3 and 5, which show that the maximum lift-to-drag occurs at an angle of attack greater than 0^o for the configurations studied. At positive angles of attack, the straight-wing model shows higher values of lift coefficient than the cranked-wing model, because some of the pressure on the lower surface of the cranked wing-tips is accounted for as a component of side force. The cranked-wing model has lower drag values because it has a larger base area, and the assumption of freestream pressure at the base reduces the total drag of the configuration more than it does for the straight-wing configuration.

The off-design performance of the straight-wing and cranked-wing pure waverider models is shown in figures 5.16 and 5.17, respectively. Each of these figures shows the experimental lift, drag and maximum lift-to-drag ratio at all Mach numbers studied as well as maximum lift-to-drag ratio versus Mach number. The data indicate that there is no significant performance degradation at off-design Mach numbers. Both configurations show higher maximum lift-to-drag ratios than the design point value at Mach numbers less than 4.0. This is not inconsistent with waverider methodology, since a waverider optimized for Mach 2.3 would have even better performance at Mach 2.3 than the Mach 4.0 configuration has here. Similar results have been found in previous studies.[3,4,5] The cranked-wing configuration has slightly better aerodynamic performance across the Mach number range than the straight-wing configuration.

The effects of Reynolds number on aerodynamic performance of the straight-wing and cranked-wing configurations are shown in figures 5.18 and 5.19, respectively. There are no significant effects of Reynolds number variation for either configuration in the range studied, except for a slight increase in maximum lift-to-drag ratio at the 3.0×10^6 per foot condition for both configurations. This is possibly due to the fact that boundary layer displacement thickness varies inversely with Reynolds number, so the shock detachment distance caused by boundary layer displacement may be somewhat smaller at higher Reynolds numbers. The smaller detachment distance could lead to less flow spillage and thus, lower drag values. An alternative explanation is that according to equation (2.2), the skin friction coefficient decreases as Reynolds number increases, resulting in decreased drag and thus increased lift-to-drag ratios at higher Reynolds numbers. This effect is likely the largest contributor to the decreased drag values observed since the decrease in drag observed experimentally is approximately equal to the decrease in viscous drag predicted by equation (2.2). Computational solutions at Mach 4.0 and a Reynolds number of 2.0×10^6 per foot show that the viscous drag contribution is approximately 34 percent of total drag.

The pitching moment characteristics of the straight-wing and cranked-wing pure waverider configurations are shown in figure 5.20. This figure shows the pitching moment coefficient versus angle of attack at each Mach number studied and the pitching moment slope versus Mach number for each configuration. Both configurations are unstable with respect to longitudinal motion at all Mach numbers, as evidenced by the positive pitching moment curve slope values. The yawing moment characteristics are shown in figure 5.21. This figure shows the yawing moment derivative versus angle of attack at each Mach number studied for both configurations. The straight-wing configuration is unstable with respect to directional motion at all Mach numbers studied, as evidenced by the negative values of yawing moment derivative. The cranked-wing configuration is stable with respect to directional motion at all Mach numbers studied at angles of attack above 4 degrees. Both configurations become more stable as Mach number decreases. The cranked-wing configuration is expected to provide enhanced directional stability from the increased dihedral angle at the outer leading edge. The rolling moment characteristics are shown in figure 5.22 for each configuration. The cranked-wing shows better lateral stability characteristics than the straight-wing model. The cranked-wing configuration is stable above 0^o angle of attack at all Mach numbers. The straight-wing model is unstable at angles of attack below 8.0^o at Mach 4.0 and Mach 4.63 and is unstable at angles of attack below 4^o at Mach 2.3.

Straight-Wing Design-Code Waverider Shape

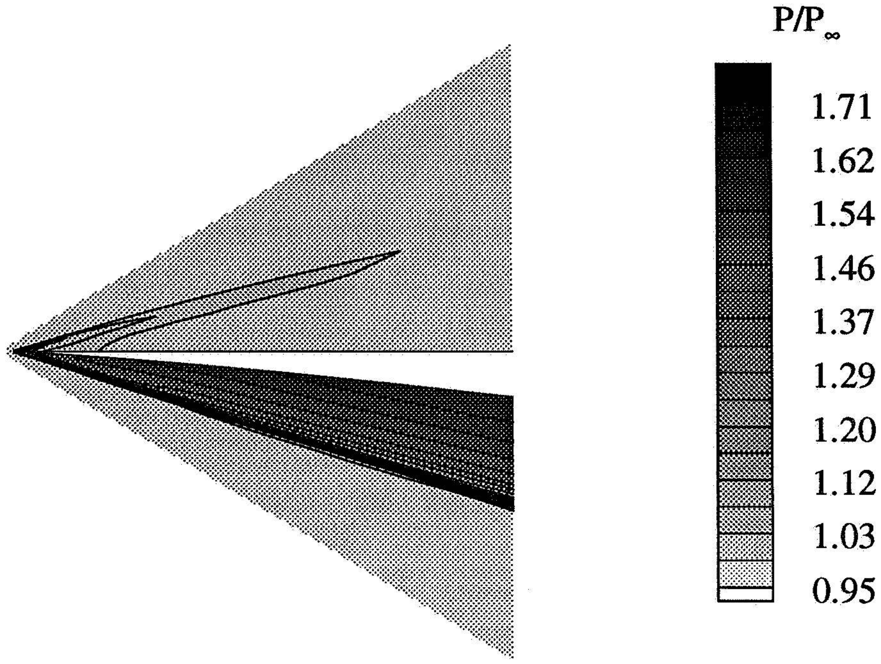

Straight-Wing Pure Waverider Model

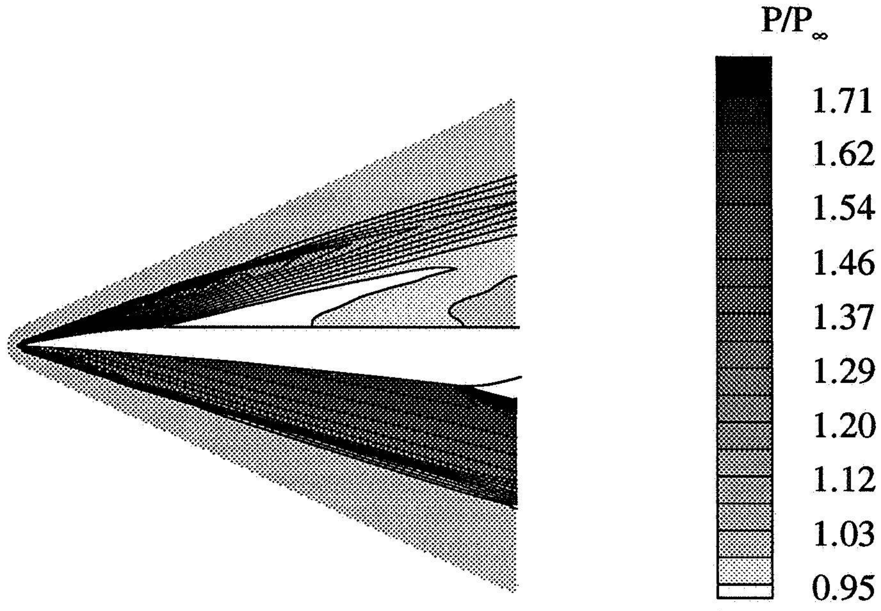

Figure 5.1. Nondimensionalized static pressure contours at the center line of the straight-wing design-code shape and model from CFD solutions at Mach 4.0, $\alpha=0^o$.

MAXWARP Straight-Wing Waverider Shape

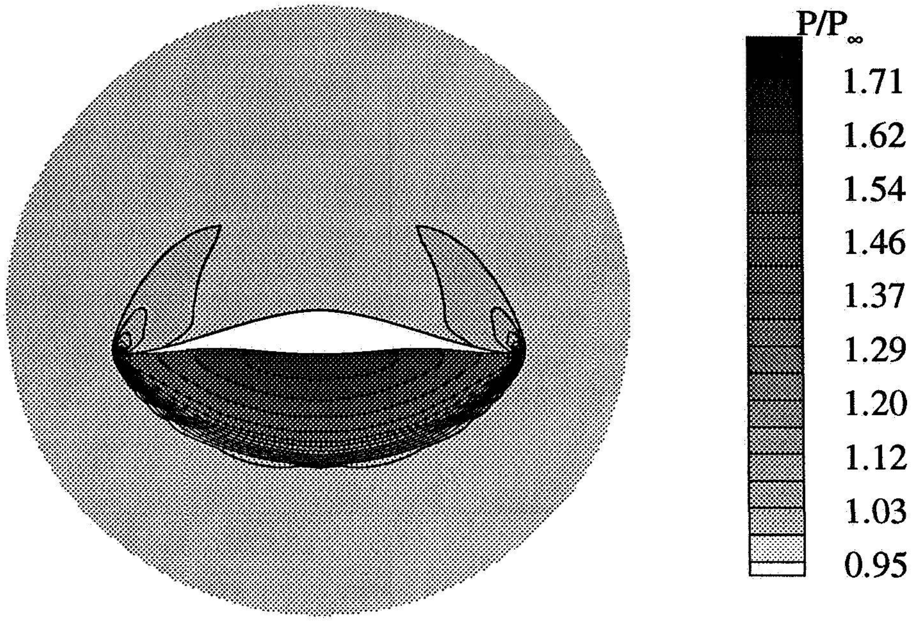

Straight-Wing Pure Waverider Model

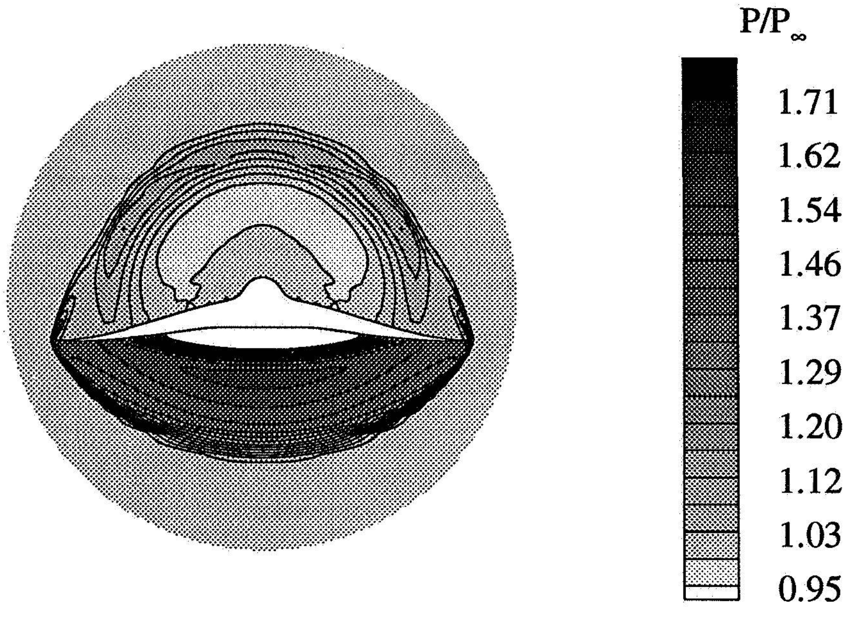

Figure 5.2. Nondimensionalized static pressure contours at the base of the straight-wing design-code shape and model from CFD solutions at Mach 4.0, $\alpha=0^{\circ}$.

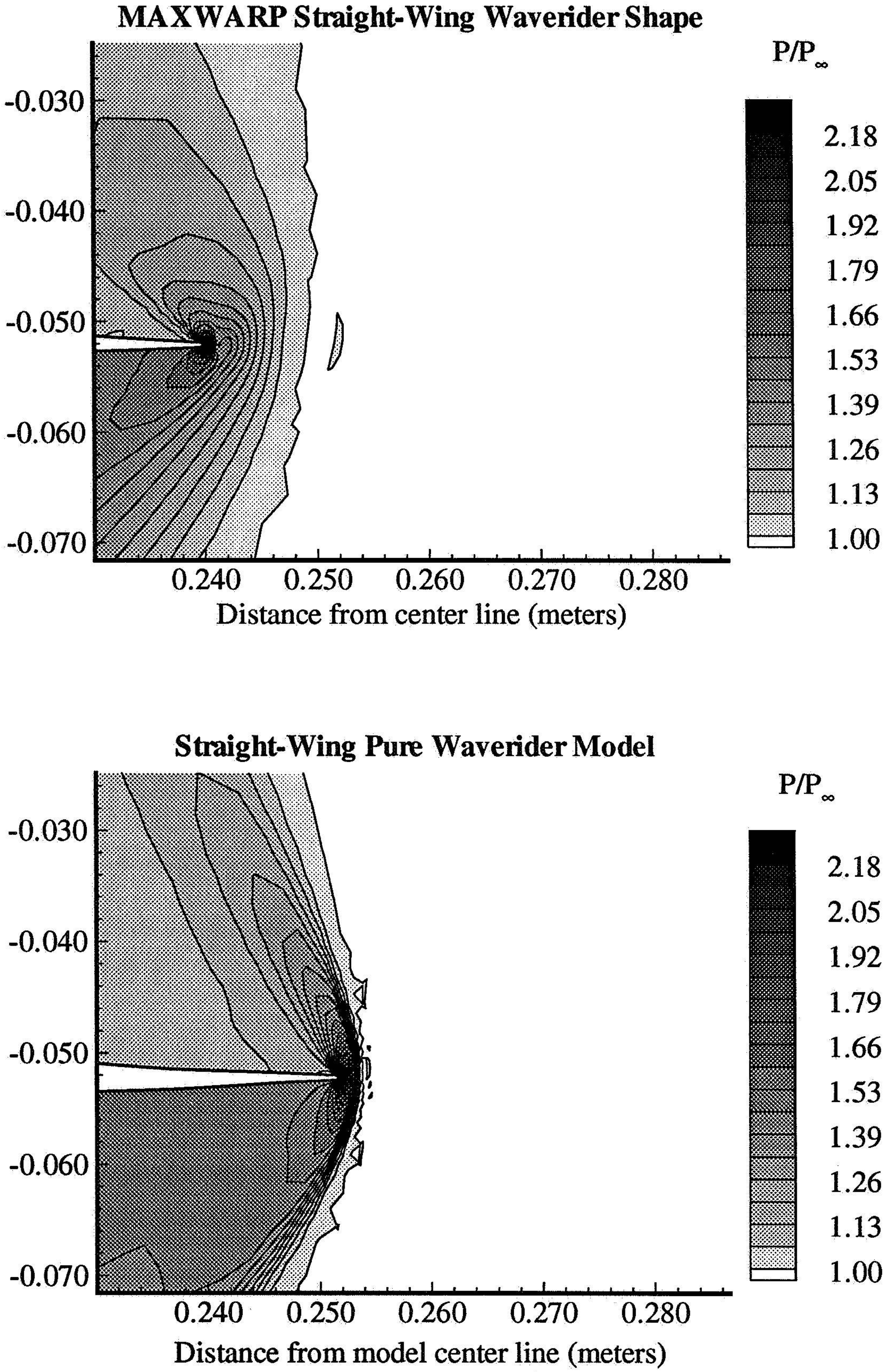

Figure 5.3. Nondimensionalized static pressure contours near the outer leading edge at the base of the straight-wing design-code and model shapes from CFD solutions at Mach 4.0, $\alpha=0^{\circ}$.

Vapor-Screen Photograph of Base

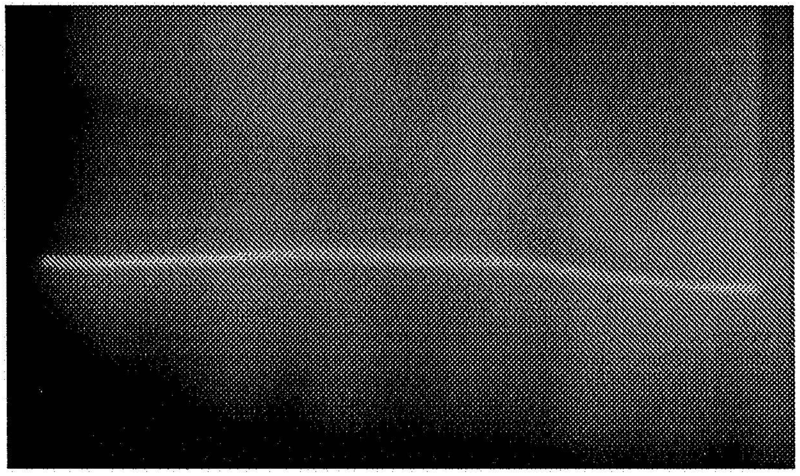

Base View of CFD Solution

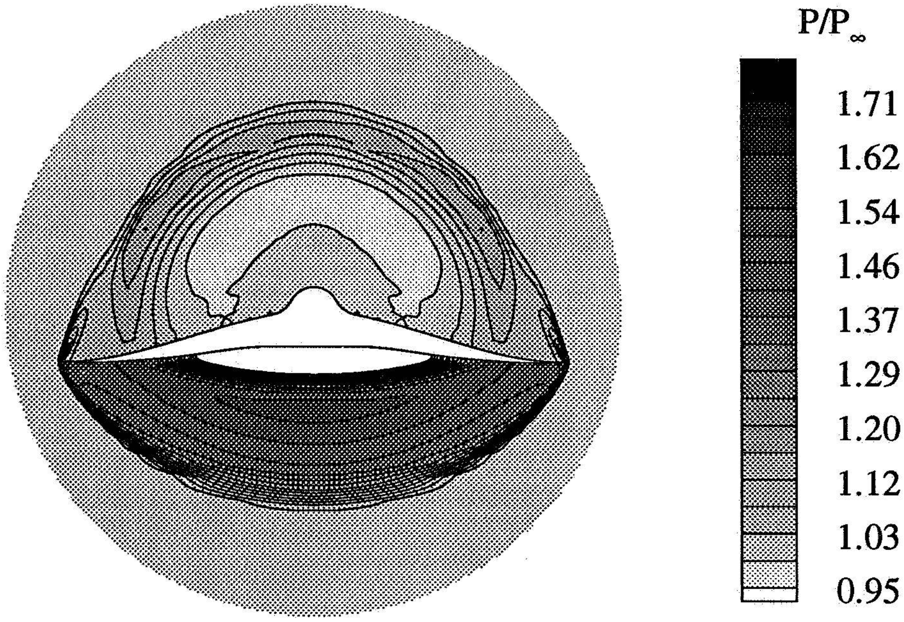

Figure 5.4. Comparison of a base-view vapor-screen photograph and nondimensional static pressure contours from a CFD solution of the straight-wing model at Mach 4.0, $\alpha=0^{\circ}$.

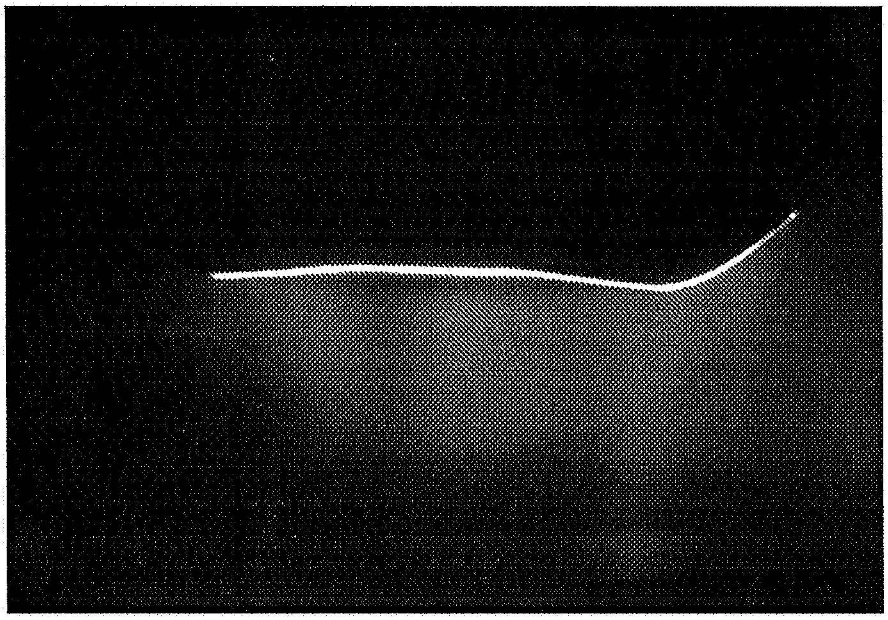

Vapor-Screen Photograph of Base

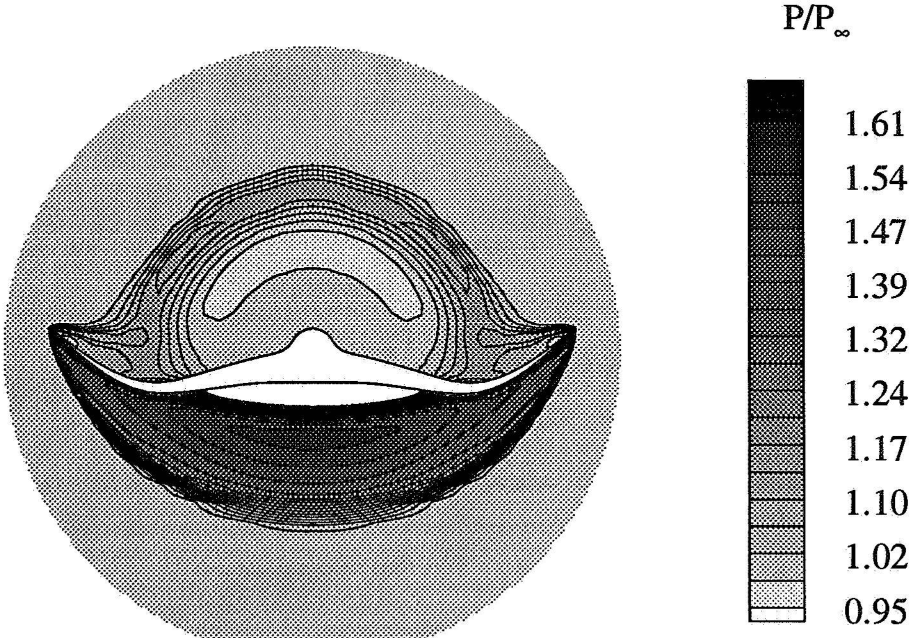

Base View of CFD Solution

Figure 5.5. Comparison of a base-view vapor-screen photograph and nondimensional static pressure contours from a CFD solution of the cranked-wing model at Mach 4.0, $\alpha=0^{\circ}$.

Cranked-Wing Pure Waverider Model

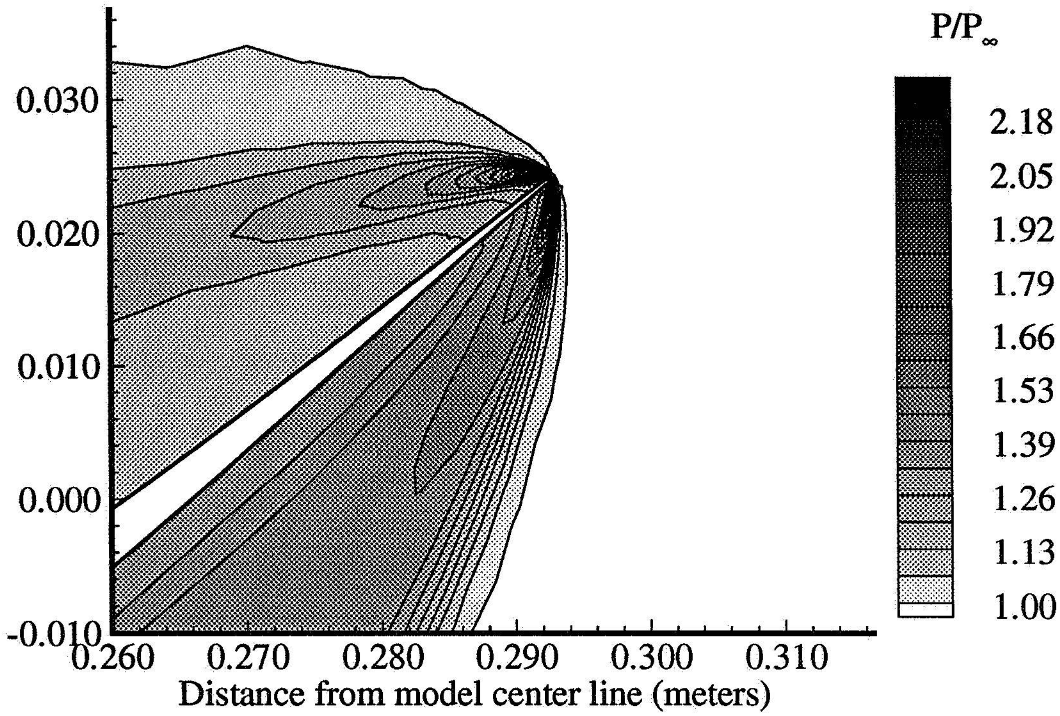

Straight-Wing Pure Waverider Model

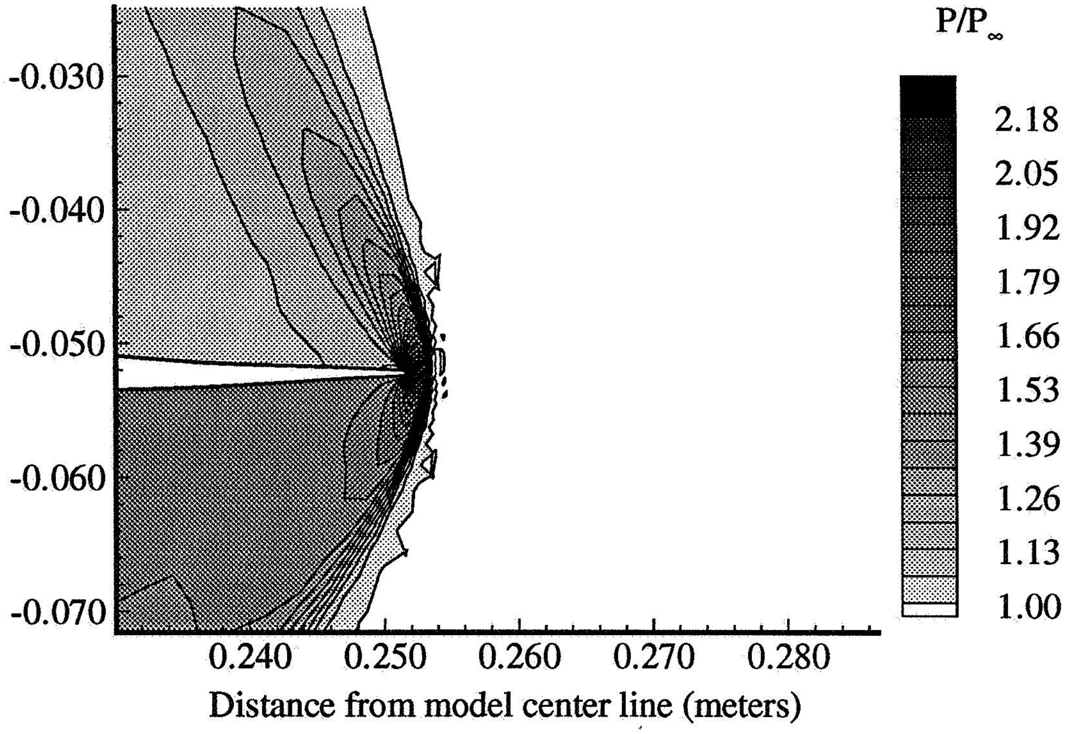

Figure 5.6. Comparison of nondimensional static pressure contours near the leading edge at the base of the cranked and straight pure waverider models from CFD solutions at Mach 4.0, $\alpha=0^{\circ}$.

Vapor-Screen Photograph at Base

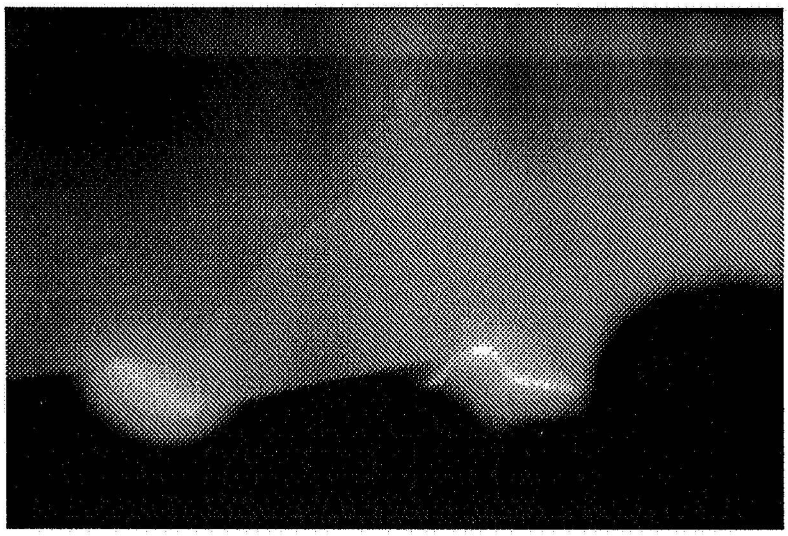

Base View of CFD Solution

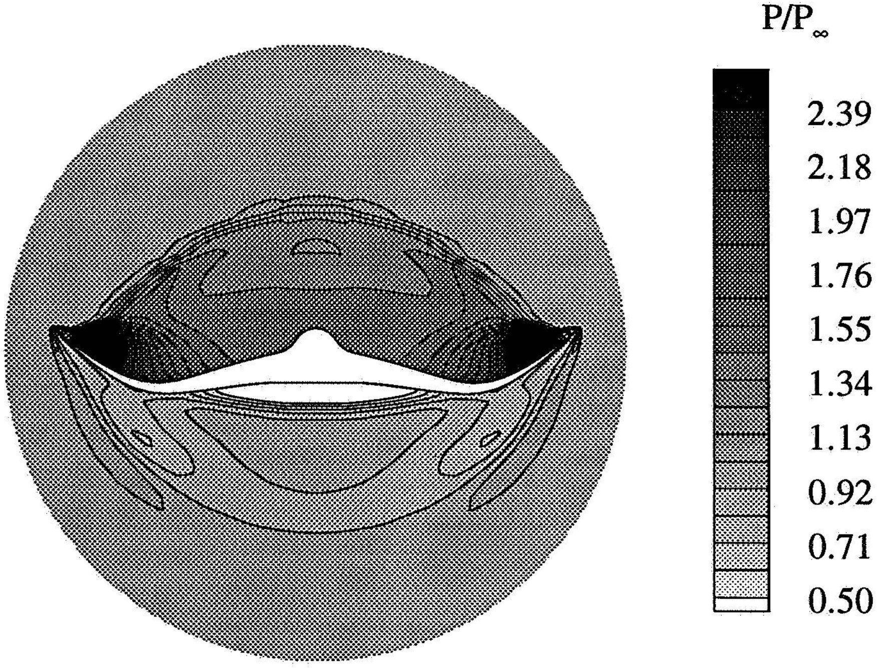

Figure 5.7. Comparison of a base-view vapor-screen photograph and nondiminsional static pressure contours from a CFD solution of the cranked-wing model at Mach 4.0, α=-6^o.

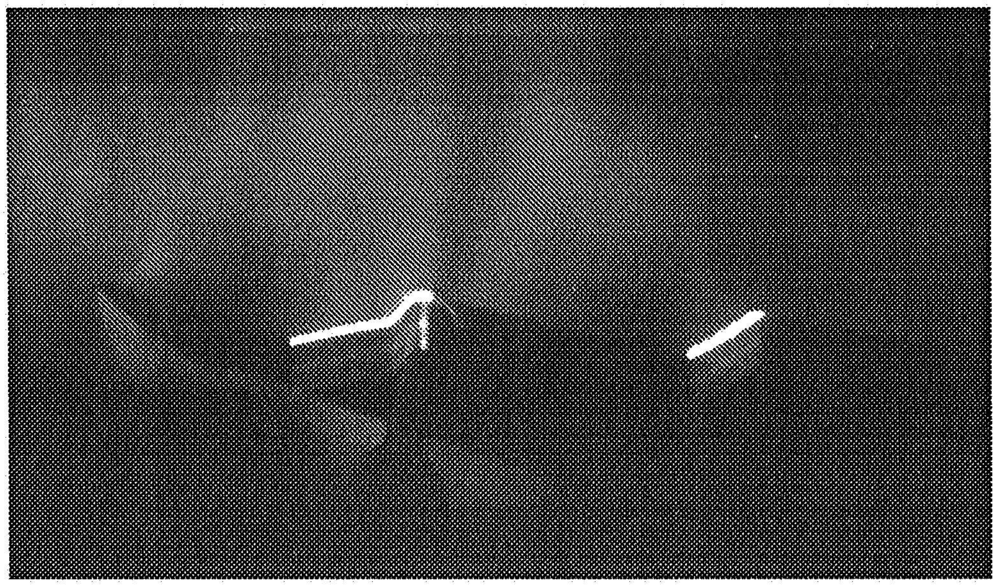

Vapor-Screen Photograph at Base

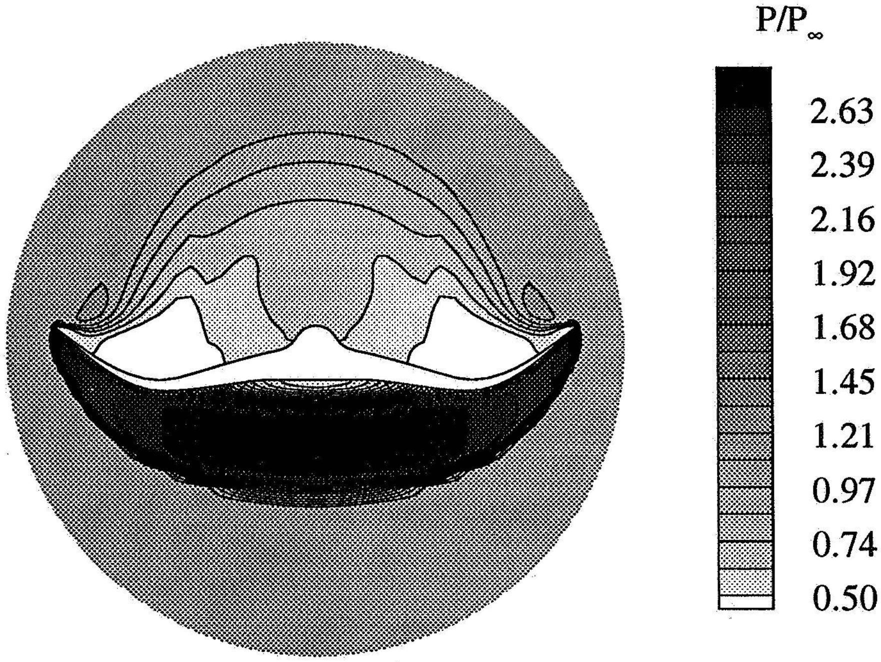

Base View of CFD Solution

Figure 5.8. Comparison of a base-view vapor-screen photograph and nondimensinal static pressure contours from a CFD solution of the cranked-wing model at Mach 4.0, $\alpha=8^{o}$.

Base View of CFD Solution at α=-6°

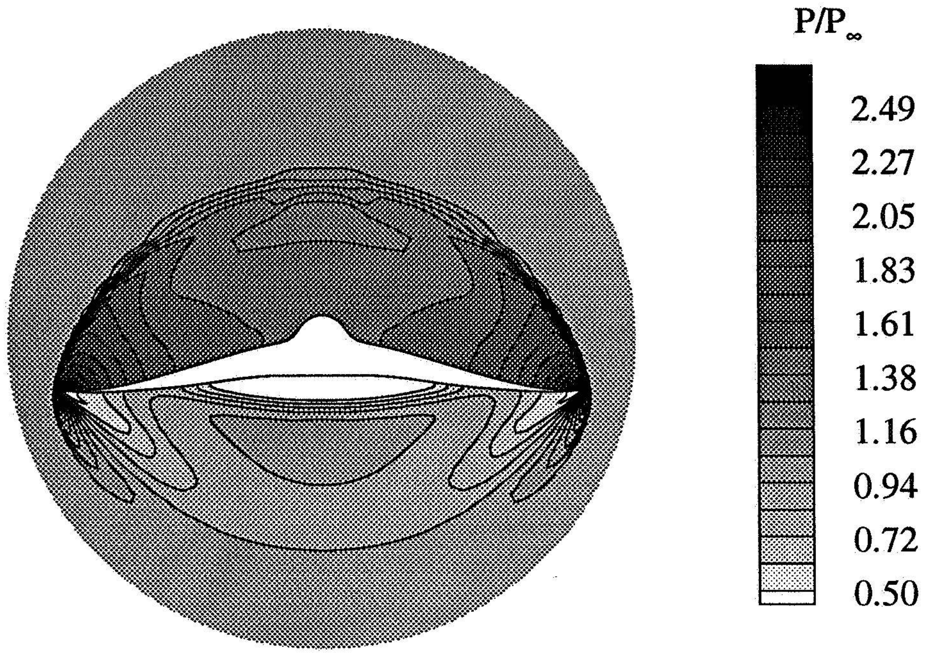

Base View of CFD Solution at α=8°

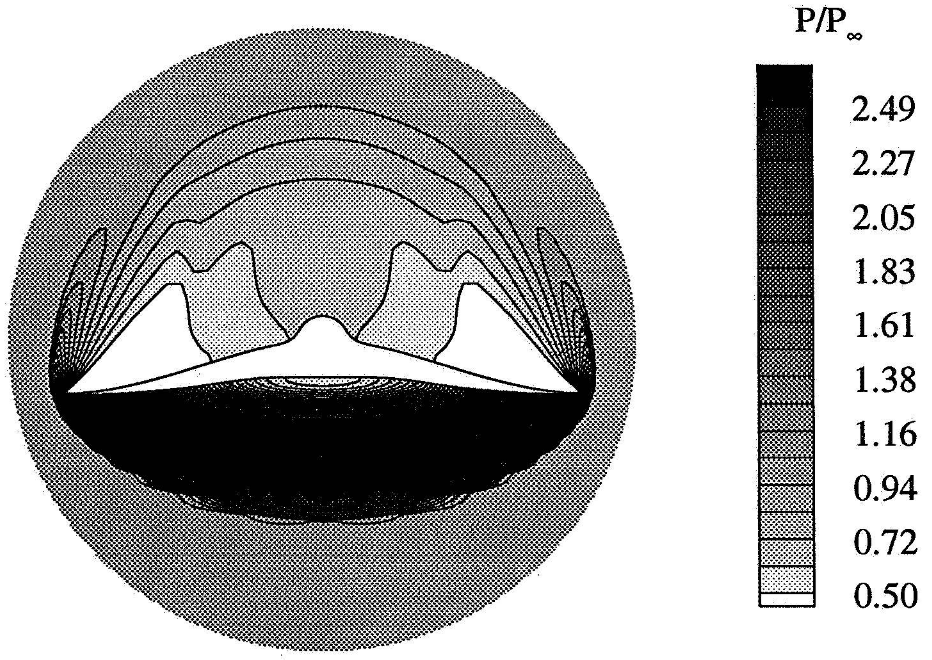

Figure 5.9. Comparison of nondimensional static pressure contours at the base of the straight-wing model from CFD solutions at Mach 4.0 and $\alpha=-6^{\circ}$, 8°.

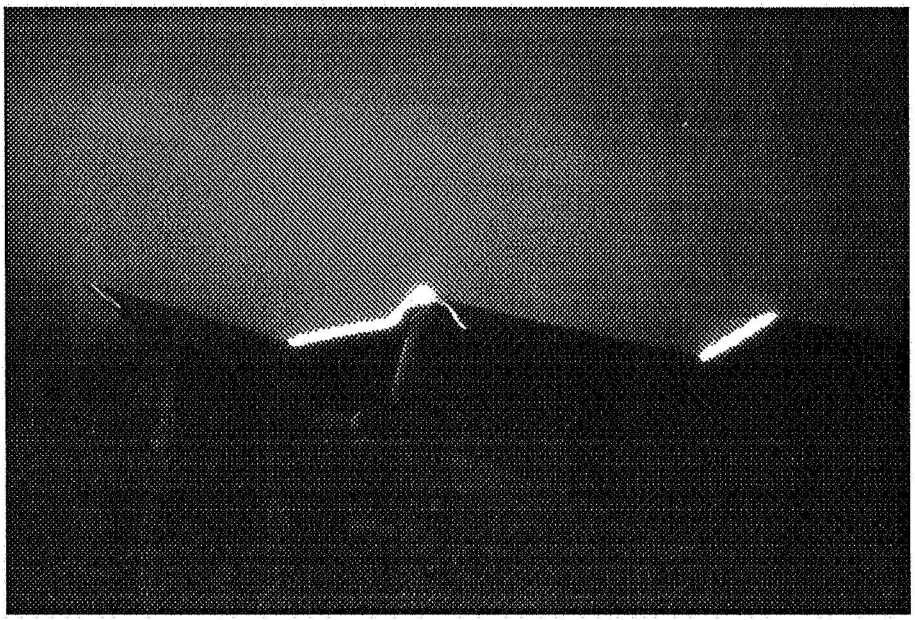

Vapor-Screen Photograph at Base

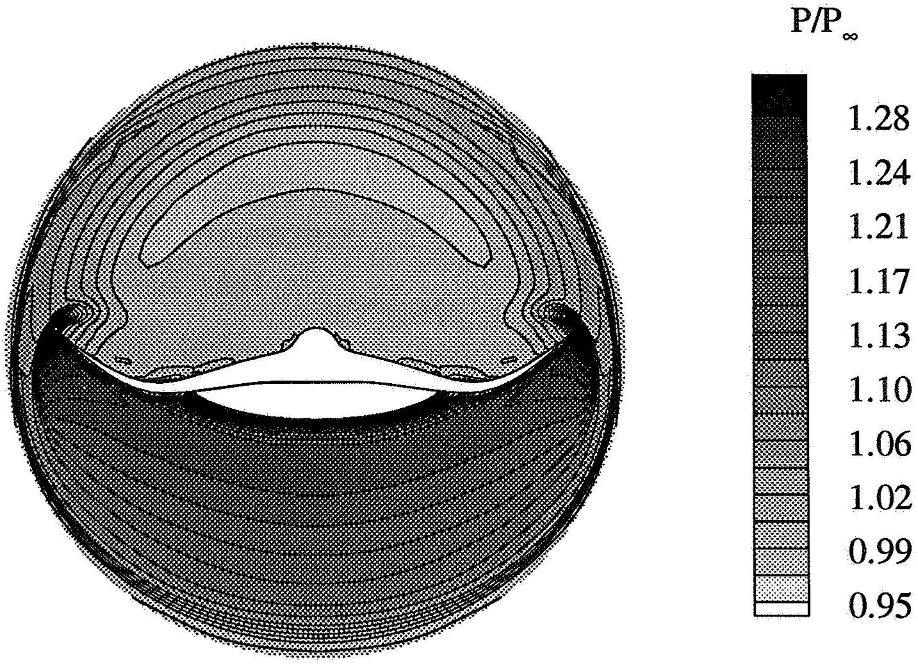

Base View of CFD Solution

Figure 5.10. Comparison of a base-view vapor-screen photograph and nondimensional static pressure contours from a CFD solution of the cranked-wing model at Mach 2.3, $\alpha=0^o$.

Vapor-Screen Photograph 5" Upstream of Base

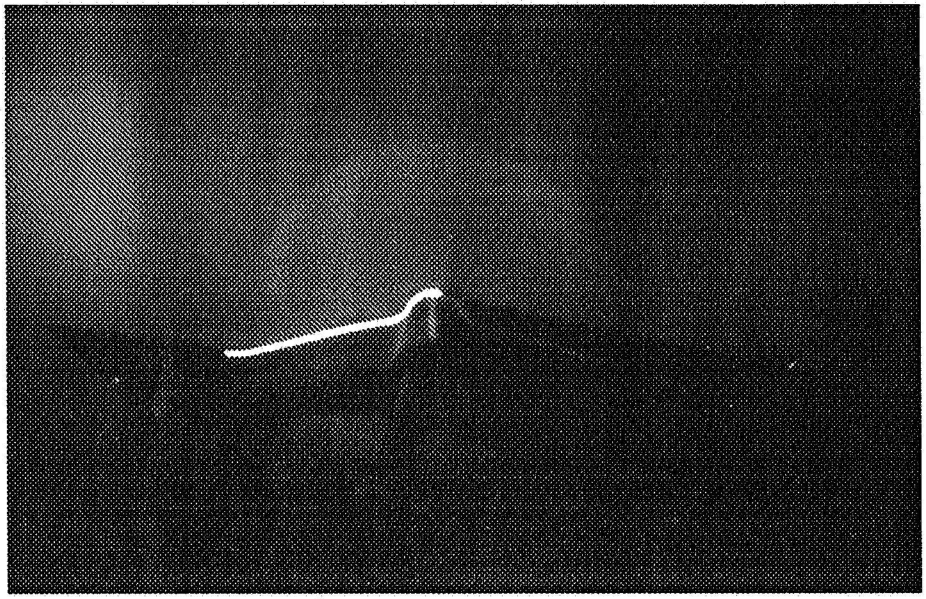

Base View of CFD Solution

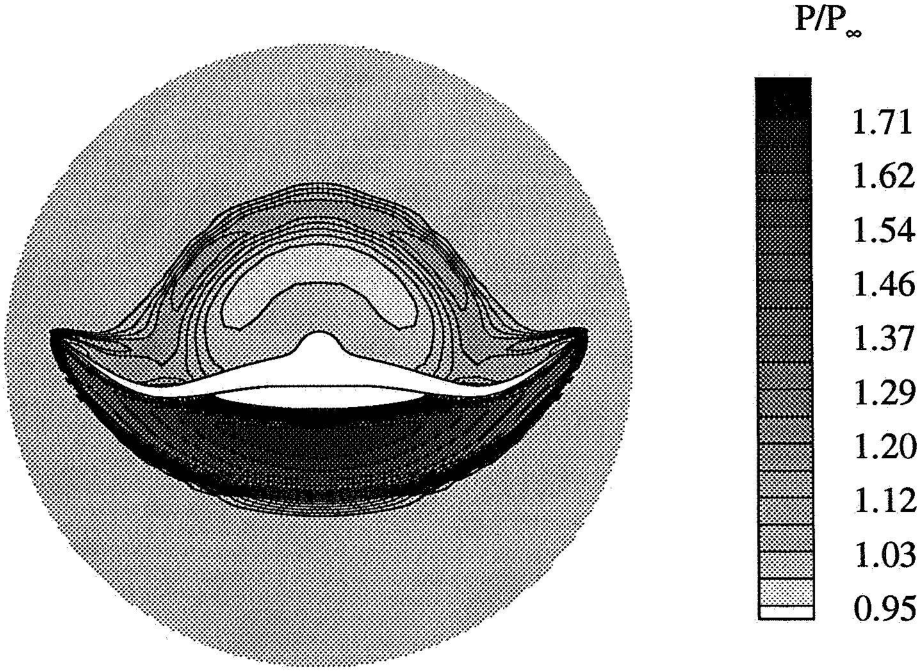

Figure 5.11. Comparison of a base-view vapor-screen photograph and nondimensional static pressure contours from a CFD solution of the cranked-wing model at Mach 4.63, $\alpha=0^o$

Base View of CFD Solution at Mach 2.3

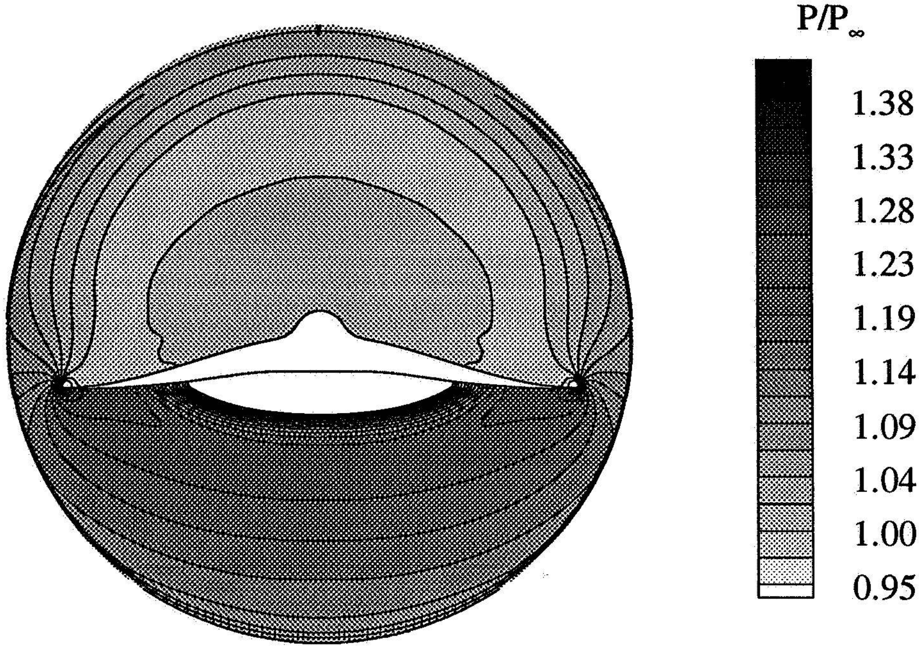

Base View of CFD Solution at Mach 4.63

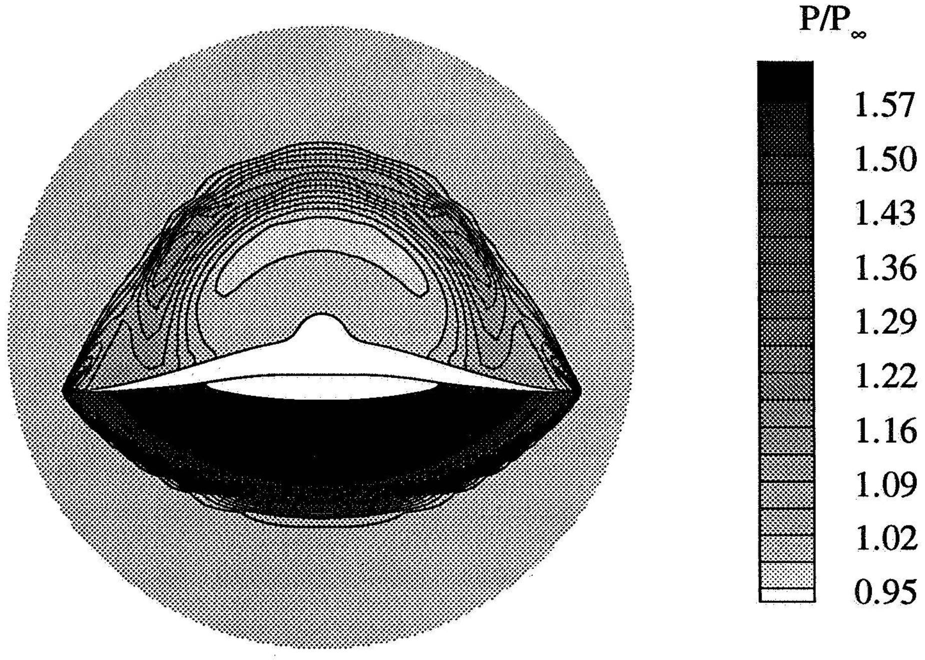

Figure 5.12. Comparison of nondimensional static pressure contours at the base of the straight-wing model from CFD solutions at Mach 2.3 and Mach 4.63 (both at $\alpha=0^{\circ}$).

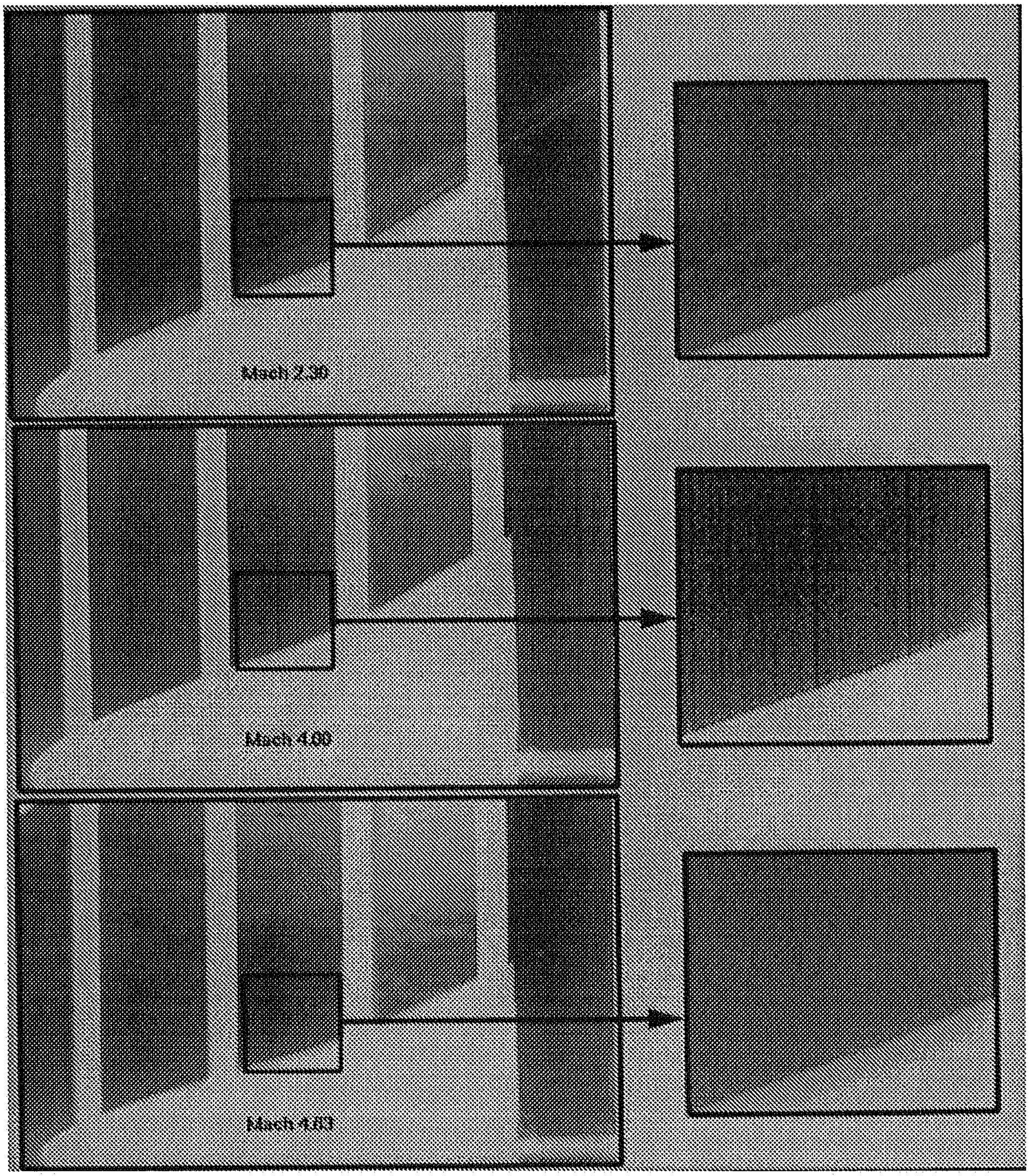

Figure 5.13. Comparison of planform schlieren photographs of cranked-wing model at Mach 2.3, 4.0 and 4.63.

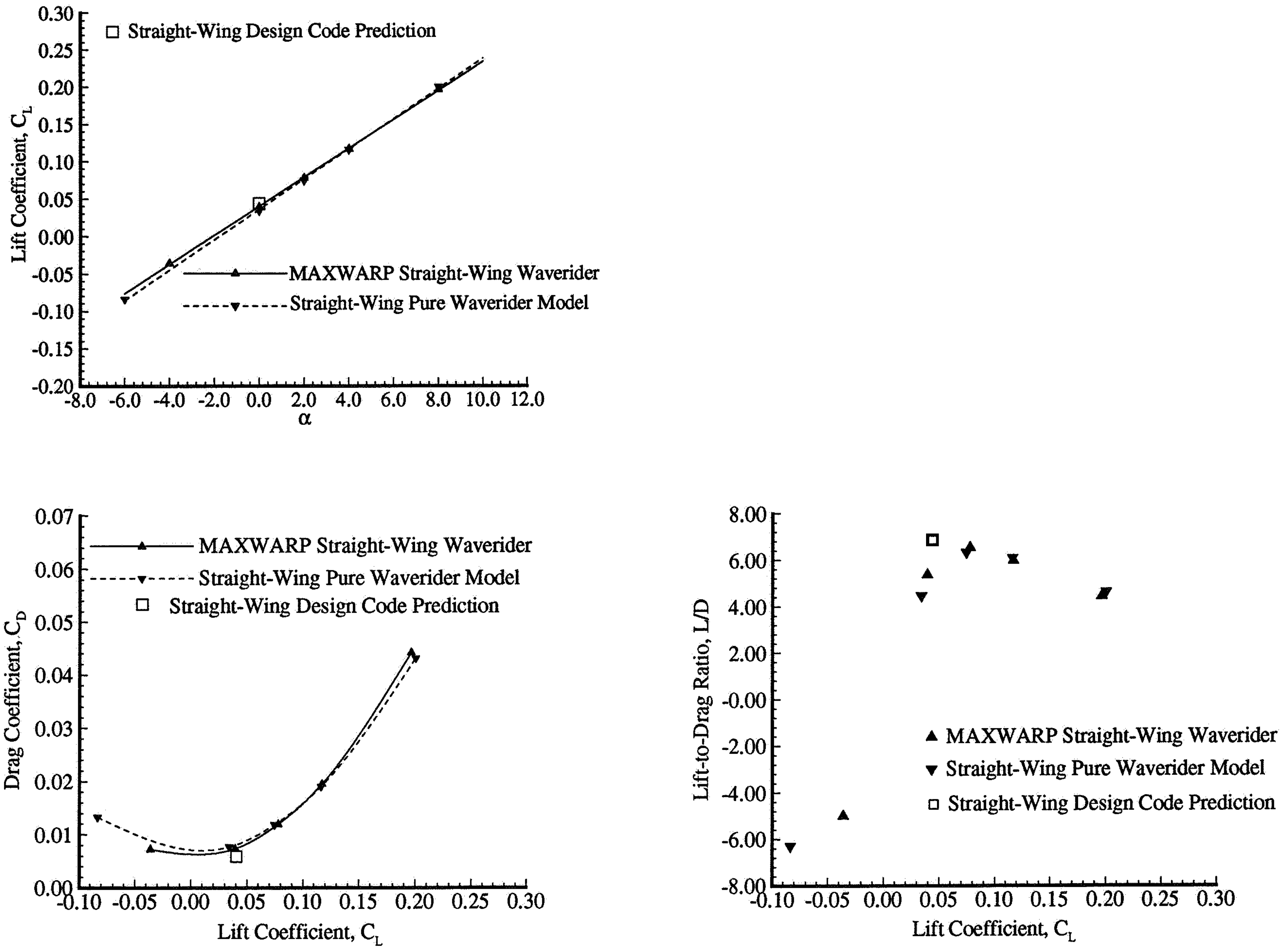

Figure 5.14. Comparison of CFD predictions of aerodynamic performance of the straight-wing design-code shape and the straight-wing pure waverider model at Mach 4.0 and Reynolds number of $2.0\text{x}10^6$ per foot.

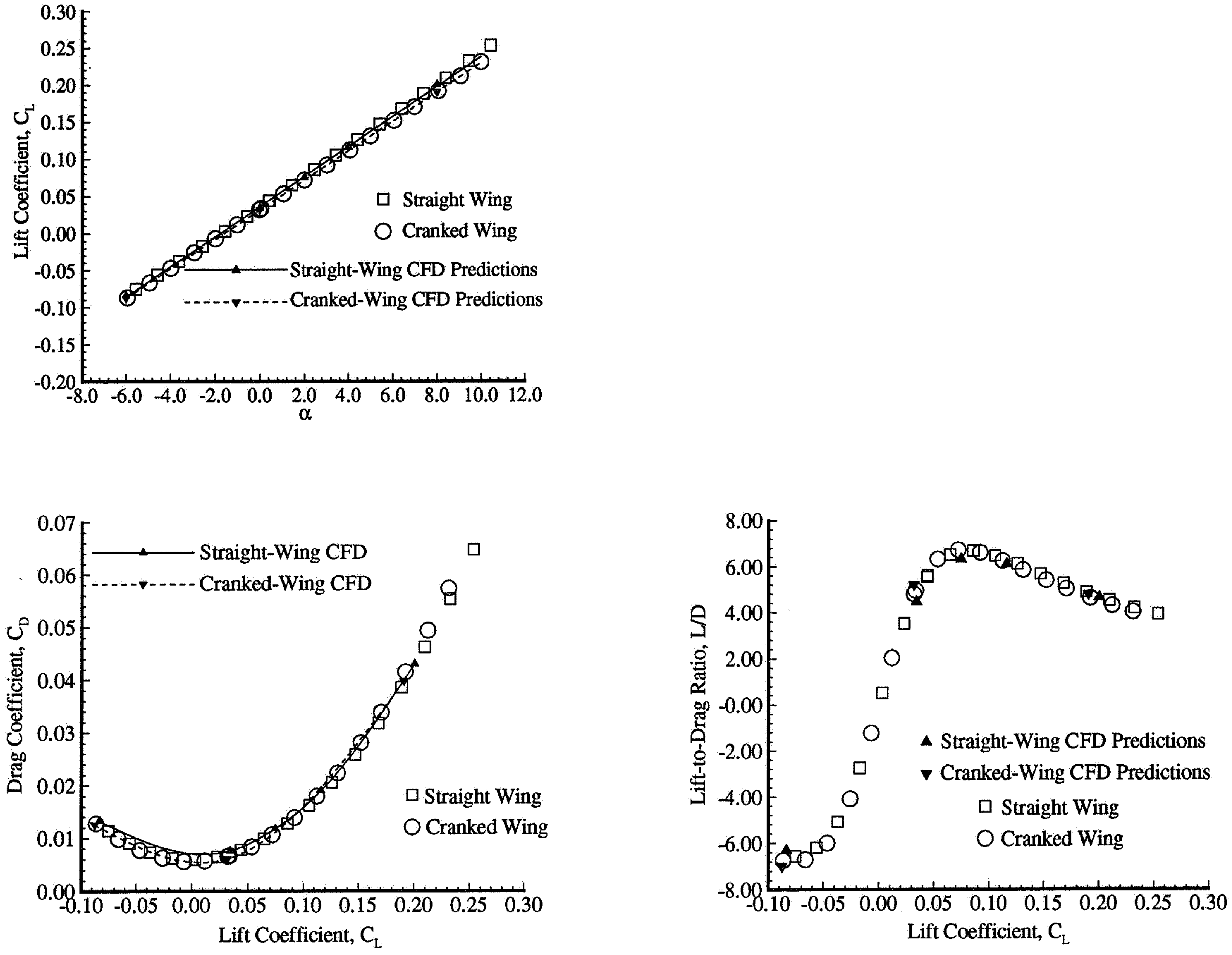

Figure 5.15. Experimental data and CFD predictions for aerodynamic performance of the straight-wing and cranked-wing pure waverider models at Mach 4.0 and Reynolds number of $2.0\text{x}10^6$ per foot.

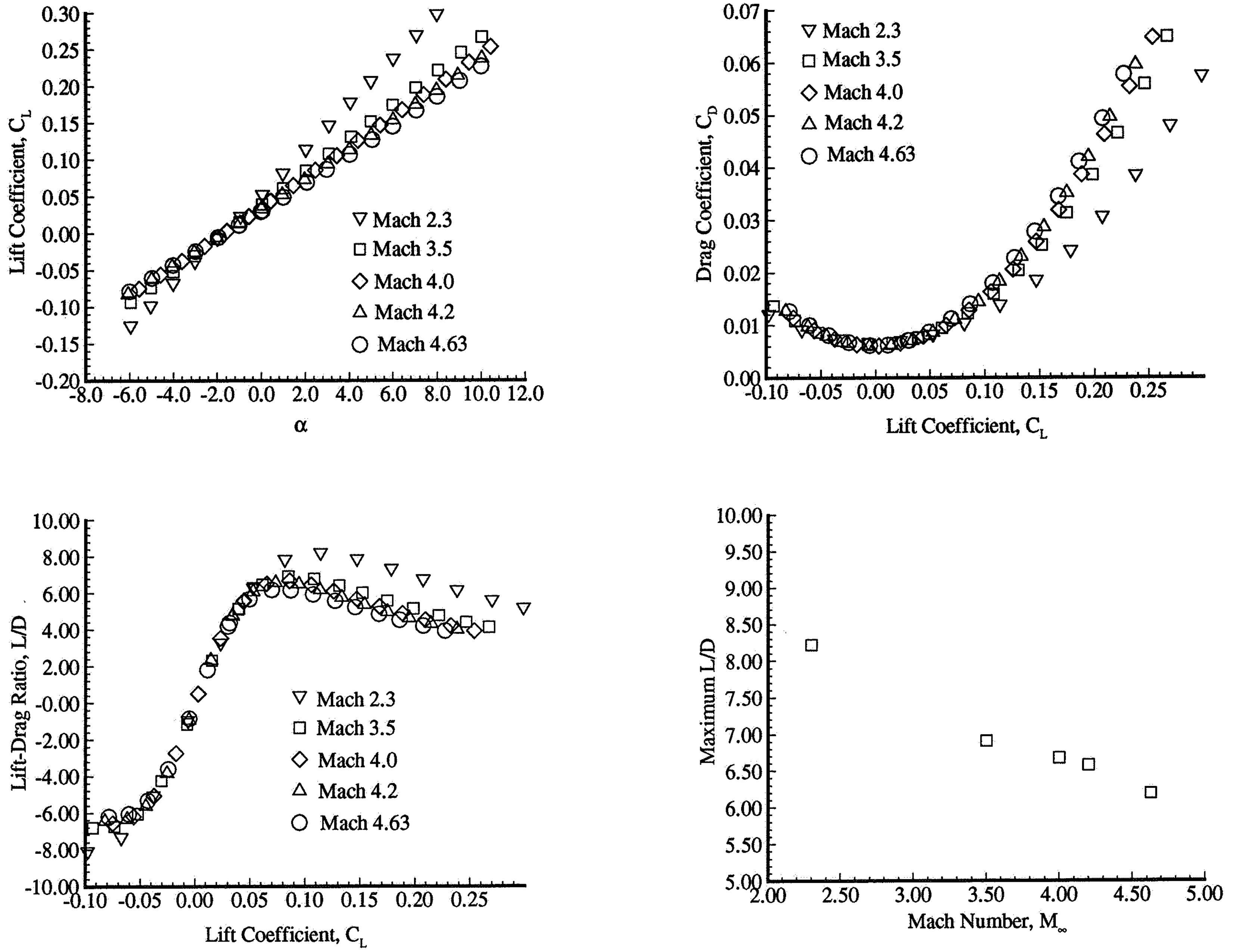

Figure 5.16. Aerodynamic performance of the straight-wing pure waverider model at off-design Mach numbers and a freestream Reynolds number of $2.0\text{x}10^6$ per foot.

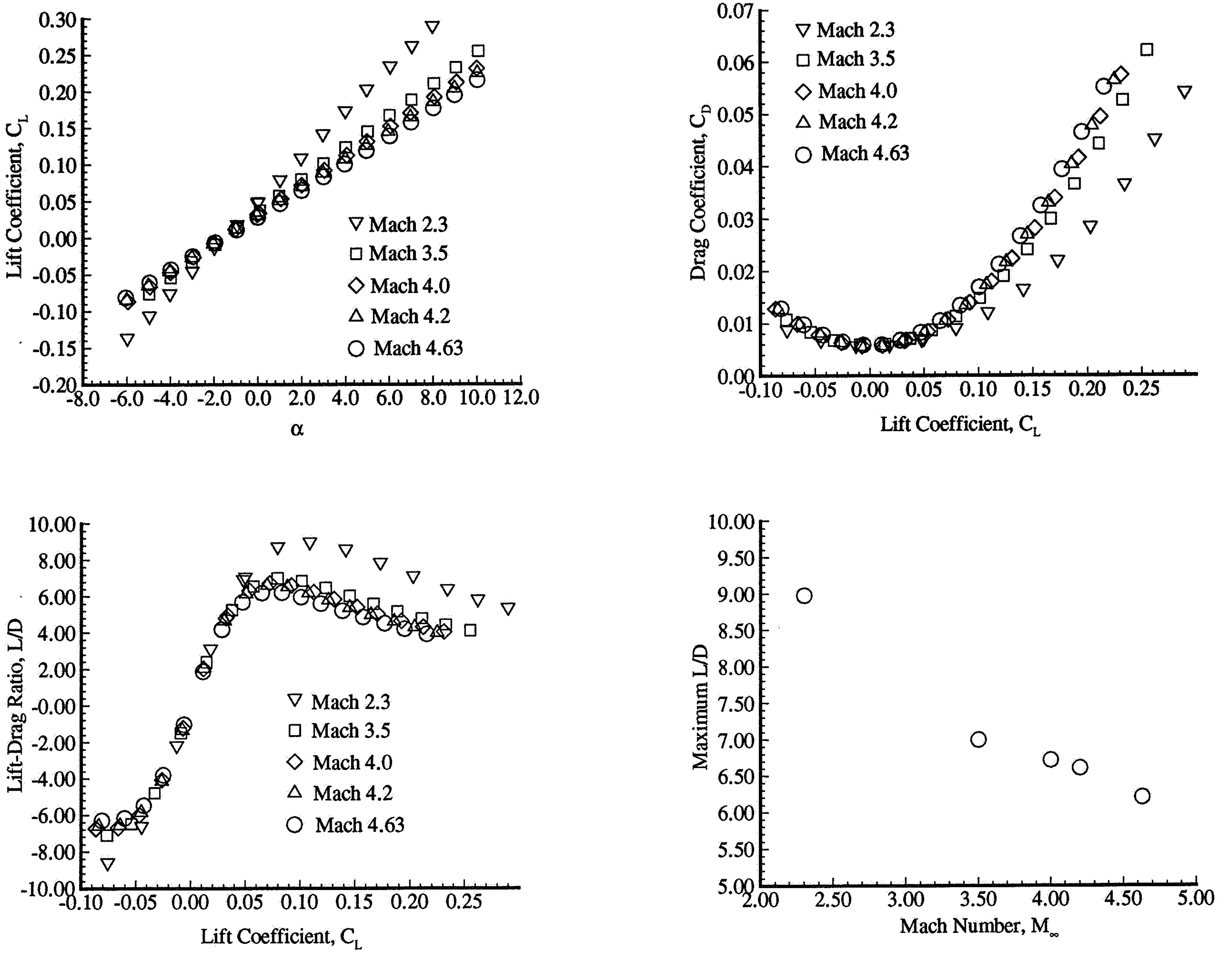

Figure 5.17. Aerodynamic performance of the cranked-wing pure waverider model at off-design Mach Numbers and a freestream Reynolds number of 2.0×10^6 per foot.

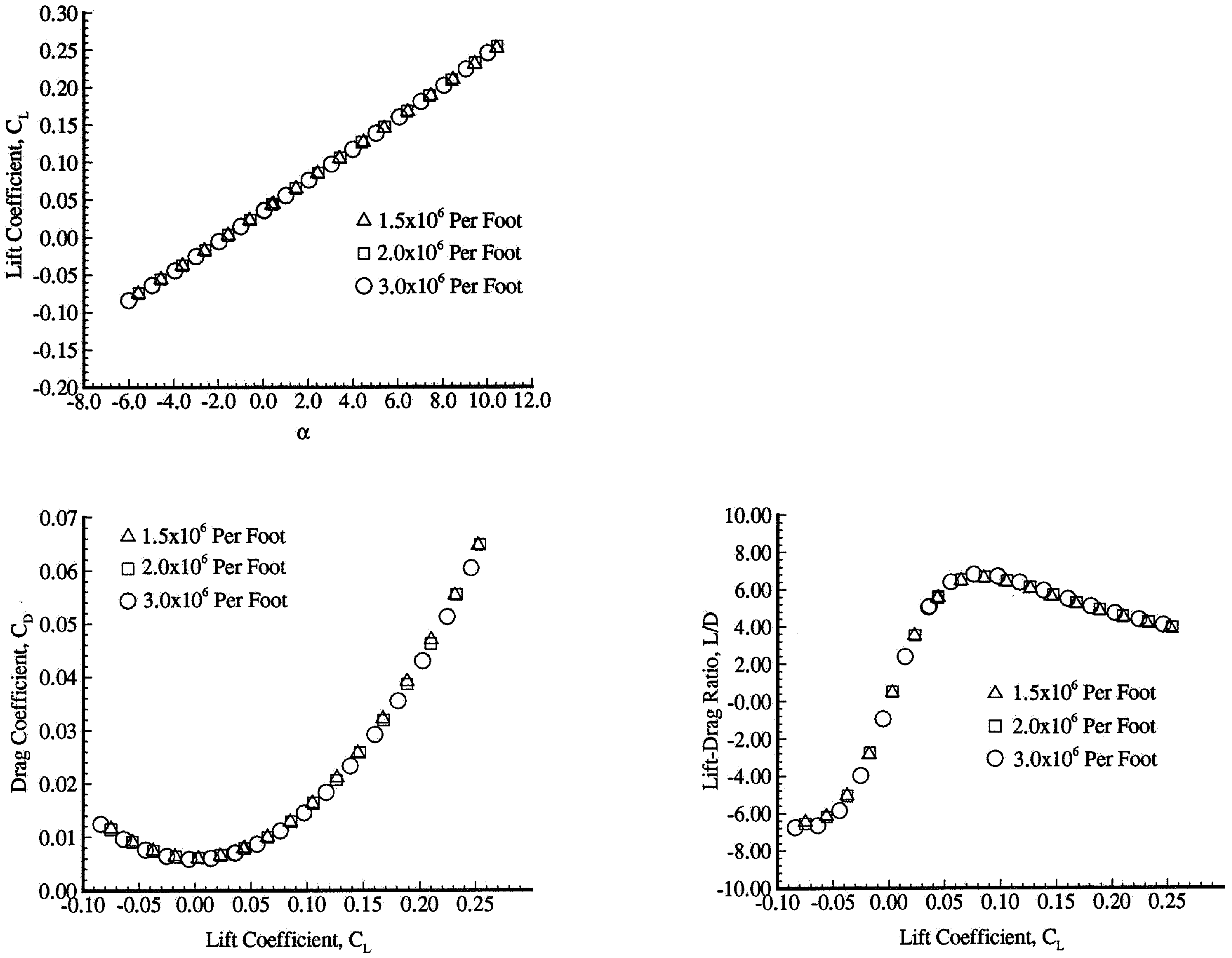

Figure 5.18. Effects of Reynolds number on aerodynamic performance of the straight-wing configuration at Mach 4.0.

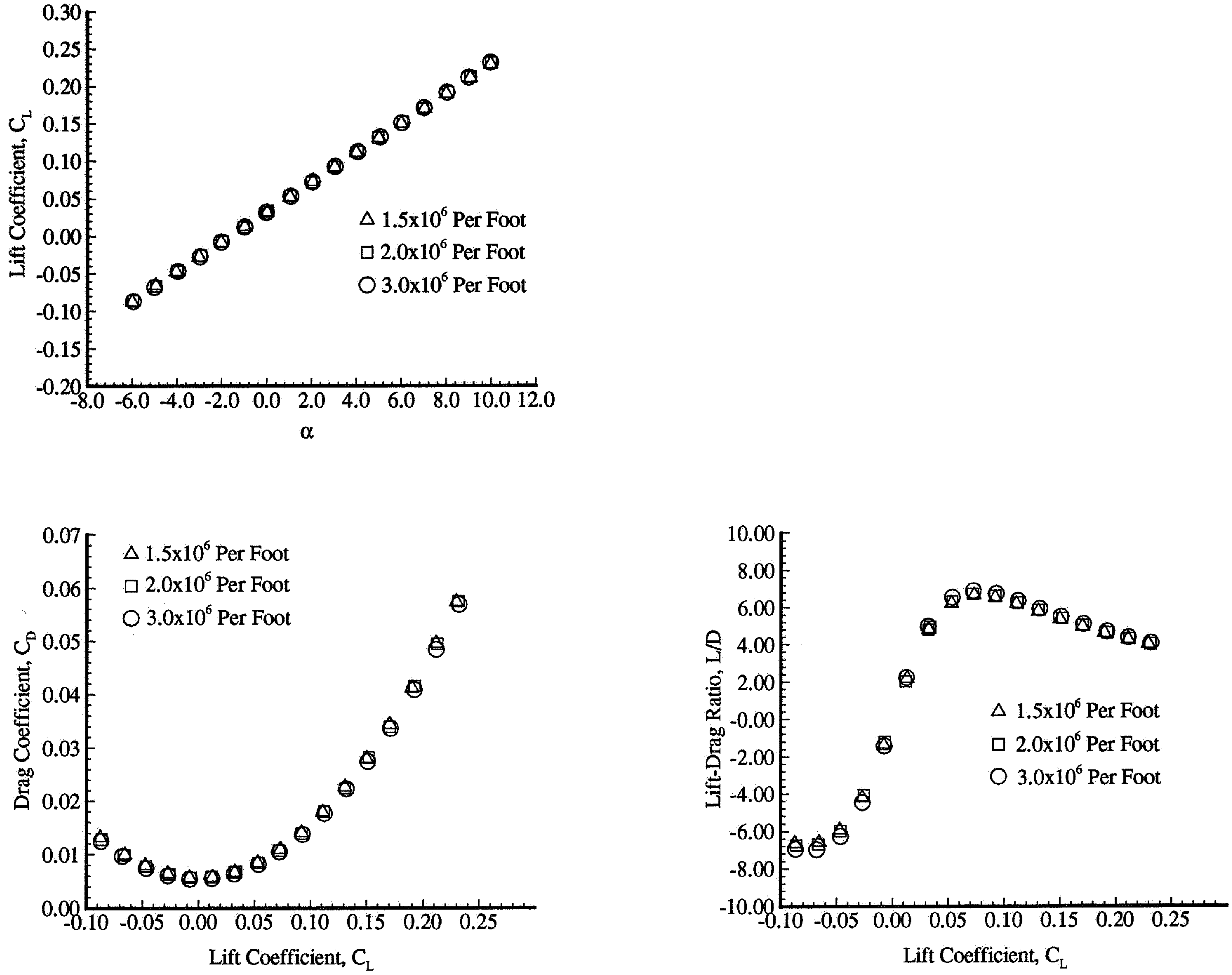

Figure 5.19. Effects of Reynolds number on aerodynamic performance of the cranked-wing configuration at Mach 4.0.

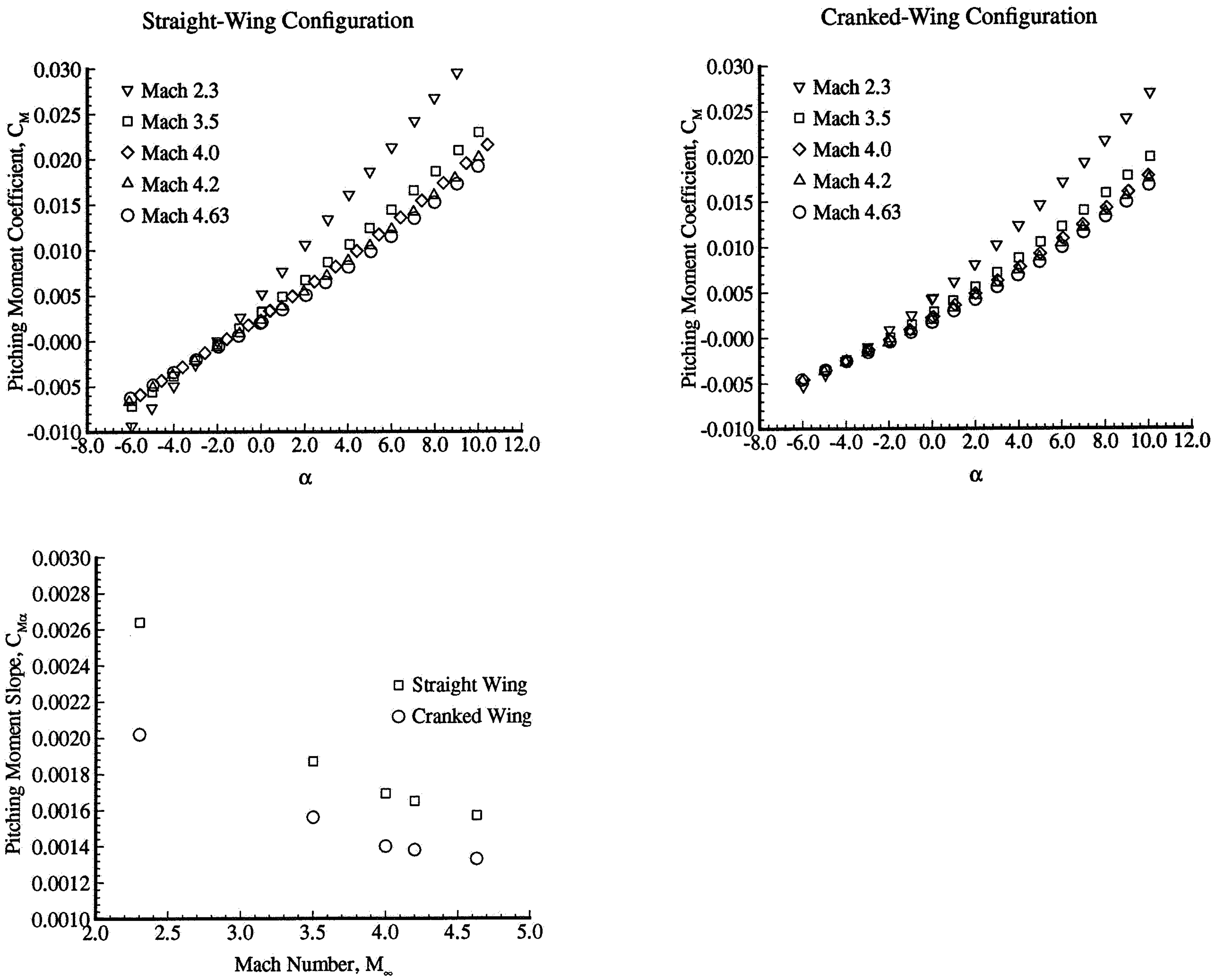

Figure 5.20. Pitching moment characteristics of the straight-wing and cranked-wing pure waverider configurations.

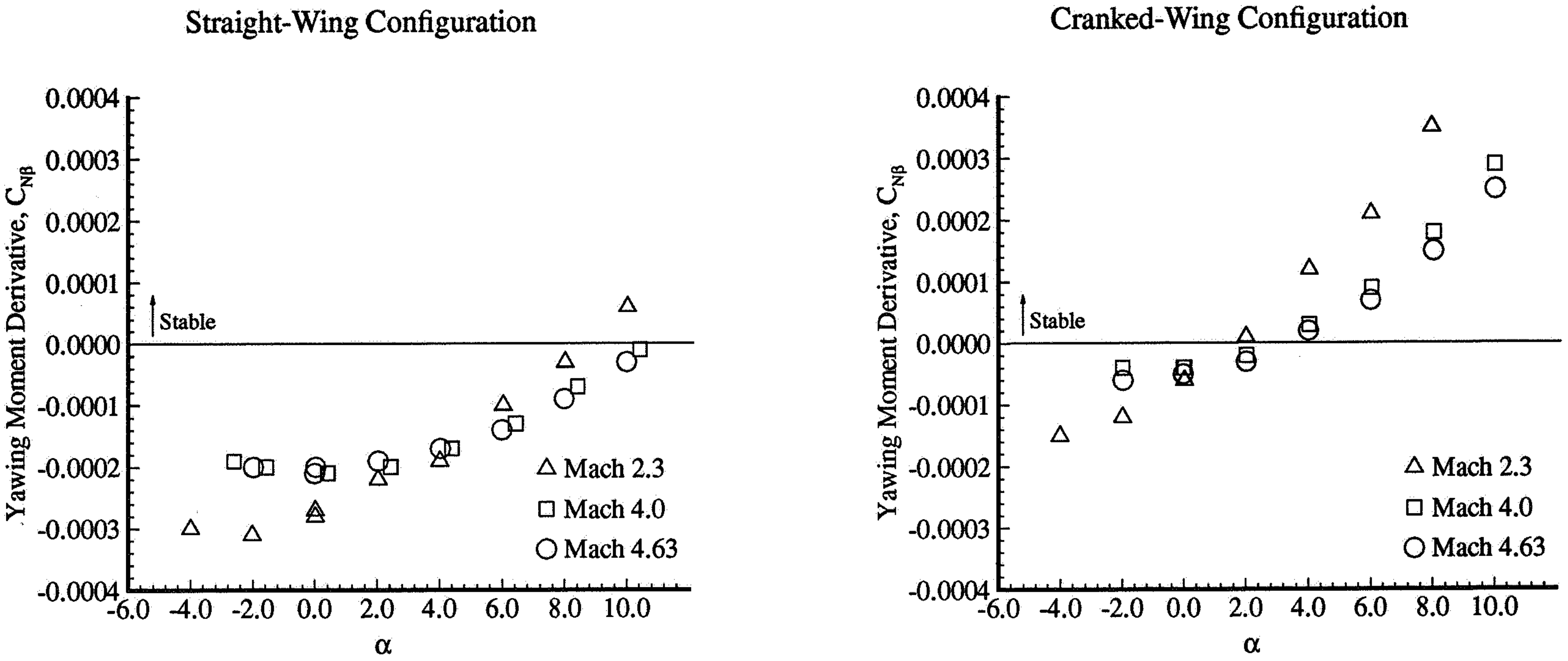
Straight-Wing Configuration

Cranked-Wing Configuration

Figure 5.21. Yawing moment characteristics of the straight-wing and cranked-wing pure waverider configurations.

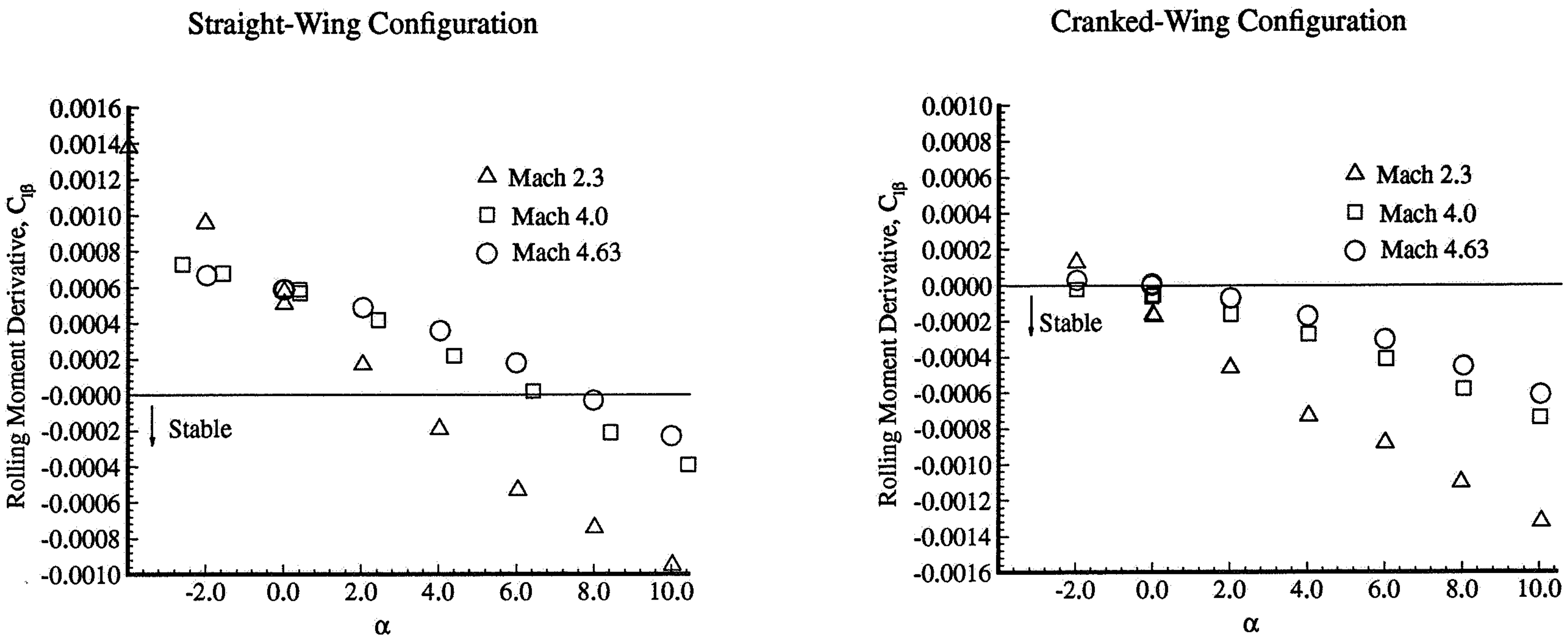

Figure 5.22. Rolling moment characteristics of straight-wing and cranked-wing pure waverider configurations.

C-2.

CHAPTER 6
COMPONENT BUILD-UP EFFECTS

6.0 Summary

The effects of component buildup on both the straight and cranked waverider shapes are examined by presenting comparisons of experimental data from various configurations. The effects of the canopy on aerodynamic performance and the effects of adding engine components and adding 0^o control surfaces on aerodynamic performance and stability are examined. The issue of control surface effectiveness is not addressed in this study. Finally, comparisons between the fully-integrated configurations and the pure waverider configurations are made in order to quantify the differences in aerodynamic performance and stability in integrating the waverider into a realistic hypersonic cruise vehicle.

6.1 Canopy Effects

The effects of the canopy on the aerodynamic performance of the straight-wing and cranked-wing configurations are illustrated in figures 6.1 and 6.2, respectively. The configurations shown here have no control surfaces or engine components attached and the data are corrected to assume freestream pressure acting at the base. Each figure shows the lift and drag coefficients at Mach 4.0, lift-to-drag ratio at three different Mach numbers and the maximum lift-to-drag ratio at each Mach number studied for the smooth-canopy and faceted-canopy configurations. Since a "canopy-off" configuration could not be tested, comparisons between the faceted canopy and the smooth canopy are used to provide an indication of how the aerodynamic performance is affected by the addition of a realistic canopy to the waverider forebody. Both the straight-wing and cranked-wing configurations show little difference in lift when the canopy is changed. The faceted-canopy configurations show slightly higher drag than those with the smooth canopy. The result is a decrease in lift-to-drag ratio at positive values of lift over the Mach number range studied when the faceted canopy is substituted for the smooth canopy. There is a 3.6 percent reduction in lift-to-drag ratio at Mach 4.0 for the straight-wing configuration and a 5.1 percent reduction for the cranked-wing configuration. This analysis indicates that the primary effect of adding a realistic canopy is a slight degradation in aerodynamic performance.

6.2 Engine Component Effects

The engine component effects are evaluated by comparing experimental data from engine-on and engine-off configurations. Figures 6.3 and 6.4 show the effects of adding the engine inlet and nozzle components to the straight-wing and cranked-wing configurations, respectively. The configurations shown here have the faceted canopy and no control surfaces integrated, and the data are corrected to assume freestream pressure acting at the base. Each figure shows lift and drag coefficients at Mach 4.0, lift-to-drag ratios at three different Mach numbers and the maximum lift-to-drag ratio at each Mach number studied for engine-on and engine-off configurations. The addition of engine components results a slight increase in lift and a significant increase in drag at Mach 4.0. These effects are caused by the inlet compression surface and the increase in projected frontal area. This results in a significant decrease in lift-to-drag ratio at positive values of lift over the Mach number range studied. The effect of the addition of engine components on drag and on lift-to-drag ratio is decreased as angle of attack increases. The straight-wing engine-on configuration shows a 19.7 percent reduction in the maximum lift-to-drag ratio at Mach 4.0 over the engine-off configuration. The cranked-wing model shows a 17.7 percent reduction at the same conditions.

The same data are shown in figures 6.5 and 6.6 for the straight-wing and cranked-wing models with both the base pressures and the nozzle surface pressures corrected to freestream pressure. These data are presented to show the comparative aerodynamic performance without any propulsive effect on the nozzle surface, as discussed in chapter 3. The nozzle pressures were corrected by assigning integrated areas to each pressure tap and then correcting the force components to assume freestream pressure acting at the nozzle surface. The data with the nozzle pressures corrected show that there is a larger increase in lift and a smaller increase in drag, compared to the uncorrected data, when engine components are added to each configuration. There is an increase in maximum lift-to-drag ratio at Mach 2.3. This is a result of higher freestream pressure at this Mach number, thereby resulting in a relatively large increment in lift for engine-on configurations when compared to higher Mach numbers. At all other Mach numbers studied, the maximum lift-to-drag ratio decreases when the engine components are added. At Mach 4.0, the engine-on model shows a 7.61 percent reduction in maximum lift-to-drag ratio for the straight-wing configuration and a 6.42 percent reduction for the cranked-wing configuration. This analysis indicates that the primary effect on aerodynamic performance of integrating the propulsion system is a degradation of the performance resulting from the significant increase in drag.

The addition of engine components has a less significant effect on the longitudinal, lateral and directional stability characteristics of each configuration. Figures 6.7 and 6.8 show the effect of adding the engine package on the longitudinal and lateral-directional stability of the straight-wing and cranked-wing configurations, respectively. Each figure shows pitching moment at Mach 4.0, pitching-moment curve slope at each Mach number studied, the yawing moment derivative, $C_{N\beta}$,and rolling moment derivative, $C_{L\beta}$, at each Mach number studied. The addition of engine components provides a further destabilizing shift in longitudinal stability, caused by the inlet compression surface, as evidenced by an increase in the pitching moment curve slope at each Mach number investigated. Both the straight-wing and cranked-wing engine-on configurations are longitudinally unstable across the Mach number range studied. The engine components cause a stabilizing shift in directional stability, as evidenced by increasing values of yawing moment derivatives, at each angle of attack over the Mach number range studied. The increase in $C_{N\beta}$ is due to the increased side force created by the inlet side walls. The straight-wing engine-on configuration is directionally unstable at most conditions, while the cranked-wing engine-on configuration is stable at angles of attack above 4^o. The addition of engine components also causes a stabilizing shift in lateral stability for both configurations, as evidenced by decreasing values of rolling moment derivatives at each angle of attack over the Mach number range studied. The straight-wing model is laterally stable at angles of attack above 2^o at Mach 2.3 and above 6^o at Mach 4.0 and Mach 4.63. The cranked-wing model is stable above angles of attack of 0^o.

6.3 Control Surface Effects

The effects of adding 0^o control surfaces are illustrated by comparing configurations with no control surfaces to those with 0^o ailerons and 0^o elevons attached. Each configuration also has the faceted canopy and engine packages integrated. Data for both the straight-wing and cranked-wing configurations are shown. The coefficient data are reduced by the planform areas of each corresponding configuration so the effects of increased planform are accounted for in the normalization of these data.

The effect of adding 0^o control surfaces to the straight-wing waverider configuration is summarized in figure 6.9. This figure shows the lift and drag coefficients at Mach 4.0, lift-to-drag ratios at each Mach number studied and the maximum lift-to-drag ratios at each Mach number for both the controls-on and controls-off case. The addition of control surfaces causes a decrease in lift coefficient at Mach 4.0. This is partially caused by the large expansion angle which is present on the elevon lower surfaces. There is also a significant increase in drag, partially due to a large thrust component acting at the base in the controls-off case, which comes from the assumption of freestream pressure acting at the base. This component of force does not exist in the controls-on case because of the significantly smaller base area. Because the two configurations compared have significantly different base areas, the increase in drag is deceptive and is not due purely to any aerodynamic effect. However, the assumption of freestream pressure acting at the base is consistent with the design method, so the data presented here provide an accurate representation of the performance degradation from predicted design values due to the closure of the blunt base. A significant decrease in maximum lift-to-drag ratio is observed at all Mach numbers studied. The maximum lift-to-drag ratio of the controls-on configuration does not vary significantly across the Mach number range. The addition of control surfaces causes a 13.9 percent reduction in maximum lift-to-drag ratio of the straight-wing configuration at Mach 4.0. The effects of control surface addition on the cranked-wing configuration are identical to that of the straight-wing model. Figure 6.10 summarizes these effects. The addition of 0^o control surfaces causes a 17.7 percent reduction in the maximum lift-to-drag ratio at Mach 4.0 for this configuration.

The addition of 0^{o} control surfaces causes a stabilizing shift in pitching moment curve slope and enhances lateral-directional stability. Figures 6.11 and 6.12 show the longitudinal and lateral-directional stability characteristics of the straight-wing and cranked-wing configurations, respectively. Each figure shows the pitching moment values at Mach 4.0, pitching-moment curve slope values at each comparative Mach number and yawing and rolling moment derivatives at each Mach number studied for controls-on and controls-off configurations. The addition of control surfaces causes a decrease in pitching-moment curve slope for both the straight-wing and cranked-wing configurations indicating improved longitudinal stability, although both configurations are unstable. There is also a slight positive shift in yawing moment derivative values, indicating enhanced directional stability. There is a slight negative shift in rolling moment derivative values, indicating an improvement in lateral stability. The exception to this trend is a slight destabilizing shift observed for the straight-wing configuration at angles of attack above 2^{o} at Mach 4.0.

6.4 Vertical Tail Effects

The effect of the vertical tail is to significantly enhance the directional stability of both the straight-wing and cranked-wing configurations. Figure 6.13 shows the effect of the vertical tail on yawing moment derivative values for each configuration. The configurations shown in this figure have the faceted canopy, engine components, 0^{o} ailerons and 0^{o} elevons installed. Comparisons are made for vertical tail-off and vertical tail-on configurations for each leading edge shape. The addition of the vertical tail causes a large positive increase in yawing moment derivatives, indicating enhanced directional stability. Both the straight-wing and cranked-wing configurations are directionally stable at all Mach numbers investigated with the vertical tail and all other control surfaces installed.

6.5 Comparison of Waverider-Derived Configurations with Pure Waverider Shapes.

The final step in the analysis of component buildup effects is to compare the aerodynamic performance and stability characteristics of the fully-integrated waverider-derived configurations with the pure waverider configurations. As previously discussed, the pure waverider configurations presented in this section have the smooth canopy with no engine components or control surfaces integrated. The fully-integrated configurations have the faceted canopy, engine/inlet and nozzle, 0^{o} ailerons, 0^{o} elevons and a vertical tail attached. Aerodynamic performance data are presented along with longitudinal, lateral and directional stability data. Comparisons are made for both the straight-wing and cranked-wing configurations.

Comparisons of the aerodynamic performance of the straight-wing pure waverider model and the fully-integrated configuration are shown in figure 6.14 and 6.15. Figure 6.14 shows lift and drag coefficients at Mach 4.0, lift-to-drag ratios at each Mach number studied and the maximum lift-to-drag ratios at each comparative Mach number. These data are presented with the base pressures corrected to freestream pressure, but with the nozzle surface pressures uncorrected. The aerodynamic performance of the fully-integrated configuration is significantly degraded from that of the pure waverider shape. A reduction in lift coefficient for the fully-integrated configuration is observed at Mach 4.0 above 0^{o} angle of attack, due to the severe closure angle of the elevon surfaces. The difference in lift coefficient values between the two configurations increases as angle of attack increases. A significant increase in drag is observed when all components are integrated with the pure waverider model. Part of this increase is again due to the significantly different base areas between the two configurations and the assumption of freestream pressure acting at the base. The result is a significant decrease in lift-to-drag ratio at all Mach numbers studied. The maximum lift-to-drag ratio of the fully-integrated model is 4.39 compared to 6.68 for the pure waverider model. This corresponds to a 34.5 percent decrease when all components are integrated. The maximum lift-to-drag ratio for the fully-integrated configuration occurs at a 2^{o} angle of attack and no significant performance degradations are observed at off-design Mach numbers for this configuration. In fact, the maximum lift-drag ratios of the fully-integrated configuration are relatively constant across the Mach number range investigated. Figure 6.15 shows the same data presented with the nozzle surface pressures corrected to freestream pressure. These data provide an accurate assessment of the effects of modifying the waverider airframe to integrate engine components, since no propulsive forces are included. Using this method, there is a smaller increase in drag than with the nozzle pressures uncorrected. This results in smaller decreases in lift-to-drag ratios at positive values of lift at each Mach number studied. There is still a significant decrease in maximum lift-to-drag ratios when comparing the pure waverider to the fully-integrated model at each Mach number studied. From the data with the nozzle surface pressures corrected, the maximum lift-to-drag ratio of the fully-integrated configuration at Mach 4.0 is 4.69, which corresponds to a 29.8 percent decrease from that of the pure waverider model.

A comparison of the fully-integrated cranked-wing configuration and the pure cranked leading-edge waverider model yields conclusions similar to those of the comparison of the straight-wing configurations. Figures 6.16 and 6.17 show the aerodynamic performance of these two configurations with only the base pressures corrected to freestream pressure and with both the base and nozzle surface pressures corrected to freestream pressure, respectively. The maximum lift-to-drag ratio at Mach 4.0 of the fully-integrated configuration is 4.27 compared to a value of 6.72 for the pure cranked-wing model. This corresponds to a 36.5 percent decrease in maximum lift-to-drag ratio at Mach 4.0 when vehicle components are added to the pure waverider. When the nozzle surface pressures are corrected to freestream pressure, the maximum lift-drag ratio for the fully-integrated configuration becomes 4.56, which corresponds to a reduction of 32.2 percent when compared to that of the pure waverider model. The maximum lift-to-drag ratios of the fully-integrated configuration are lower than those for the pure waverider model at all Mach numbers studied and this value remains relatively constant across the Mach number range studied for the fully-integrated model.

The straight-wing fully-integrated configuration provides better aerodynamic performance than the cranked-wing fully-integrated configuration. The straight-wing model shows a maximum lift-to-drag ratio which is 3.82 percent higher than that of the cranked-wing configuration at the design Mach number of 4.0. This difference drops to 3 percent when the nozzle surface pressures are corrected to freestream pressure on both configurations. Both configurations have maximum lift-to-drag ratios above 4.0 which is comparable to conventional supersonic/ hypersonic shapes, but does not appear to provide a significant performance. Furthermore, the lift-to-drag ratios of the fully-integrated configurations are significantly lower than design-code predictions, as expected.

The fully-integrated configurations have better longitudinal and lateral-directional stability characteristics than the pure waverider configurations. Figures 6.18 and 6.19 show the pitching moment at Mach 4.0, the pitching moment curve slope and the yawing and rolling moment derivatives at each Mach number studied for the straight-wing and cranked-wing waveriders, respectively. A comparison of the fully-integrated and pure waverider configurations are shown on each plot. The fully-integrated configurations are more stable with respect to longitudinal motion than the pure waverider. Both fully-integrated configurations are still longitudinally unstable at all Mach numbers studied, but the cranked-wing model is more stable than the straight-wing configuration. The fully-integrated configurations are also more stable with respect to directional motion than the pure waverider models. Both the straight-wing and cranked-wing fully-integrated models are directionally stable at all Mach numbers studied, with the cranked-wing model providing more stability than the straight-wing model. Each fully-integrated model is also more laterally stable than the corresponding pure waverider configuration, with the cranked-wing configuration providing better stability than the straight-wing model.

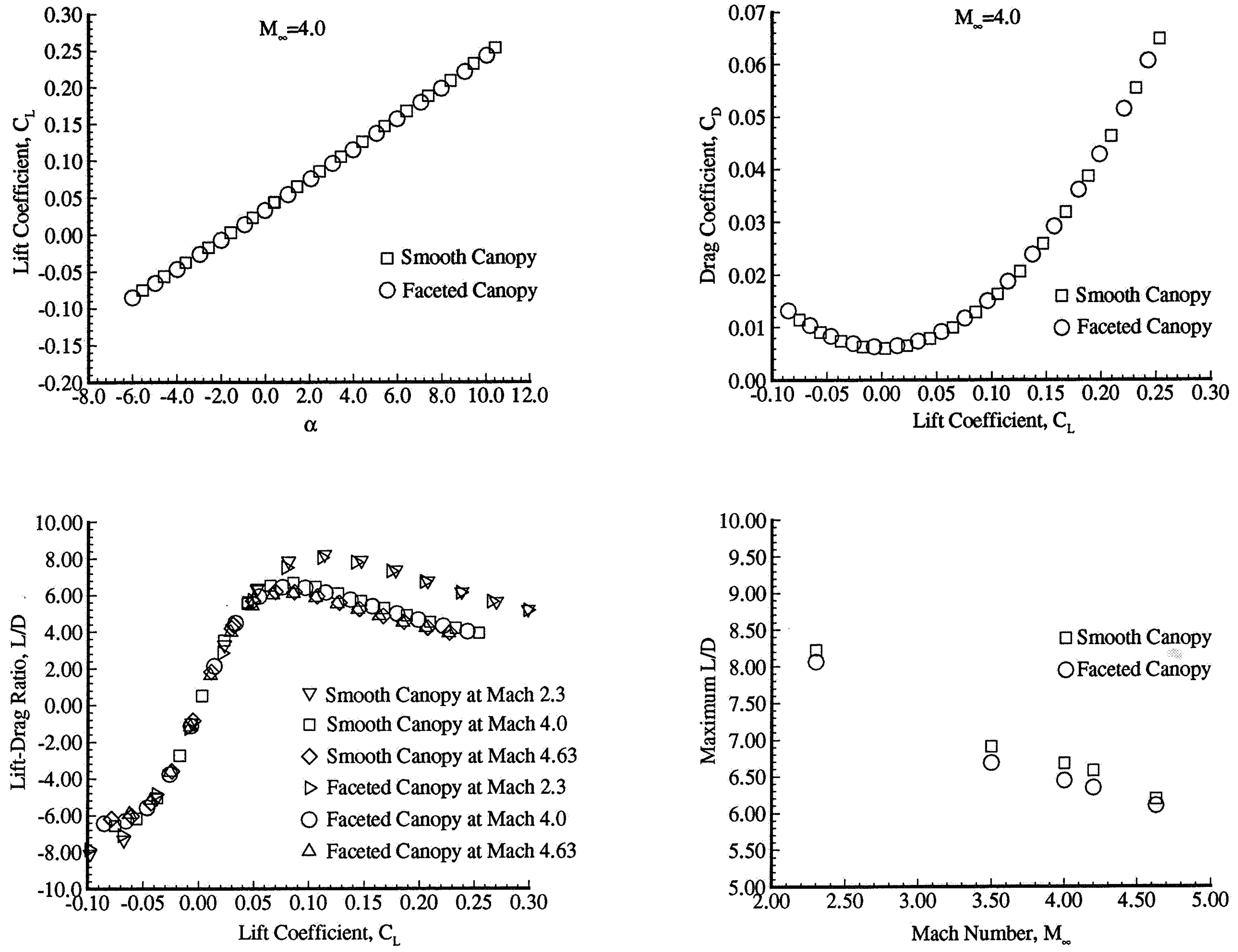

Figure 6.1. Effect of canopy on aerodynamic performance of straight-wing configuration.

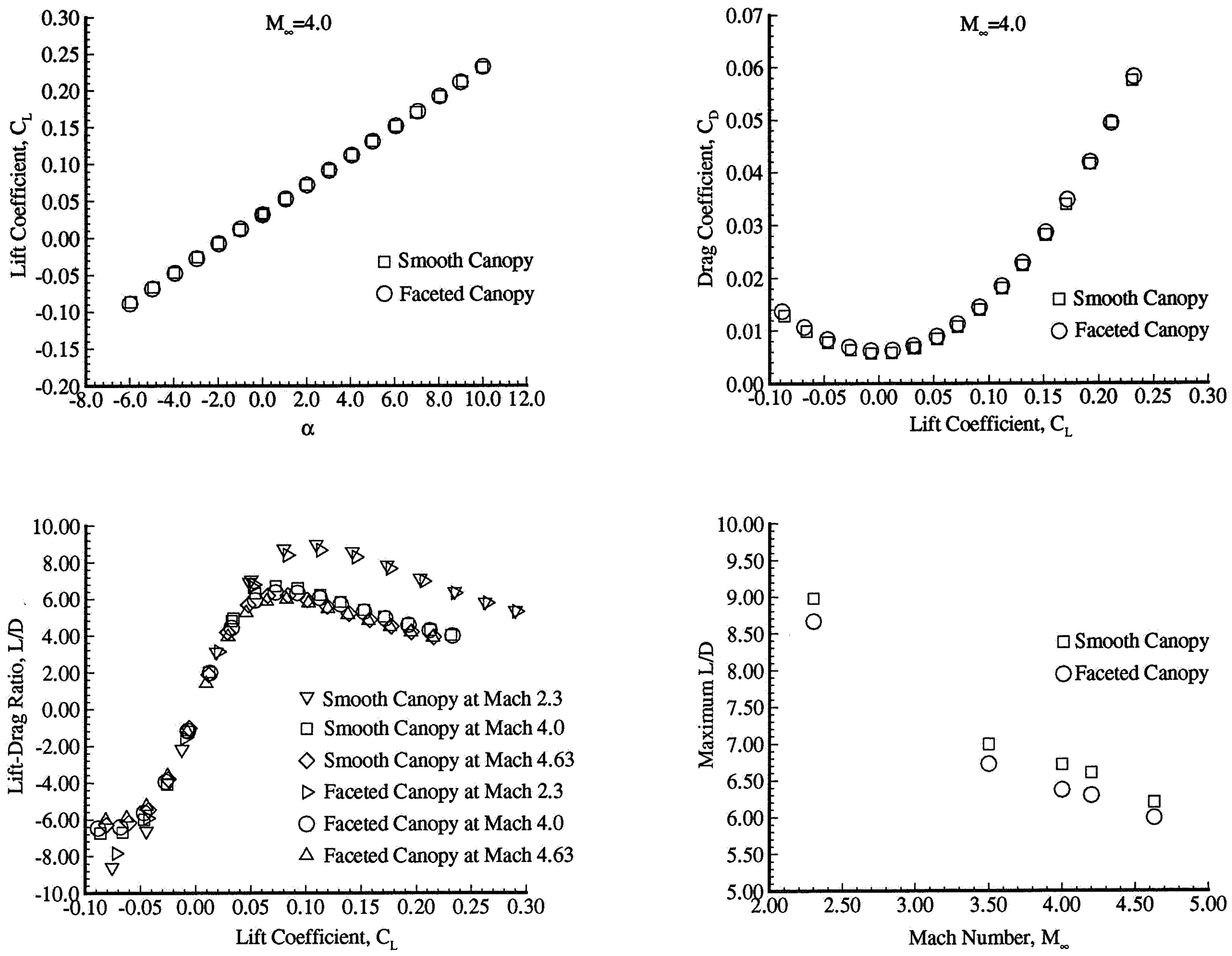

Figure 6.2. Effect of canopy on aerodynamic performance of cranked-wing configuration.

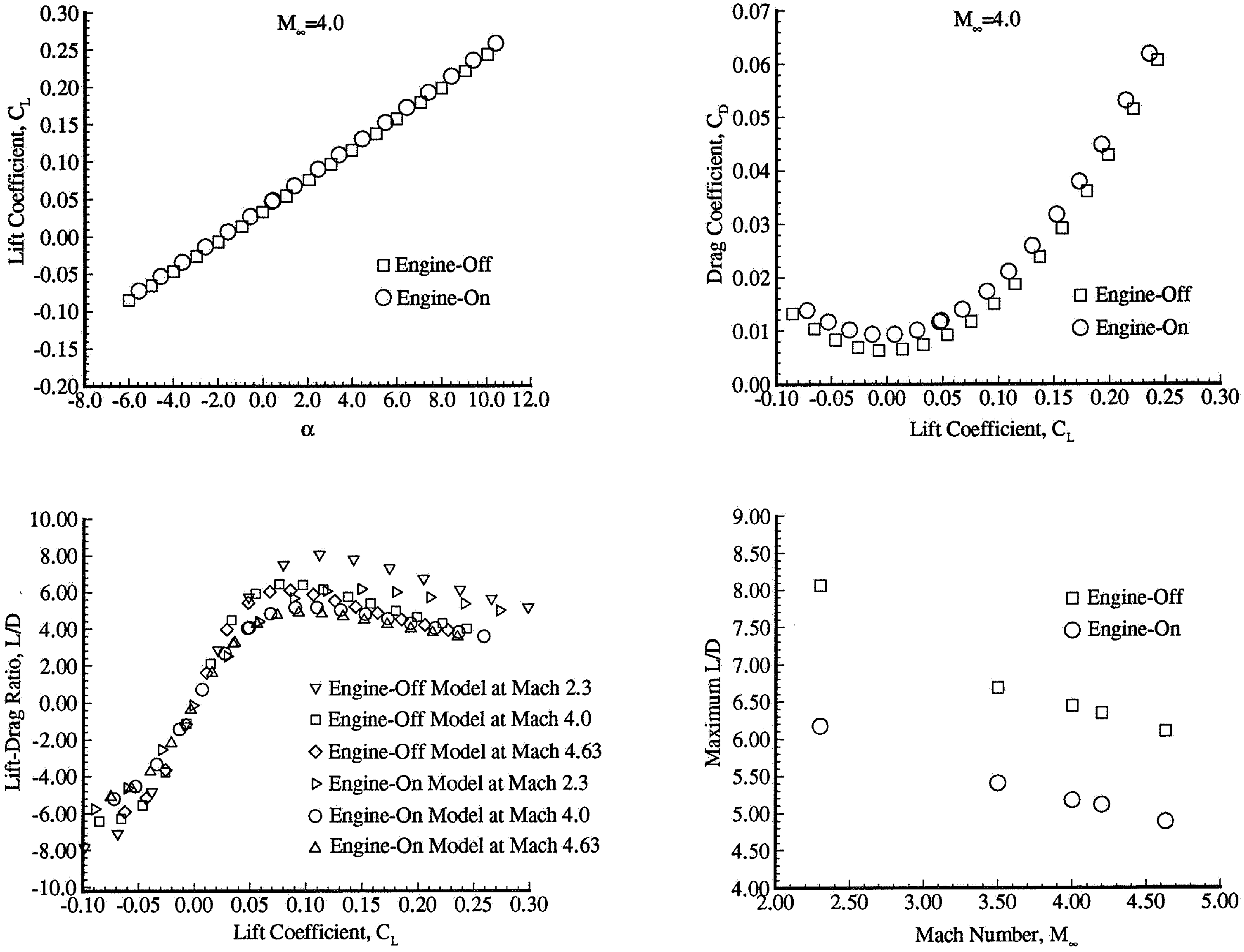

Figure 6.3. Effect of adding engine components on aerodynamic performance of straight-wing configuration.

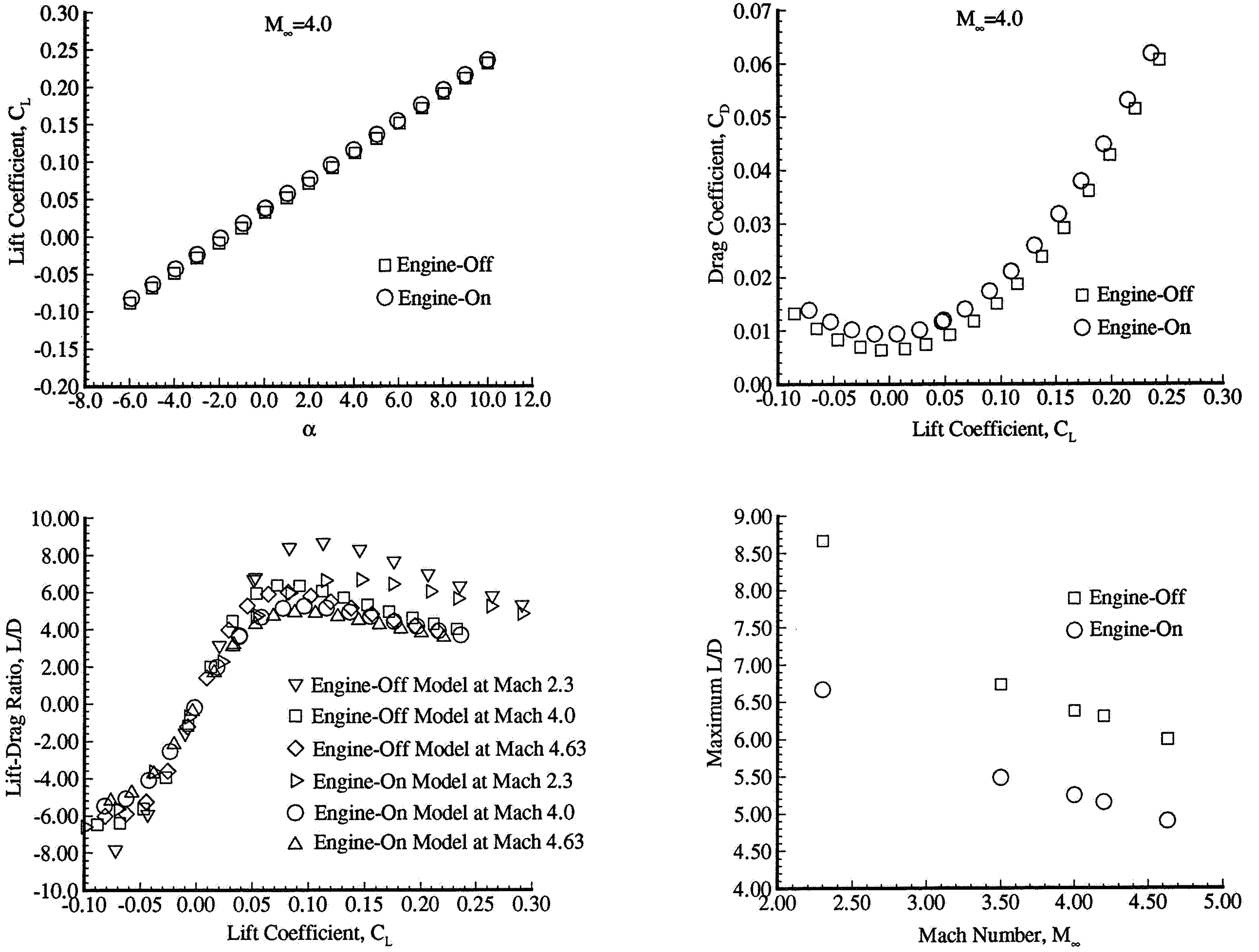

Figure 6.4. Effect of adding engine components on aerodynamic performance of cranked-wing configuration.

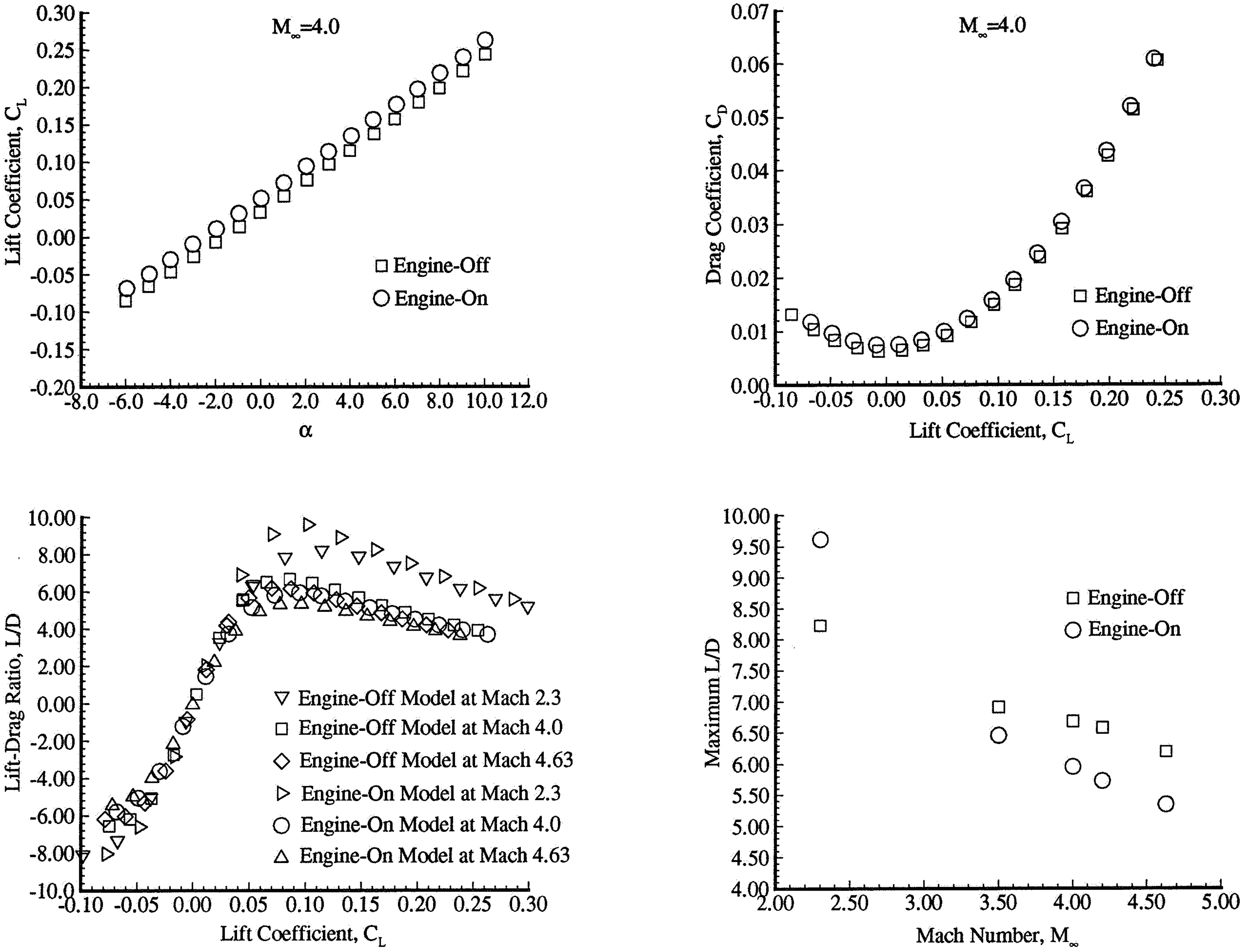

Figure 6.5. Effect of adding engine components on aerodynamic performance of straight-wing configuration with nozzle surface pressures corrected to freestream pressure.

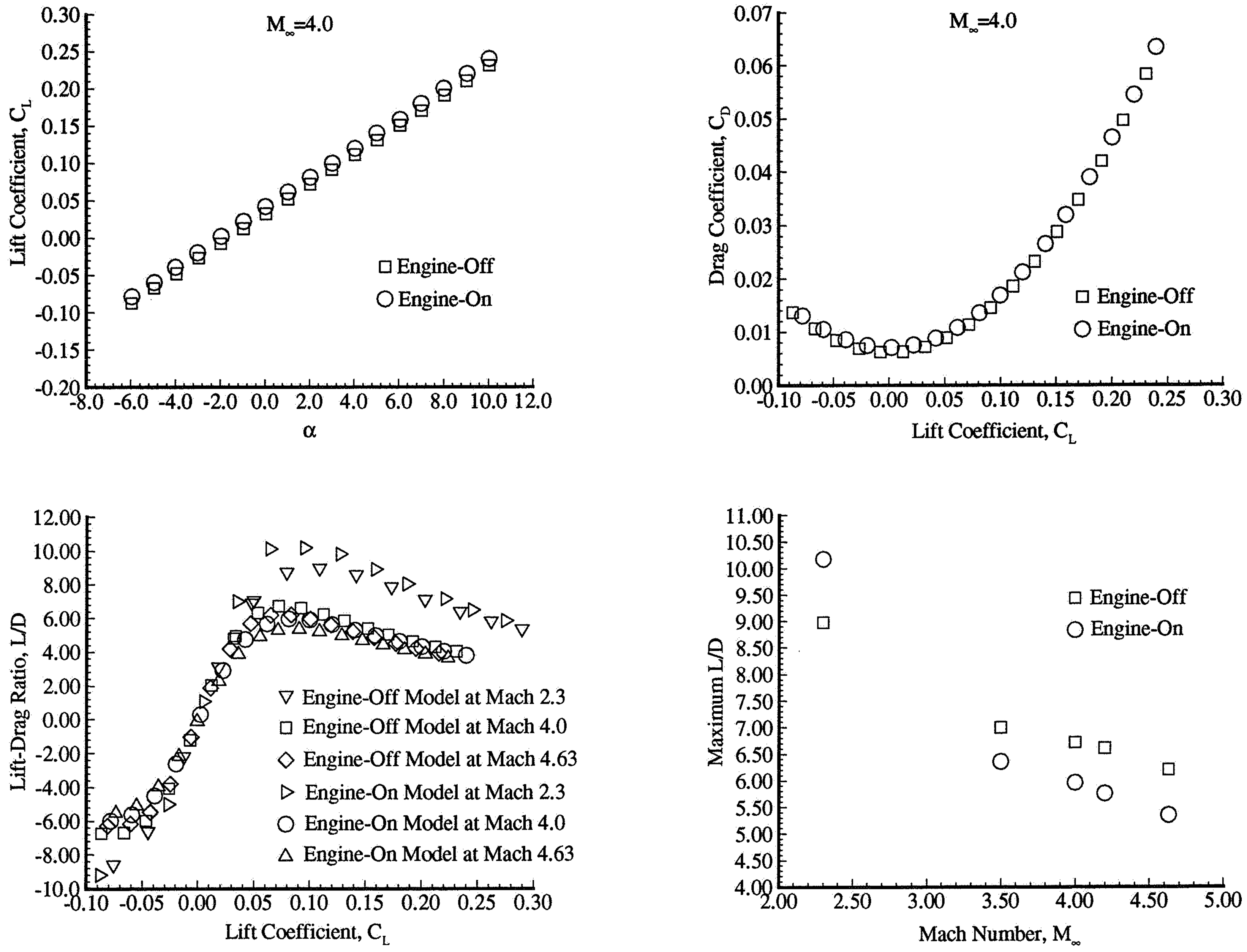

Figure 6.6. Effect of adding engine components on aerodynamic performance of cranked -wing configuration with nozzle surface pressures corrected to freestream pressure.

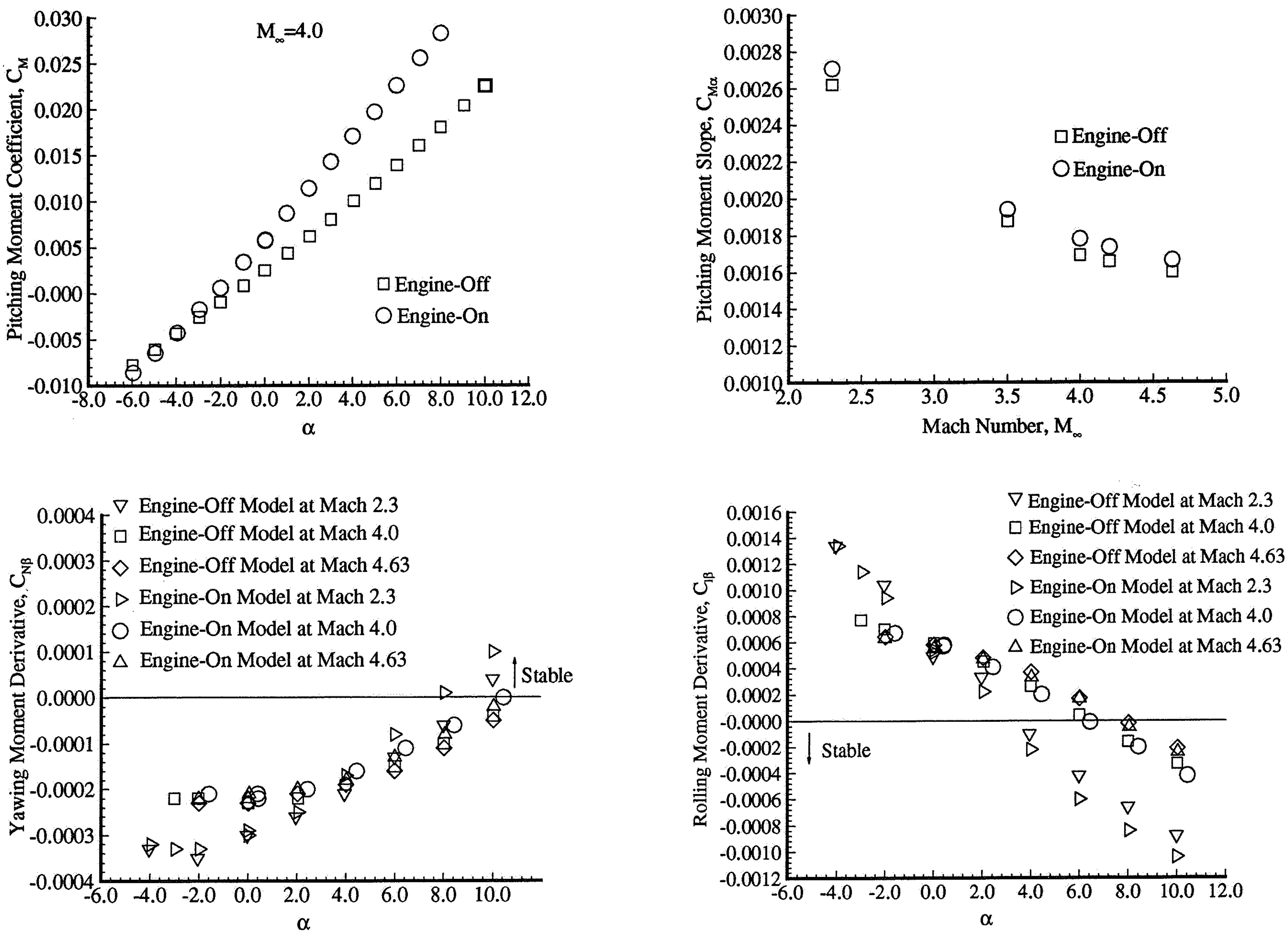

Figure 6.7. Effect of adding engine components on longitudinal and lateral-directional stability of straight-wing configuration.

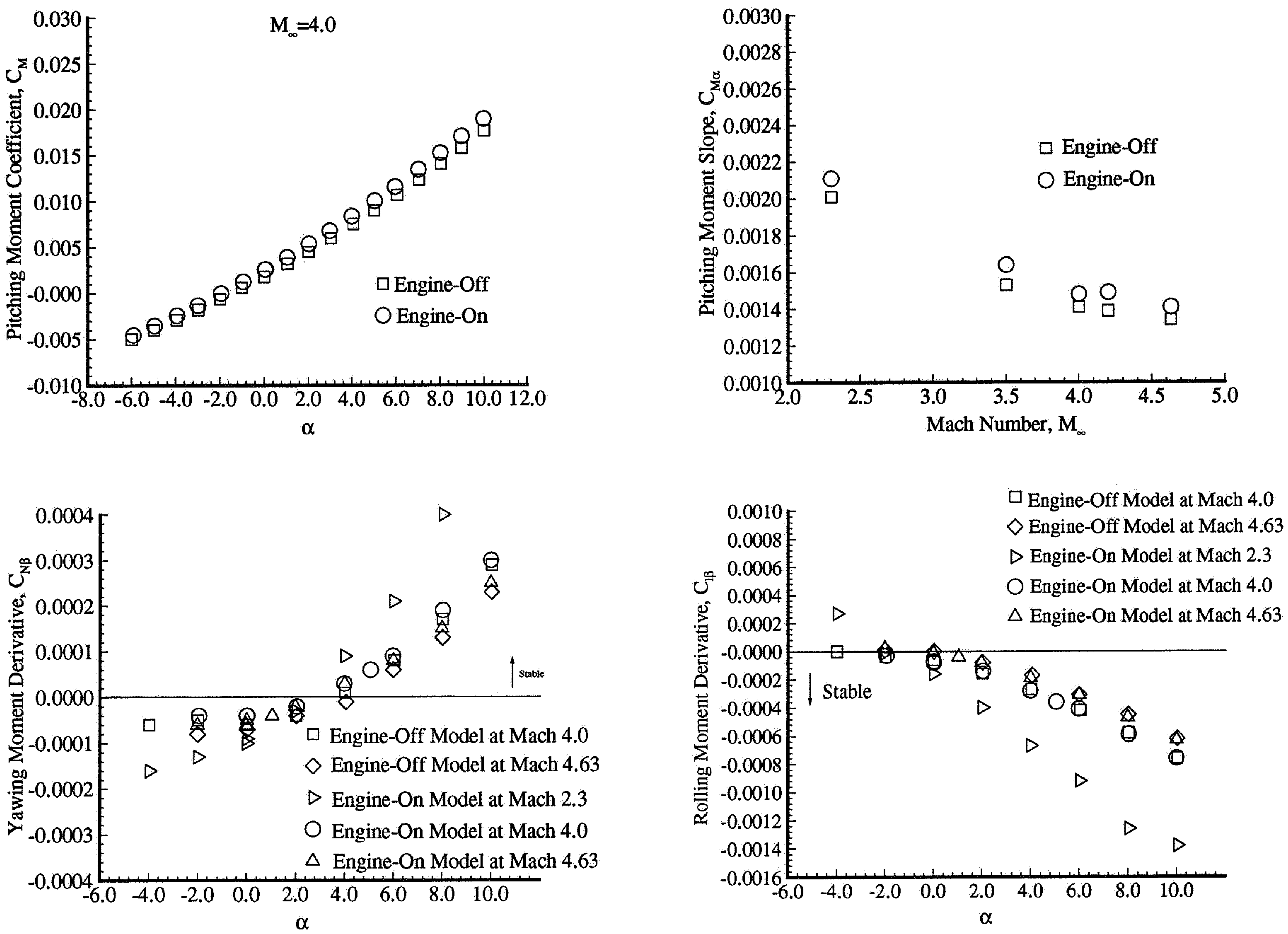

Figure 6.8. Effect of adding engine components on longitudinal and lateral-directional stability of cranked-wing configuration.

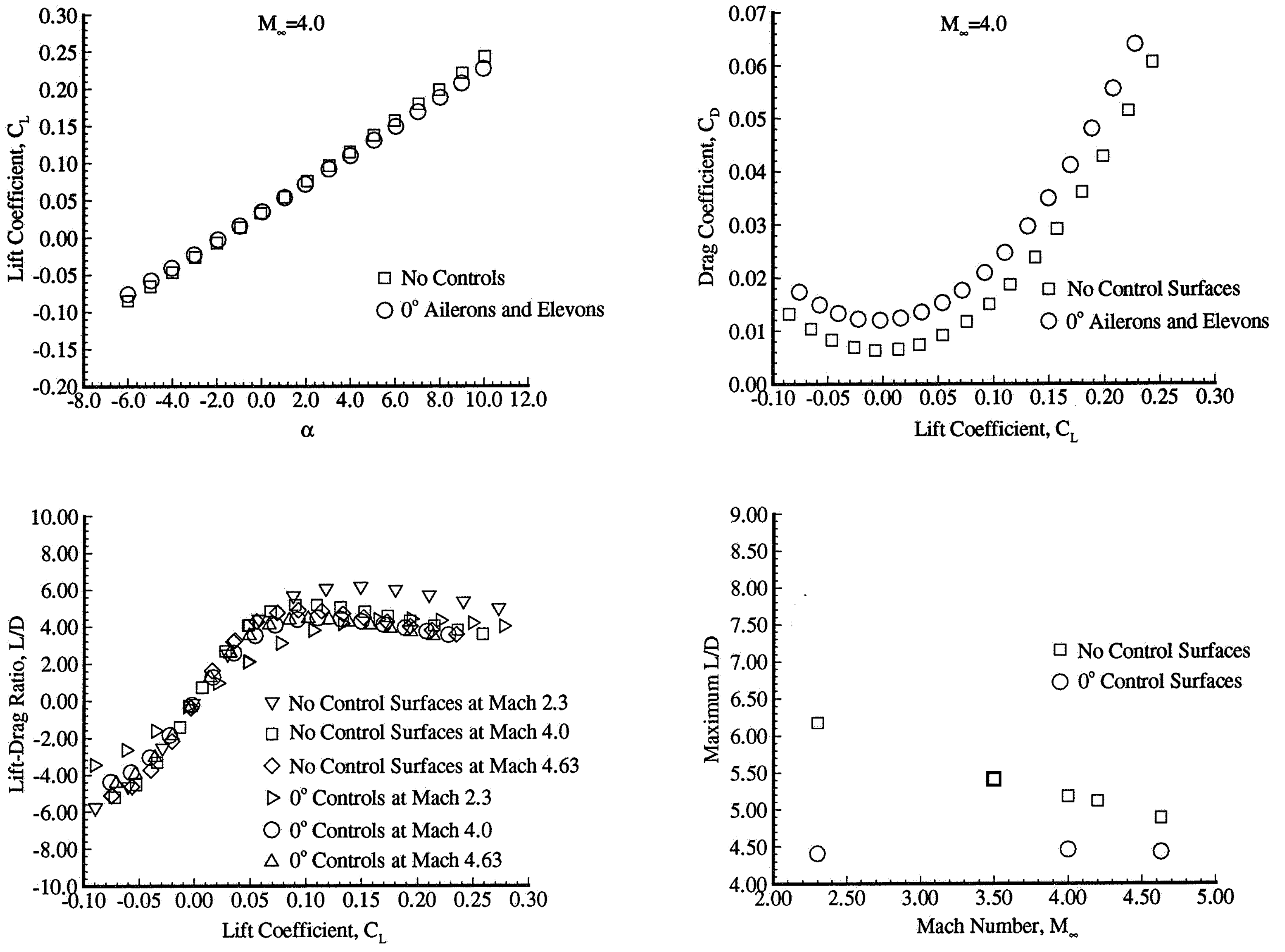

Figure 6.9. Effect of adding 0^{o} control surfaces on aerodynamic performance of straight-wing configuration.

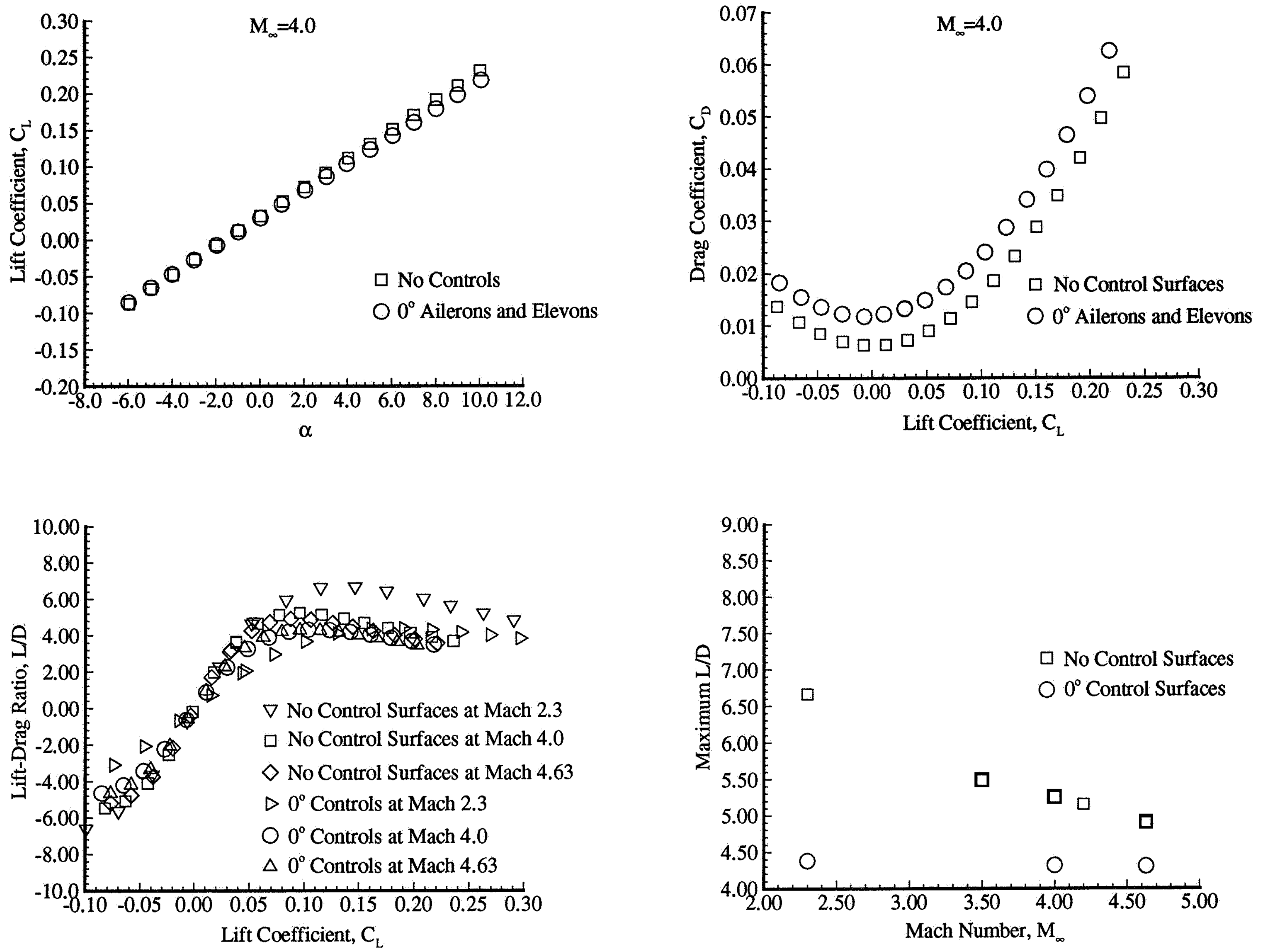

Figure 6.10. Effect of adding 0° control aurfaces on aerodynamic performance of cranked-wing configuration.

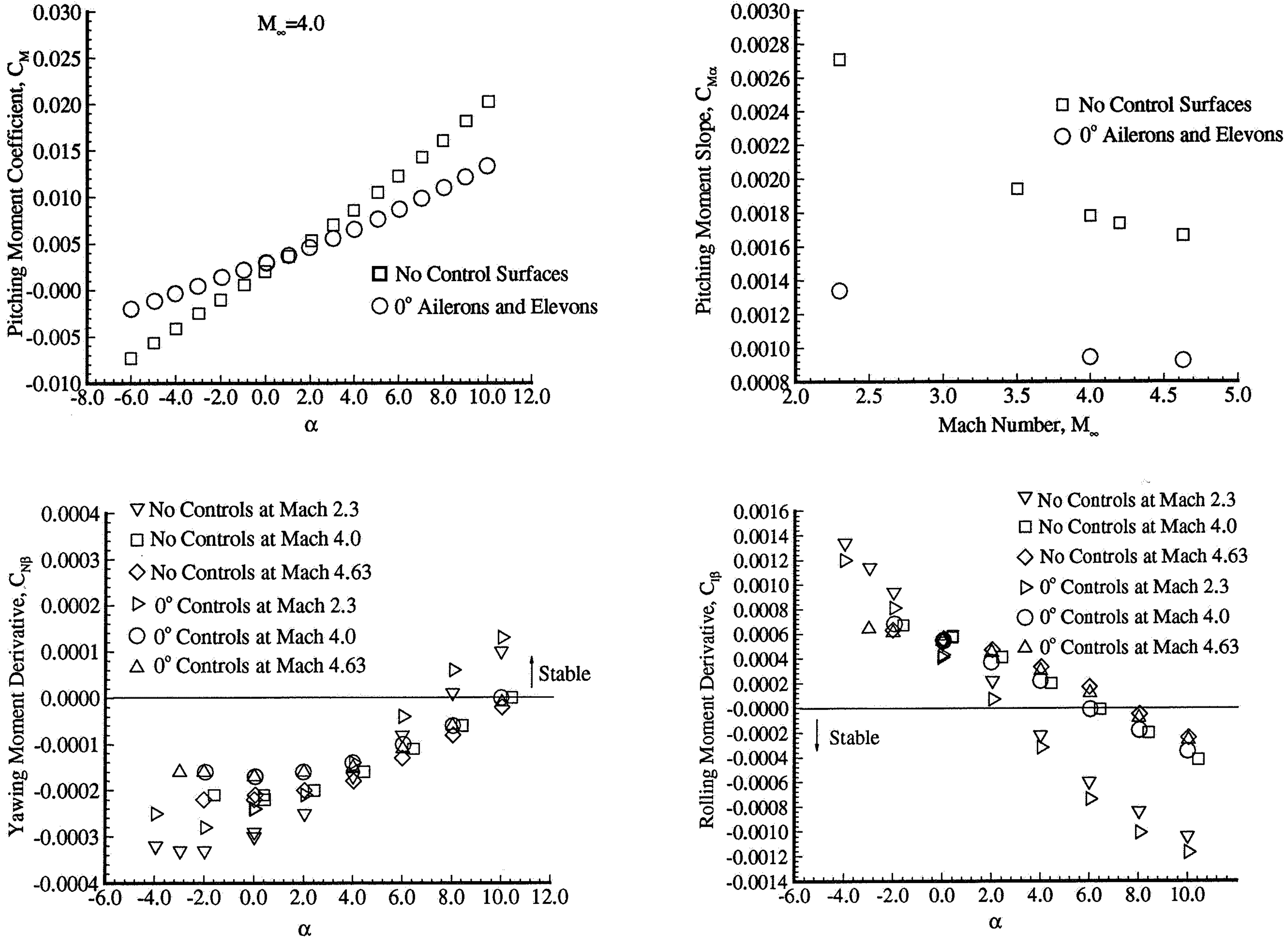

Figure 6.11. Effect of adding 0° control surfaces on longitudinal and lateral-directional stability of straight-wing configuration.

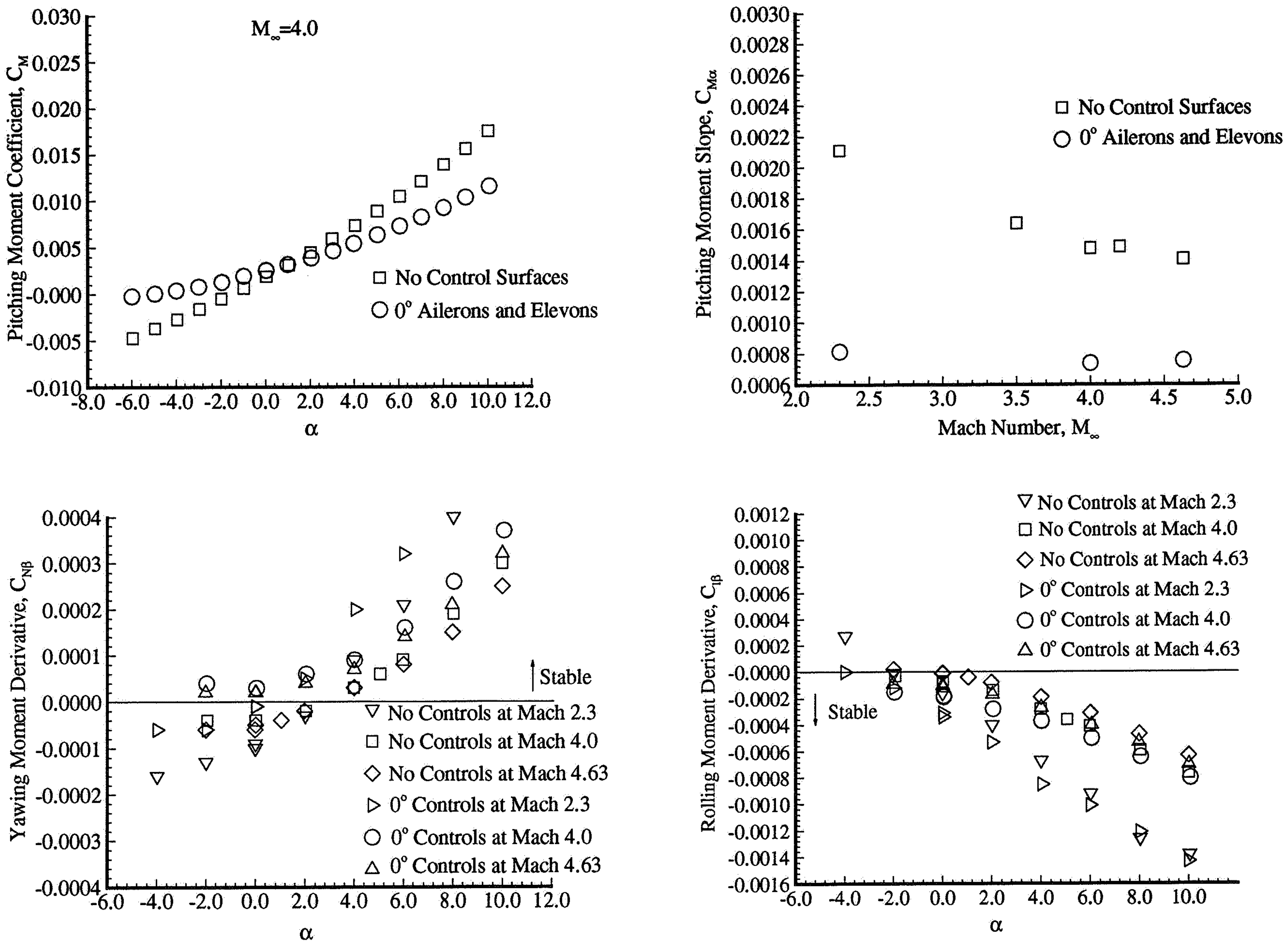

Figure 6.12. Effect of adding 0° control surfaces on longitudinal and lateral-directional stability of cranked-wing configuration.

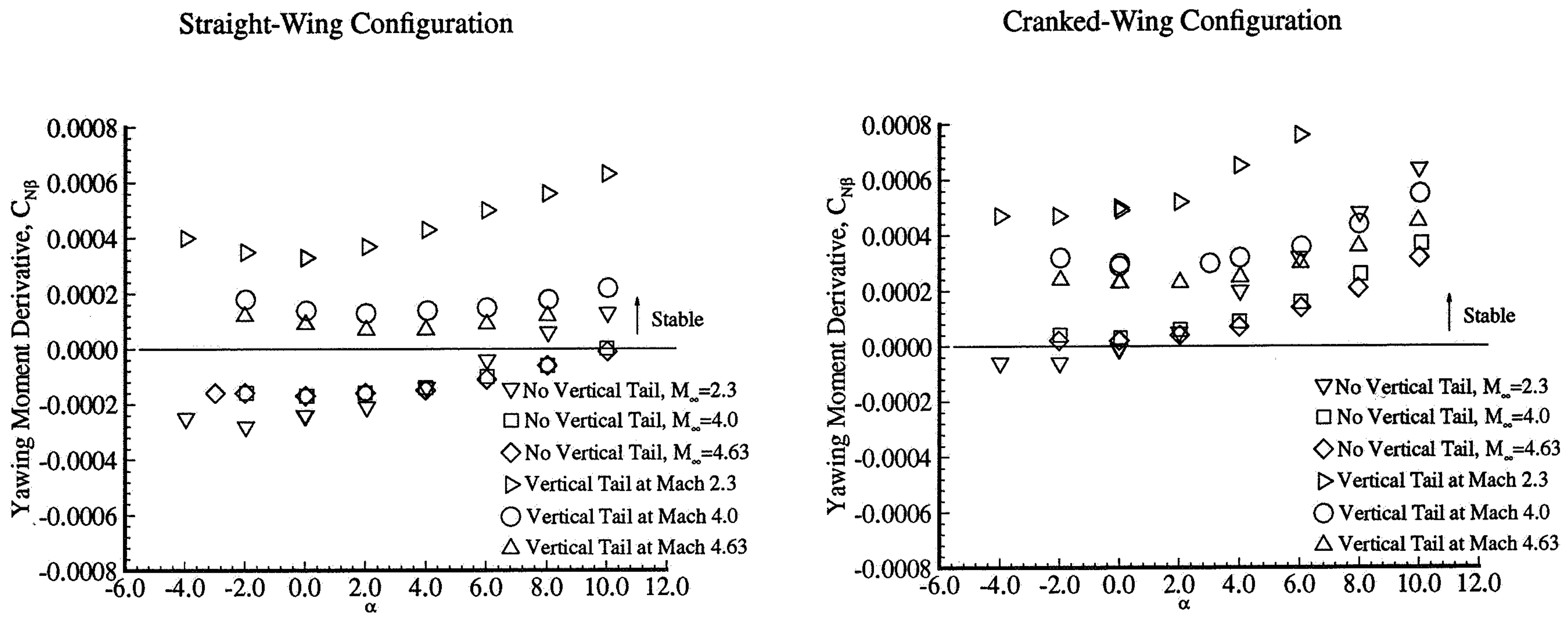
Straight-Wing Configuration

Cranked-Wing Configuration

Figure 6.13. Effect of vertical tail on directional stability of straight-wing and cranked-wing configurations.

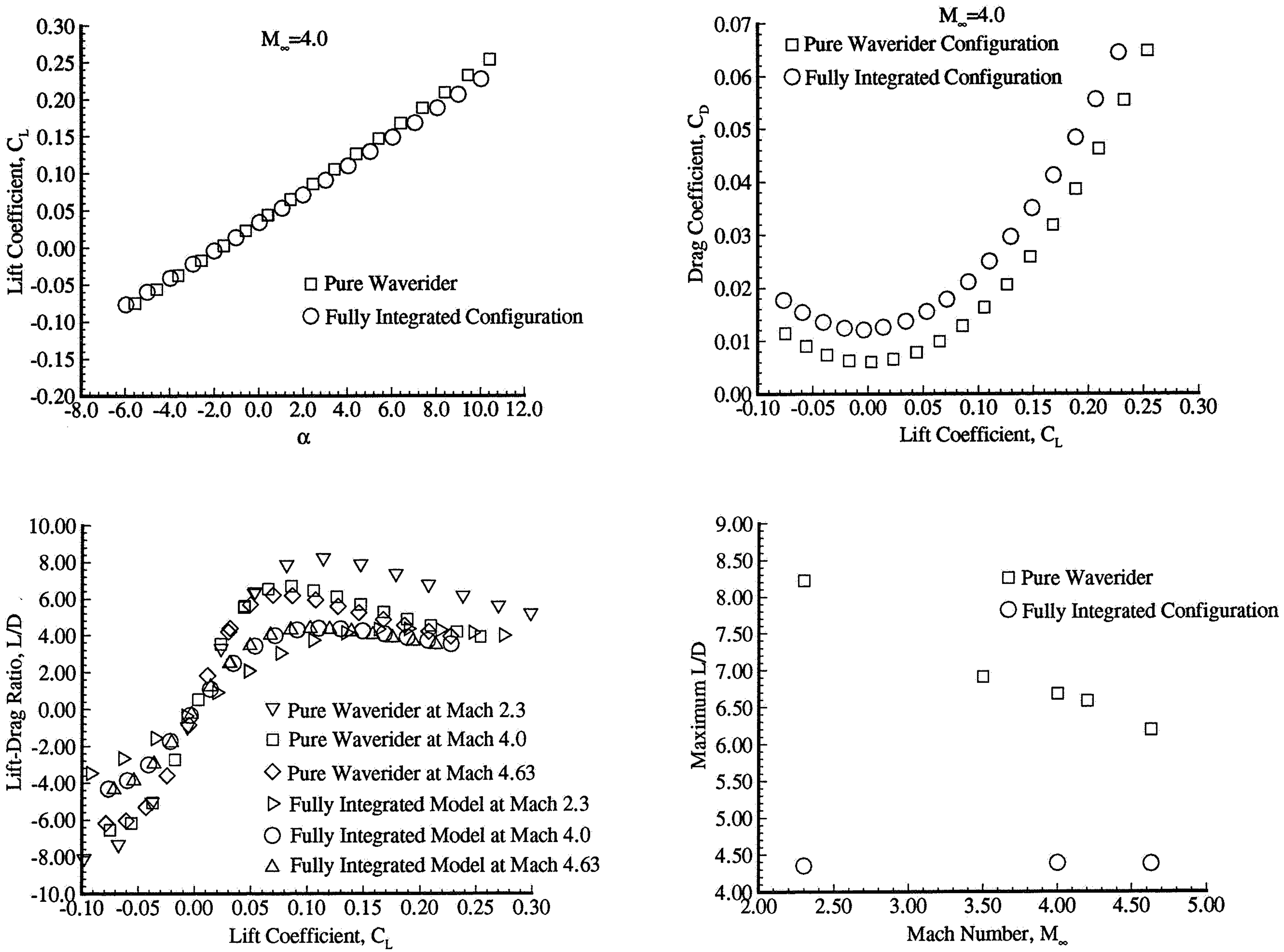

Figure 6.14. Comparison of aerodynamic performance of pure straight-wing waverider configuration and fully-integrated straight-wing configuration.

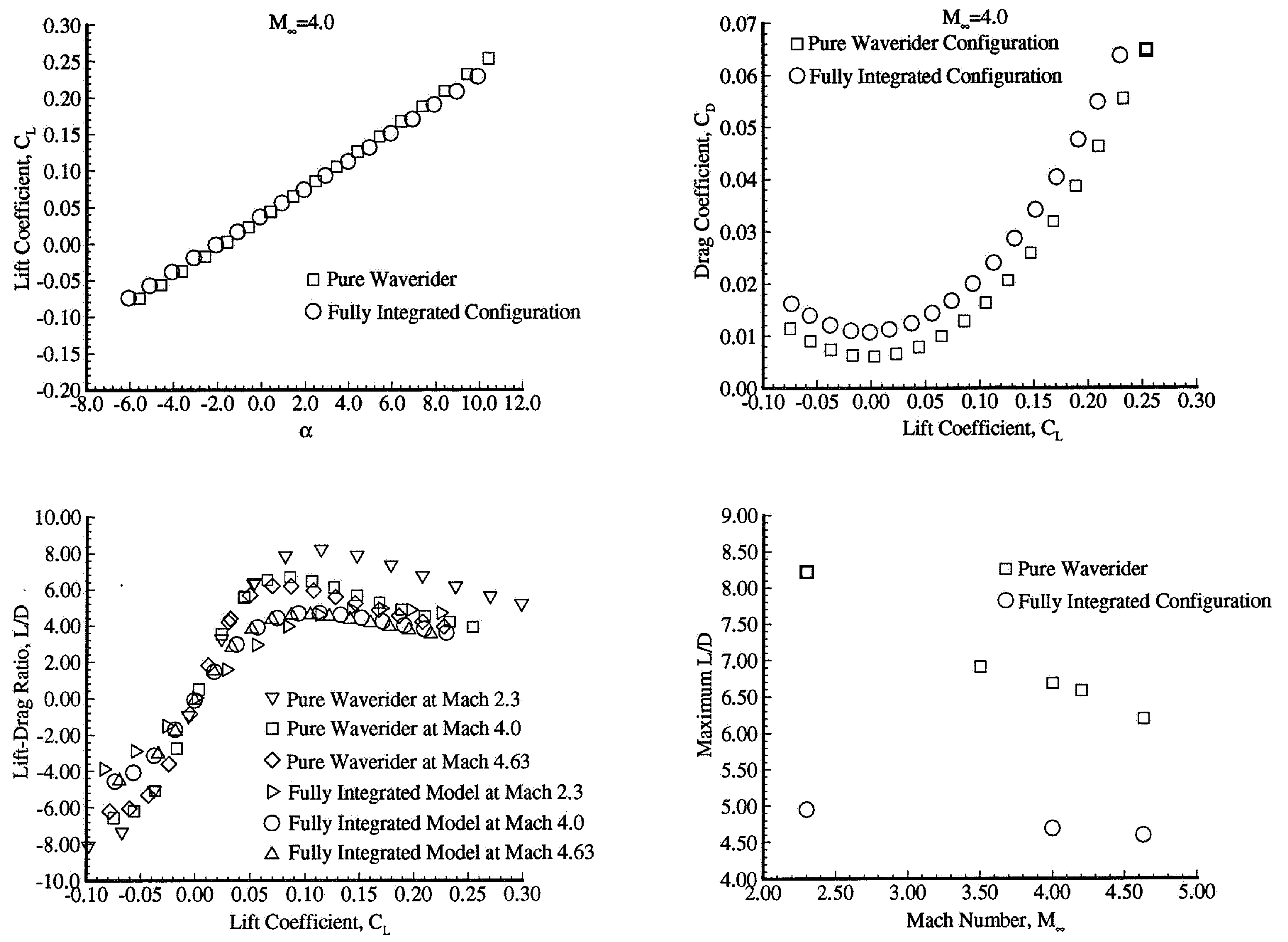

Figure 6.15. Comparison of aerodynamic performance of pure straight-wing waverider configuration and fully-integrated straight-wing configuration with nozzle surface pressures corrected to freestream pressure.

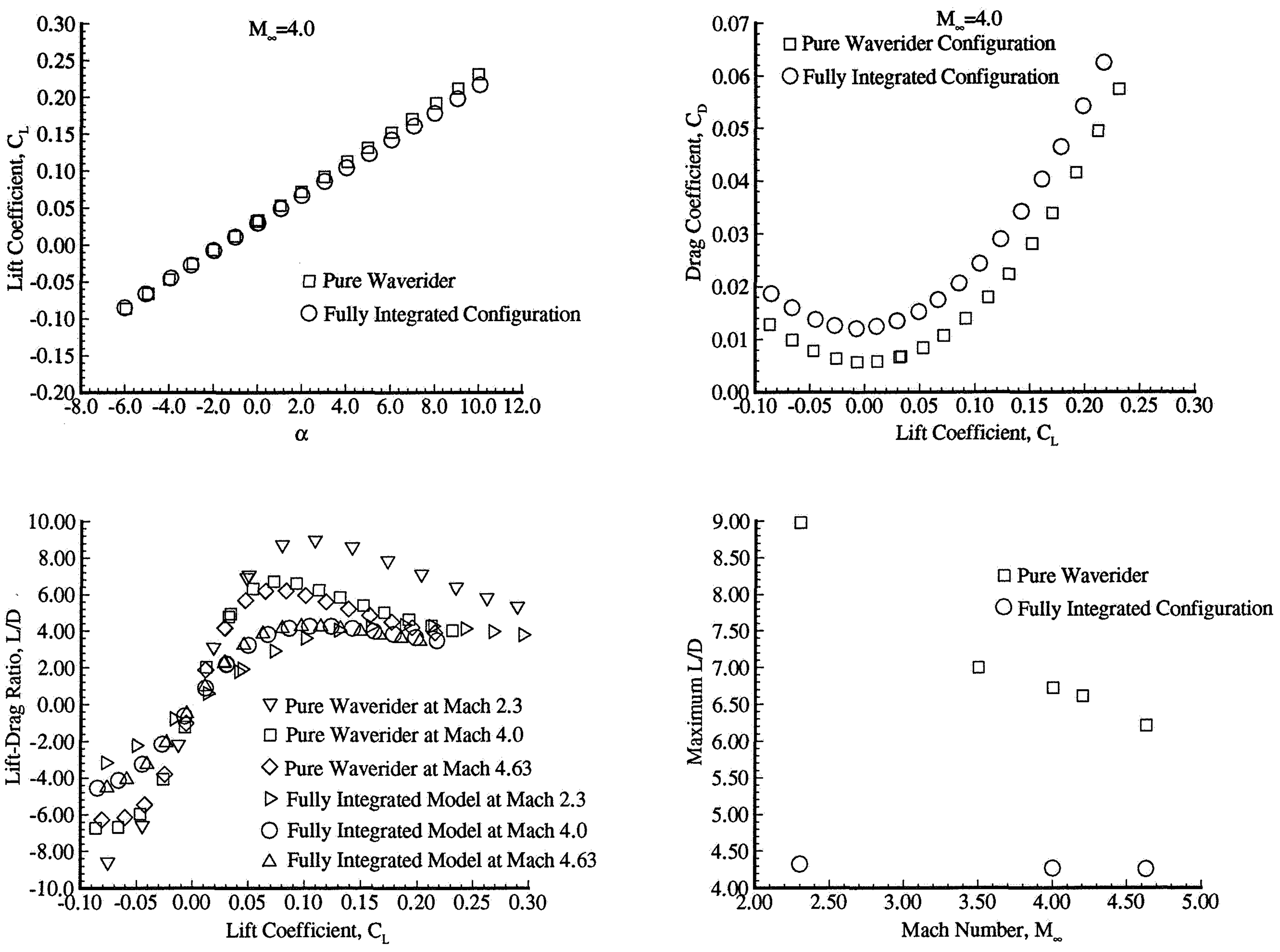

Figure 6.16. Comparison of aerodynamic performance of pure cranked-wing waverider configuration and fully-integrated cranked-wing configuration.

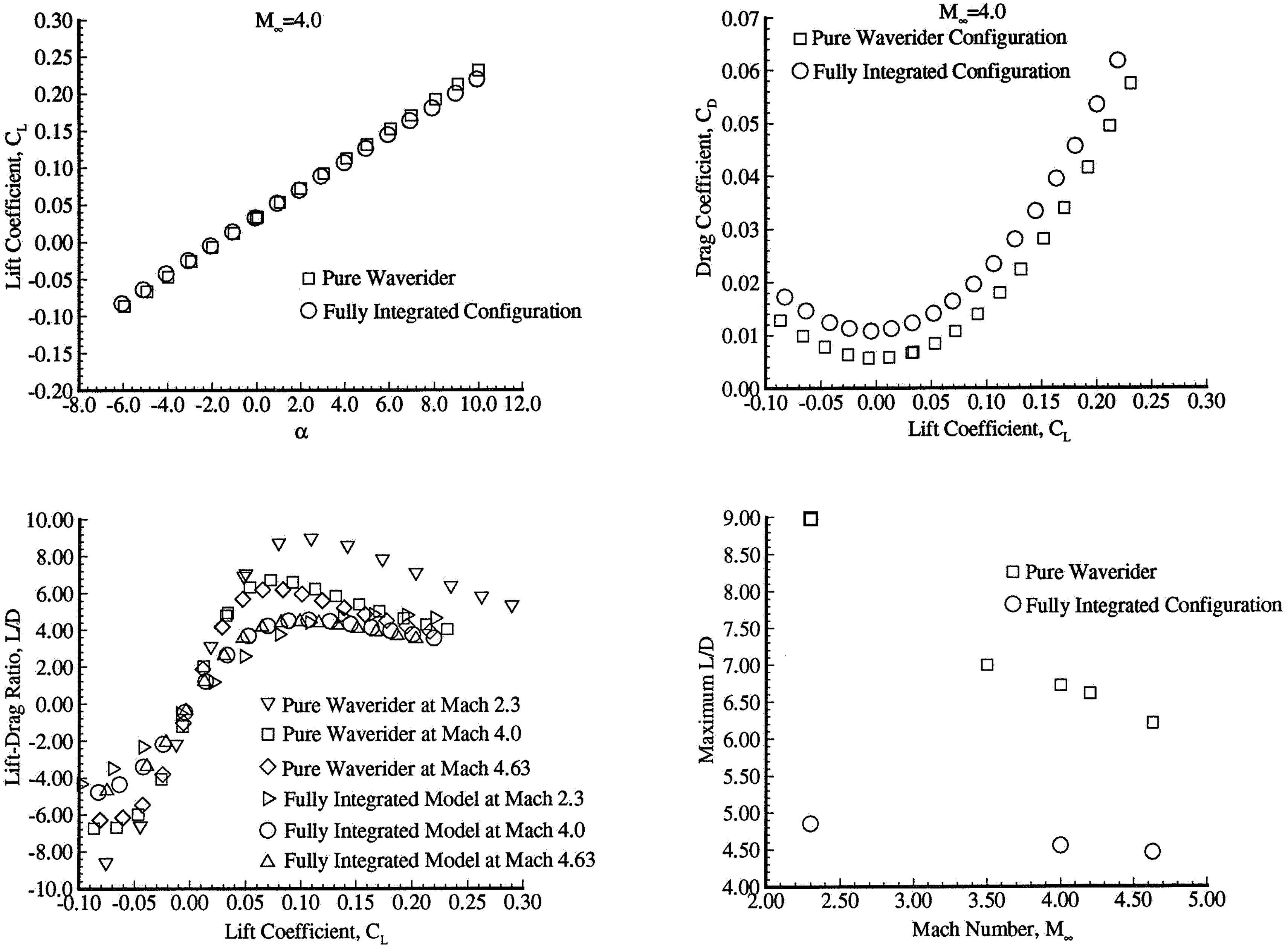

Figure 6.17. Comparison of aerodynamic performance of pure cranked-wing waverider configuration and fully-integrated cranked - wing configuration with nozzle surface pressures corrected to freestream pressure.

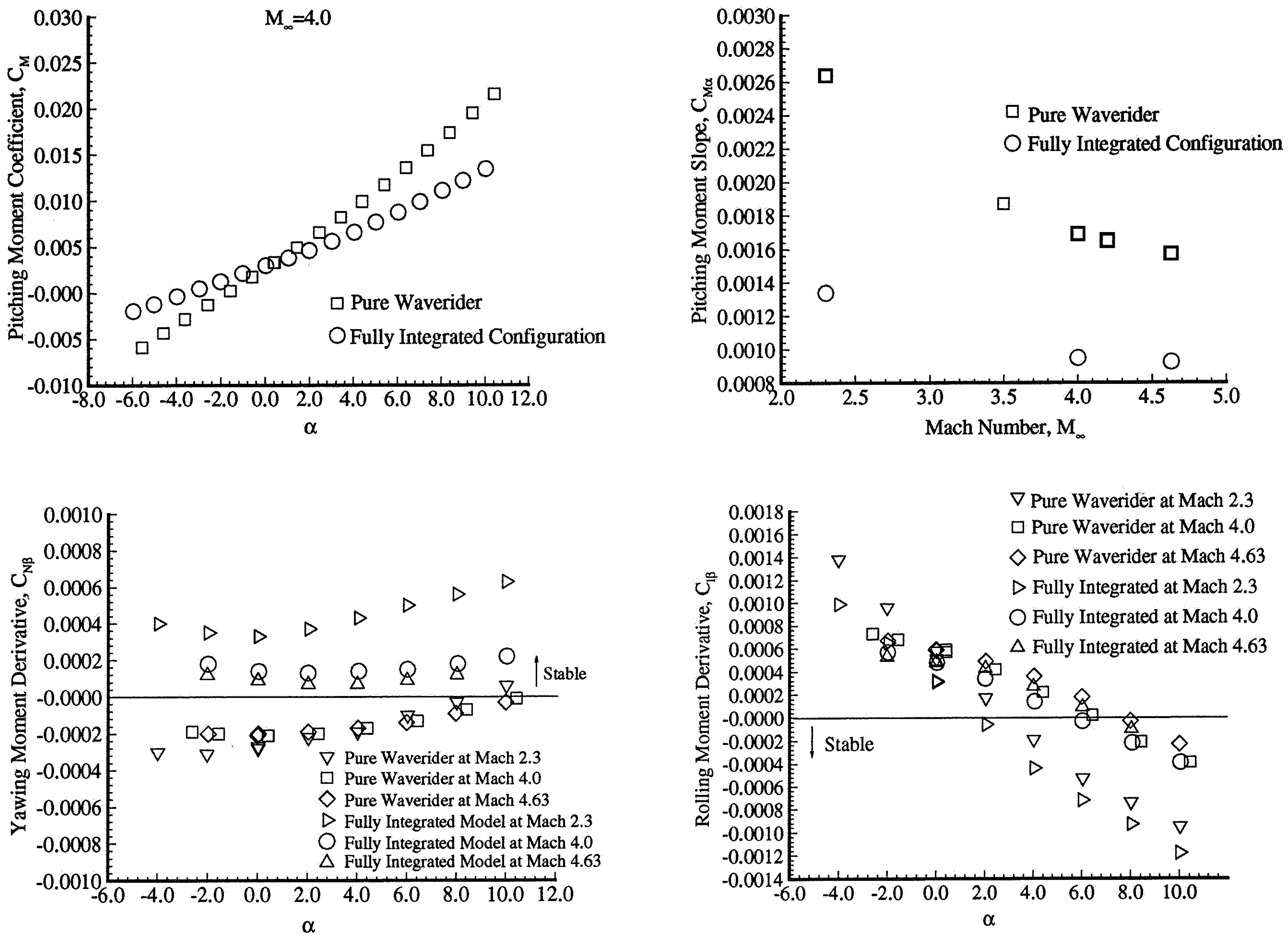

Figure 6.18. Comparison of longitudinal and lateral-directional stability characteristics of pure straight-wing waverider and fully-integrated straight-wing configuration.

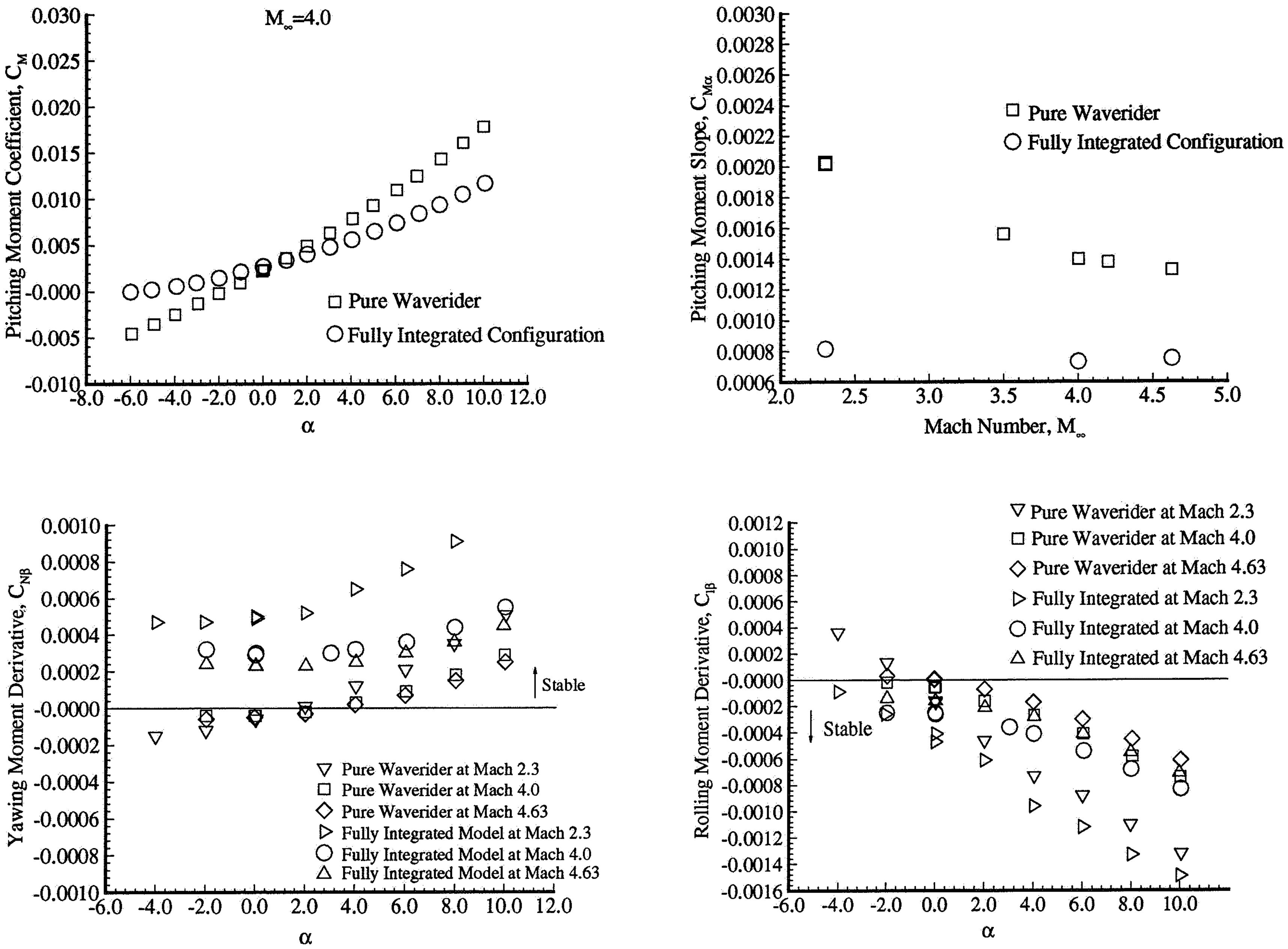

Figure 6.19. Comparison of longitudinal and lateral-directionsl stability characteristics of pure cranked-wing waverider and fully-integrated cranked-wing configuration.

CHAPTER 7
CONCLUSIONS AND RECOMENDATIONS

7.0 Summary

The objectives of this study were to create an aerodynamic data base for waverider-derived hypersonic cruise configurations, to examine the effects of various vehicle components on waverider aerodynamic performance and stability and to quantify the differences in performance and stability between the fully-integrated configurations and the baseline waverider shapes. These objectives were accomplished by obtaining experimental force and moment data as well as flow visualization data for two waverider models, a straight-wing and a cranked-wing waverider. Data were obtained for various configurations with and without integrated vehicle components, up to and including the fully-integrated waverider-derived vehicles. Limited computational predictions were also obtained for the "pure" waverider configurations, which have no engine components or control surfaces. The waverider flow-field characteristics were examined from CFD solutions, as well as from schlieren and vapor-screen photographs of the models. The effects of individual vehicle components on waverider performance were isolated by comparing experimental force and moment data for various configurations. Finally, experimental data for the aerodynamic performance and stability characteristics of the fully-integrated configurations were compared with data from the pure waverider models. Future research in this area should include improvements in design methods, obtaining experimental data and computational predictions in various speed regimes and powered exhaust simulation testing to evaluate the propulsion/airframe integration (PAI) characteristics of waverider-derived models.

7.1 Waverider Flow-Field Characteristics and Performance Analysis

Comparisons of CFD solutions of the straight-wing design-code shape and the straight-wing pure waverider model at the design Mach number of 4.0 showed that the modifications made to the design-code waverider shape in order to facilitate fabrication of the wind tunnel model did not have a significant effect on the aerodynamic performance or on the flow-field characteristics of the waverider shape. The modified waverider shape maintained advantages in aerodynamic performance and propulsion/airframe integration (PAI) characteristics. CFD predictions and laser vapor-screen photographs of the straight-wing and cranked-wing pure waverider models confirmed the shock attachment/detachment characteristics of each configuration. The shock was slightly detached from the outer leading edge at the design Mach number of 4.0 and 0^o angle of attack. This detachment distance exists because of boundary layer displacement effects as well as blunt leading-edge effects. The design code assumes an infinitely sharp leading edge and does not account for the presence of a boundary layer. The CFD predictions and flow visualization data also showed that the shock was detached from the leading edge at angles of attack of -6^o and 8^o at Mach 4.0 and that a large detachment distance was present at Mach 2.3 and 0^o angle of attack for both the straight and cranked waverider models.

The aerodynamic performance and stability of the two pure waverider models were examined using experimental force and moment data as well as integrated pressure and skin-friction predictions from CFD solutions. The results showed that:

1. The cranked-wing pure waverider model exhibited slightly better aerodynamic performance at the design Mach number than the straight-wing model.
2. The maximum lift-to-drag ratios observed experimentally were lower than the design-code predictions, as expected. This was due to a loss of lift and increase in drag caused by the shock not being perfectly attached as well as to a loss of lift from the lower-surface expansion and an increase in drag from the additional volume added to the upper surface. The maximum lift-to-drag ratio for each configuration occurs at an angle of attack above 0^o.
3. There was no significant performance degradation of the pure waverider configurations at off-design Mach numbers.
4. Both pure waverider models were longitudinally unstable at all Mach numbers studied and the cranked-wing pure waverider configuration showed better lateral-directional stability characteristics than the straight-wing pure waverider

configuration, as expected.

7.2 Component Build-Up Effects

Component build-up effects on the aerodynamic performance and stability of both waverider shapes were examined by comparing experimental force and moment data. This analysis showed that:

1. The primary effect of adding the faceted canopy was to increase the drag of the configuration, thereby resulting in a slight degradation in aerodynamic performance.
2. The effect of adding the engine package was to significantly increase the drag and degrade the aerodynamic performance. A slight increase in lift was also observed, caused by the inlet compression surface. The performance degradation observed was less severe when the nozzle surface pressures were corrected to assume freestream pressure acting at the nozzle surface. The data presented with nozzle surface pressure corrected show the effects on performance without any propulsive component.
3. The addition of engine components caused a slight destabilizing shift in longitudinal stability and slightly enhanced the lateral-directional stability of both the straight-wing and cranked-wing configurations.
4. The addition of control surfaces significantly degraded the aerodynamic performance of each configuration. Much of the performance degradation was caused by a large reduction in the base area when control surfaces were added to close the blunt base to a sharp trailing edge. The data for all of the configurations were presented with the base pressures corrected to freestream pressure in order to eliminate the effect of the base in performance data. These results indicate that additional consideration should be applied to the design of control surfaces and aftbody closure in waverider-based hypersonic cruise configurations.

5. The addition of control surfaces caused a stabilizing shift in pitching moment curve slope and enhanced the lateral-directional stability of both configurations. However, the controls-on configurations were longitudinally unstable at all Mach numbers studied.

7.3 Evaluation of Fully-Integrated Configuration

The aerodynamic performance of both fully-integrated waverider models was significantly degraded from that of the pure waverider shapes. The straight-wing fully-integrated configuration provided slightly better aerodynamic performance than the cranked-wing fully-integrated model. The maximum lift-to-drag ratios at Mach 4.0 are 4.69 for the straight-wing model and 4.27 for the cranked-wing model. By comparing these values to the "L/D Barrier" shown in figure 2.2 and discussed in chapter 2, it is observed that the fully-integrated waverider-derived configurations no longer provide a significant performance advantage over conventional hypersonic shapes. However, the performance is not significantly worse than conventional shapes and the waverider flow field still provides significant advantages for air-breathing propulsion systems integration. Furthermore, the results of this study have identified areas which could be improved, such as control surfaces, aftbody closure and propulsion system design. Improvements in these areas could enhance the performance of waverider-derived configurations. Improvements in waverider design methods, such as accounting for the change in effective surface slope due to boundary layers, including blunt leading edges in optimization routines and using different generating flow-field bodies, could also enhance the performance of pure waverider shapes.

The fully-integrated configurations exhibited better longitudinal and lateral-directional stability characteristics than the pure waverider shapes. However, both fully-integrated configurations were unstable with respect to longitudinal motion. The control surface design should be revised to improve the longitudinal stability of the vehicle. The addition of a functioning propulsion system will also enhance the longitudinal stability of waverider-derived vehicles. Additionally, the shift in static margin could be controlled using fuel shift for this type of vehicle in order to provide at least neutral stability over the angle-of-attack range. Both configurations were stable with respect to lateral-directional motion. The cranked-wing configuration provided better lateral-directional stability characteristics than the straight-wing waverider configurations.

7.4 Recommendations For Future Research

Future research in the development of waverider-derived hypersonic cruise vehicles should center on evaluation of control surface effectiveness, improvements in design methods, obtaining aerodynamic data and computational predictions across all speed regimes and powered exhaust simulation testing. Specifically, the following studies are recommended:

1. The effectiveness of the current control surface design should be evaluated using experimental data obtained for aileron-deflected and elevon-deflected configurations. A re-design of the control surfaces may be necessary to ensure longitudinal stability and to minimize the aerodynamic performance degradation observed in the current study.
2. Computational solutions of the fully-integrated configurations should be obtained in order to make comparisons with experimental force and moment data and to provide additional information on the flow-field characteristics of each configurations.
3. The design method should be improved to account for the displacement thickness of the boundary layer. This may result in performance improvements by decreasing the shock detachment distance observed at the design Mach number.
4. Blunt leading edges should be accounted for in future optimized designs. Leading edge shape and heat transfer to the leading edge have been examined in previous studies,[20] and an updated version of the design code used in the current study has been developed which allows for the design of waveriders with blunt leading edges.[21]
5. Studies examining the performance of waveriders designed from flow fields other

than conical ones should be conducted. Preliminary research in this area has shown that it is possible to generate waveriders from different generating flow fields, resulting in improved PAI characteristics and greater volume.[22] Improvements in aerodynamic performance may also be possible.[5]

6. Component build-up, aerodynamic performance and flow-field characteristics should be examined at subsonic, transonic and low supersonic speeds. Experimental data and computational solutions should be obtained. The advantages offered by the cranked-wing shape in subsonic performance should be validated.
7. Additional studies in PAI methods and design of propulsion systems for waverider-derived hypersonic cruise vehicles should be conducted.
8. Powered exhaust simulation studies should be conducted to examine the effects of a functioning propulsion system on the external aerodynamics of waverider-derived models. Data should be obtained at subsonic, transonic, supersonic and hypersonic speeds. Data at subsonic speeds would yield information regarding ground effects of the propulsion system.

LIST OF REFERENCES

1. Eggers, Alfred J. Jr. and Ashley, Holt. "Waverider Configurations from the 1950's to the 1990's," Proceeding of the First International Hypersonic Waverider Symposium, Universiy of Maryland, College Park, MD, October 1990.

2. Bowcutt, Kevin G. and Anderson, John D. "Viscous Optimized Hypersonic Waveriders," AIAA Paper 87-0272, AIAA 24th Aerospace Sciences Meeting, Reno, NV, January 12-15, 1987.

3. Bauer, Steven X.S. "Analysis of Two Viscous Optimized Waveriders," Proceedings of the First International Hypersonic Waverider Symposium, University of Maryland, College Park, MD, October 1990.

4. Takashima, Naruhisa. *Navier-Stokes Computation of a Viscous-Optimized Waverider.* NASA Contractor Report 189658, June 1992.

5. Cockrell, Charles E. Jr. "Interpretation of Waverider Performance Data Using Computational Fluid Dynamics," AIAA Paper 93-2921, AIAA 24th Fluid Dynamics Conference, Orlando, FL, July 6-9, 1993.

6. Anderson, John D. *Modern Compressible Flow with Historical Perspective*, McGraw-Hill Company, New York, 1982, pp. 250-256.

7. Corda, Stephen and Anderson, John D. "Viscous Optimized Hypersonic Waveriders Designed from Axisymmetric Flow Fields," AIAA Paper 88-0369, AIAA 26th Aerospace Sciences Meeting, Reno, NV, January 11-14, 1988.

8. Kuchemann, D. *The Aerodynamic Design of Aircraft*, Pergamon Press, Oxford, 1978, pp. 1-22, pp. 448-510.

9. O'Neill, Mary Kae and Lewis, Mark J. "Optimized Scramjet Integration on a Waverider," *Journal of Aircraft*, vol. 29, no. 6, November-December 1992, pp. 1114-1121.

10. Corda, Stephen and Seifert, E. Scott. *User Information for Maryland Axisymmetric Waverider Program (MAXWARP)*, University of Maryland Department of Aerospace Engineering, January 1989.

11. Anderson, John D. *Hypersonic and High Temperature Gas Dynamics*, McGraw-Hill Company, New York, 1989, pp. 286-295.

12. Coro, Rick. Notes on Waverider Cooperative Program, Memo from General Dynamics-Fort Worth Division, Fort Worth, TX, 3 July 1991.

13. Jackson, Charlie M. Jr., Corlett, William A. and Monta, William J. *Description and Calibration of the Langley Unitary Plan Wind Tunnel*, NASA TP 1905, November 1981.

14. Steinbrenner, John P. and Chawner, John R. *The GRIDGEN Version 8 Multiple Block Grid Generation Software*. MDA Engineering Report 92-01, MDA Engineering, Arlington, Texas, May 1993.

15. Richardson, Pamela F.; et al. *Hypersonic CFD Applications for the National Aero-Space Plane*. SAE Paper Number 892310, September 1989.

16. McGrory, William D.; Huebner, Lawrence D.; Slack, David C. and Walters, Robert W. "Development and Application of GASP 2.0," AIAA Paper 92-5067, AIAA Fourth International Aerospace Planes Conference, December 1992.

17. McGrory, William D.; Slack, David C.; Applebaum, Michael P. and Walters, Robert W. *GASP Version 2.2 User's Manual*, Aerosoft, Inc., Blackburg, VA, 1993.

18. Anderson, Dale A.; Tannehill, John C. and Pletcher, Richard H. *Computational Fluid Mechanics and Heat Transfer*, Hemisphere Publishing Corporation, 1984.

19. Walters, Robert W.; Slack, David C.; Cinnella, Pasquale; Applebaum, Michael and Frost, Corey. *A User's Guide to GASP*, Virginia Polytechnic Institute and State University, Department of Aerospace and Ocean Engineering, Blacksburg, VA, November 1990.

20. Vanmol, Denis O. and Anderson, John D., Jr. *Heat Transfer Characteristics of Hypersonic Waveriders with an Emphasis on the Leading Edge Effects*. NASA Contractor Report 189586, March 1992.

21. Vanmol, Denis O.; Lewis, Mark and Anderson, John D., Jr. *MAXWARP 2.0: Maryland Axisymmetric Waverider Program 2.0*. Report No. UM-AERO-92-04, Department of Aerospace Engineering, University of Maryland, College Park, Maryland, 1992.

22. Takishima, Naruhisa and Lewis, Mark J. "Waverider Configurations Based on Non-Axisymmetric Flow Fields for Engine-Airframe Integration," AIAA Paper 94-0380, AIAA 32nd Aerospace Sciences Meeting, Reno, NV, January 10-13, 1994.